APPLICATION OF CFD TO HYDROCYCLONE FLOW PREDICTION

MDUDUZI FELIX DLAMINI

AUGUST 2001

APPLICATION OF CFD TO HYDROCYCLONE FLOW PREDICTION

Mduduzi Felix Dlamini
BSc(Eng)

A dissertartion submitted to the Faculty of Engineering and the Built Environment at the University of Cape Town in partial fulfillment of the requirements for the degree of Master of Science in Engineering

Department of Mechanical Engineering
University of Cape Town
August 2004

Declaration

I declare that this dissertation contains only my own work, except where reference is made with acknowledgement to contributions from others. The material contained herein has also not been submitted for any purpose or examination to any other Department or University.

Signed:

(Mduduzi Felix Dlamini)

Dedication

I wish to extend a special thank-you to my parents, Jan and Joyce, for their emotional and financial support as well as the sacrifices they have made to afford me the opportunity to get such a good education. I can only hope that I have lived up to their expectations, given the huge investment they have made in me. To them, I will remain forever grateful, for facilitating the realisation of my dreams. Of my sisters Gabsile and Nosmilo, I am most appreciative, for their prayers of support and love for me. This one I dedicate to all of you, for believing in me.

Acknowledgements

I wish to thank all who contributed in one way or another to ensure the success of this research project. Needless to say, thanks is due to many, to whom I am grateful, but I am most indebted to:

Dr Malcolm Powell and Dr Chris Meyer for supervision of the research project and the constructive criticism of my ideas and dissertartion text, without which a better project and the appropriate documentation thereof, could not have resulted. Special thanks to Malcolm for the tremendous support provided, for believing and investing in me so much and for the countless crazy ideas he constantly generated to stimulate good research. Following the outcome of my research, I hope he finally has some faith in "*C*olourful *F*oolish *D*ynamics."

Dr Mike Slack (Fluent, UK) and Dr Matthew Brennan (University of Queensland, Australia) for sharing their ideas on cyclone modelling in CFD.

Dr Raj Rajamani (Utah University, USA) for providing me with the most needed experimental data used to set up the CFD models in this work.

Aubrey Mainza for - his provision of relevant literature, sharing his knowledge on hydrocyclones, proof-reading my dissertation text, in part, and the tremendous support provided.

Dr Richard Williams (Leeds University, UK), Dr Elizabeth Marshall (Fluent, USA) and Dr David Leith (University of North Carolina, USA) for their provision, in part, of relevant literature.

Dr Dave Deglon and Craig Sweet for the lecture on residence time distribution.

Dr Robert Sarracino, Andrew McBride and Indresan Govender for the intelligent discussions, their encouragement and support rendered in many ways.

Nicholas Gibson for the technical support provided.

My family and friends for their continued support.

God, for the wisdom, courage and strength.

Abstract

Classification is imperative to numerous industrial processes, more so where it impacts directly on the final product yield. As such, classification devices such as the hydrocyclone that contribute directly to the revenue generated in such industries, receive much deserved attention, which is aimed at improving their operation efficiencies. The mechanical simplicity of the hydrocyclone deceptively suggests non-intricate and well understood device hydrodynamics. On the contrary, improved understanding on the hydrodynamic behaviour and operation of the hydrocyclone are still being sought in order that its full classification potential may be realised. Current models describing such behaviour are predominantly highly empirical hence the need for continued complementary research via computational techniques such as Computational Fluid Dynamics (CFD).

This dissertation presents the outcome of an investigation into the flow characteristics of a hydrocyclone. Assessment of its hydrodynamic behaviour was conducted via interpretation of numerically predicted velocity and pressure field profiles arising from single phase (water-only) and multiphase (water/air) flow fields. The investigation, focussing primarily on single phase flow, was undertaken via numerical modelling of the hydrocyclone flow field, in a Cartesian coordinate system, using the commercial CFD code, Fluent v6.1.22. On account of the lack of published experimental data for water-only operated cyclones, no validation of the numerical models was undertaken. However, numerical predictions were obtained which reflect physically realistic hydrocyclone velocity and pressure field profiles. Despite the unsuccessful simulation of an air core, insight into the probable mechanism for its inception and development was gained from the multiphase flow predictions. The classical understanding of the hydrocyclone radial particle classification mechanism was also challenged. Furthermore, a generic methodology for meshing the main body of the hydrocyclone, particularly such as to avoid non-conformal meshing at the inlet-main chamber interface, was identified. The Reynolds Stress Model (RSM) and the Algebraic Slip Mixture Model (ASMM) were identified to be suitable for the numerical modelling of turbulence and multiphase hydrocyclone flow fields, respectively.

Liquid velocity component predictions were obtained that are consistent with experimentally determined trends. Evidence of the existence of a locus or envelope of zero axial velocity, within which fluid motion is directed upwards, and downwards beyond its periphery, was given by the establishment of a positive core and a surrounding negative axial flow field. This observation served to confirm the establishment of the vertically opposed overflow and underflow discharge streams, which determine the flow split of the classified product material, to the respective discharge orifices. An increase in the absolute values of the axial velocity was predicted with increase in distance from the envelope of zero axial velocity. The velocity increase was greater in the upward than the downward direction of flow. The horizontal axis intercept of the locus of zero axial velocity was predicted to migrate radially inwards, traversing down the length of the hydrocyclone.

Of the three liquid velocity components, the radial component, represented the least in magnitude. In accordance with the particle equilibrium orbit theory, a radial particle centrifugal-drag force balance is established which effects radial particle classification via inward radial transport of fine particles and centrifugal drift of large particles. This classical understanding of radial particle classification assumes that the radial velocity component is always directed radially inwards. However, the CFD predictions revealed joint precessing and oscillatory radial motion of the bulk flow field that resulted in combined inward and outward-directed radial velocity fields. As such, provided fluid and solid particle motion is approximately homogeneous in a radially outward-directed fluid velocity field, the solid particle centrifugal force is supplemented and the centrifugal drift thereof further enhanced. As a result, and on account of the relatively minute numerical values exhibited by the radial velocity field, the indication is that radial particle displacement and classification are predominantly due to the action of the centrifugal force and that radial particle migration is a mass displacement effect.

The tangential velocity component characteristic Rankine vortex structure was accurately predicted via the RSM. The fluid tangential velocity increased, traversing radially inwards from the hydrocyclone internal wall structure, before decreasing rapidly in the vicinity of its vertical geometric axis. Relatively less severe tangential velocity gradients were observed within the main chamber than in the conical chamber. In accordance with literature reports, a sub-atmospheric pressure and a positive pressure gradient were established at the hydrocyclone core and radially outwards, respectively. The sub-atmospheric core pressure was induced by the Rankine vortex, which effects solid body rotation at the core of the flow field via forced vortex motion. It was established via the multiphase flow simulations that a sub-atmospheric core pressure induces air core inception at the spigot discharge orifice and supports the central location thereof. The subsequent development of a centrally-positioned air column was identified as a dual function of pressure-driven gaseous diffusion and convective transport. It is recommended that the CFD hydrocyclone models resulting from this work be used to develop an air core extending across the entire length of the hydrocyclone in order to facilitate further investigation of the hydrodynamics of multiphase flow fields.

Contents

Declaration i

Dedication ii

Acknowledgements iii

Abstract iv

Nomenclature xi

1 Introduction 1
- 1.1 Historical background to the investigation 1
- 1.2 Terms of reference 2
- 1.3 Hypothesis 2
- 1.4 Objectives 3
  - 1.4.1 Detailed objectives 3
  - 1.4.2 Long term objectives 3
- 1.5 Proposed CFD methodology of solution 4
  - 1.5.1 Anticipated computational modelling problem areas 4
- 1.6 Plan of development 5

2 Literature Review 7
- 2.1 Hydrocyclone fundamentals 8
  - 2.1.1 Preliminary overview 8
  - 2.1.2 Hydrocyclone flow characteristics 13
  - 2.1.3 Pressure drop across the hydrocyclone 24
  - 2.1.4 Current experimental research techniques 24
  - 2.1.5 Summary 28
- 2.2 CFD hydrocyclone modelling 29
  - 2.2.1 Preliminary overview 29
  - 2.2.2 Current CFD hydrocyclone modelling research 30
  - 2.2.3 Summary 36

3 CFD Methodology of Solution 38
- 3.1 Iterative development of solution strategies 39
  - 3.1.1 Geometry generation and meshing 39

3.1.2 Boundary condition specification 44
3.1.3 Turbulence modelling 45
3.1.4 Multiphase modelling 46
3.1.5 Constitutive equation discretisation 46
3.1.6 Iterative development of single phase flow solution strategy . . 46
3.1.7 Iterative development of multiphase flow solution strategy . . . 50
3.2 Implemented solution strategies 54
3.2.1 Implemented single phase flow solution strategy 55
3.2.2 Implemented multiphase flow solution strategy 58
3.2.3 Summary 58

4 CFD Results and Discussion 60
4.1 Predicted single phase flow fields 61
4.1.1 Predicted hydrocyclone flow field development dynamics 61
4.1.2 Predicted single phase flow component velocity profiles 64
4.1.3 Comparison of single phase flow fields due to variable cyclone geometric configurations 73
4.1.4 Assessment of the appropriateness in application of the wall function approach 75
4.2 Predicted multiphase flow fields 77
4.2.1 Multiphase flow field velocity profile predictions 78
4.2.2 Multiphase flow field pressure profile predictions 79
4.2.3 The predicted air core inception and development mechanism . 80
4.2.4 Summary 83

5 Summary and Conclusions 84

6 Recommendations for Future Work 90

A The Experimental Hydrocyclone 99

B Computational Fluid Dynamics Fundamentals 101
B.1 The mathematical basis of computational fluid dynamics 102
B.1.1 Turbulence and CFD modelling thereof 105
B.1.2 Auxiliary models 117
B.2 The methodology of solution of CFD codes 120

C Comparative CFD Hydrocyclone Velocity Profile Predictions 124

List of Figures

2.1 Conventional cyclone cross-section 9
2.2 Cyclone feed inlet designs [1] 10
2.3 Cyclone flow schematic [2] 11
2.4 Hydrocyclone upper region flow structure [3] 15
2.5 Hydrocyclone particle equilibrium orbit [4] 16
2.6 Distribution of hydrocyclone axial velocity component [3] 19
2.7 Distribution of hydrocyclone radial velocity component [3] 20
2.8 Distribution of hydrocyclone tangential velocity component [3] 21
2.9 Hydrocyclone Rankine vortex structure [5] 22
2.10 Hydrocyclone variable particle size spatial distribution [3] 23
2.11 Hydrocyclone - laser-Doppler anemometry system [6] 27
2.12 Angular definition with respect to LDA system [6] 27
2.13 Non-conformal inlet-duct main chamber mesh [7] 32

3.1 Basic CFD cyclone model geometry 40
3.2 Cyclone meshing concept A 42
3.3 Spigot discharge orifice with irregularly structured circular core 43
3.4 Concept B geometry planar view 43
3.5 Spigot discharge orifice with regularly structured square core 44
3.6 Convergence history of single phase flow simulation 47
3.7 Predicted vertical planar start-up condition pressure profile 48
3.8 Comparison of steady state and transient vertical planar velocity profile predictions 49
3.9 Comparison of steady state and transient vertical planar pressure profile predictions 50
3.10 Normalised spigot discharge orifice air volume fraction profiles 52
3.11 Artificial vortex finder air core inception and inlet feed air trajectory . 53
3.12 Enhanced artificial air core development 54
3.13 Spigot air core inception and development 55
3.14 Rectangular cross-sectional inlet cyclone mesh 56
3.15 Diminished spigot discharge orifice air recirculation zones 58

4.1 Horizontal planar start-up and steady state velocity profiles 62
4.2 Vertical planar start-up and steady state velocity profiles 63
4.3 Overflow and underflow discharge stream particle pathlines 64

4.4 Vertical planar start-up and steady state pressure profiles 65
4.5 Horizontal planar axial velocity profiles (30-240 mm) 67
4.6 Horizontal planar radial velocity profiles (30-240 mm) 69
4.7 Horizontal planar tangential velocity profiles (30-240 mm) 71
4.8 Qualitative vertical planar fluid component velocity profiles 72
4.9 CFD hydrocyclone model coordinate system descriptor 74
4.10 Variation of turbulent kinetic energy per unit mass in hydrocyclone feed entry section 74
4.11 Comparison of experimental and CFD tangential velocity predictions . 76
4.12 Vertical planar mixture and air velocity profile comparison 78
4.13 Vertical planar water and mixture pressure profile comparison 80
4.14 Probable convective transport-pressure field air core development mechanism 82
4.15 Probable convective transport air core development mechanism 82

A.1 Experimental hydrocyclone [6] 100

C.1 Circular and rectangular inlet hydrocyclone axial velocity profile comparison 125
C.2 Circular and rectangular inlet hydrocyclone radial velocity profile comparison 126
C.3 Circular and rectangular inlet hydrocyclone tangential velocity profile comparison 127

List of Tables

3.1 CFD hydrocyclone model boundary conditions 45
3.2 Implemented governing transport equation discretisation schemes . . . 46
3.3 Wall function validation criteria of circular and rectangular cross-sectional inlet cyclones 57

A.1 Experimental cyclone dimensions 100

B.1 Turbulence model classification 111
B.2 Relative performance assessment of turbulence models 114

Nomenclature

Technical terminology

anisotropic directional

beat differential frequency between two simultaneously detected acoustic/light waves

cavitation liquid rupture process due to pressure decrease at constant temperature

closed system system with equivalent number of unknown variables and equations

comminution rock breakage

convection free/forced fluid motion displacement

creeping flow flow restricted to Re values less than 1

cut point (d_{50}) size fraction with equal probability of discharge with overflow and underflow streams

cut size characteristic separation size

cylindroconical cylindrical-conical geometry

eddy flow current opposed to direction of bulk flow

forced vortex vortex structure exhibiting solid body rotation

free vortex naturally/free-flowing vortex

hydraulic smoothness elimination of surface roughness effects via boundary layer due to incident fluid stream

hydrocyclone water-based particle classifier

hydrodynamic classification fluid media-based particle separation

isotropic non-directional

laminar streamlined particle motion

overflow primary hydrocyclone product stream

post-processing fluid flow problem solution and data extraction phase

pre-processing fluid flow problem definition phase

Rankine vortex compound vortex structure comprising free and forced vortices

rheology the study of flow and deformation of fluids and slurries

turbulence cross-flow particle motion

underflow secondary hydrocyclone product stream

Acronyms

ASMM Algebraic Slip Mixture Model

CFD Computational Fluid Dynamics

DDT Differential Doppler Technique

EIT Electrical Impedance Tomography

Fluent commercial CFD code post-processor

Gambit commercial CFD code pre-processor

GUI Graphical User Interface

LDA Laser-Doppler Anemometry

LES Large Eddy Simulation

MPRU Mineral Processing Research Unit

MRT Mean Residence Time

PRESTO Pressure-Staggered Option

QUICK Quadratic Upstream Interpolation for Convective Kinetics

RANS Reynolds Averaged Navier-Stokes

RNG Renormalisation group

RSM Reynolds Stress Model

RTD Residence Time Distribution

SIMPLE Semi-Implicit Method for Pressure-Linked Equations

SIMPLEC SIMPLE-Consistent

UDF User-Defined Function

UG2 Upper Ground - Level 2 (platinum-bearing ore body)

General symbols

$C_{1,2}$ empirical k-ϵ turbulence model constants

C_μ empirical k-ϵ turbulence model constant (0.09)

C_γ empirical algebraic stress model constant

D main chamber diameter [m]

E empirical standard wall functions' constant (9.793)

$\mathbf{F}$ force vector [N]

F_i summation of body force components [N]

G_k turbulence generation term

L characteristic mean flow length scale [m]

R radial distance from vertical central axis of cyclone [m]

Re Reynolds number

R_f water-to-underflow parameter

S shear rate [s^{-1}]

T transpose operator/time period [s]

T' relative turbulence intensity

U_P mean fluid velocity at nodal point P [ms^{-1}]

U^* dimensionless mean fluid velocity

$\mathbf{V}$ velocity vector [ms^{-1}]

V volume [m^3]

$\overset{\bullet}{V}$ volume flow rate [m^3s^{-1}]

$\mathbf{a}$ acceleration vetor [ms^{-2}]

d nominal particle diameter [m]

d_{50} diameter of particles with equal propability of discharge with overflow or underflow stream [m]

f_b beat frequency [Hz]

f_d drag force function

$\mathbf{g}$ gravitational acceleration vector [ms^{-2}]

k turbulent kinetic energy per unit mass [Jkg^{-1}]

$\dot{m}$ mass flow rate/mass transfer due to cavitation or user-defined sources [kgm^{-3}]

p hydrostatic pressure [Pa]

$\bar{t}$ mean residence time [s]

$\mathbf{u}$ velocity vector [ms^{-1}]

u, v velocity [ms^{-1}]

$\overline{u}$ mean velocity [ms^{-1}]

u' fluctuating velocity [ms^{-1}]

u_{rms} root mean square velocity [ms^{-1}]

u_{dr} drift velocity [ms^{-1}]

$\overline{u_i' u_j'}$ turbulent inertia tensor

y^+ dimensionless wall unit

y^* dimensionless wall unit unique to Fluent [8]

y_P perpendicular distance of near-wall node P from the wall [m]

∇ gradient operator

Greek symbols

α arbitrary proportionality constant/angular displacement [rad]/phasic volume fraction

β arbitrary viscosity exponent

δ_{ij} Kronecker delta

ϵ rate of dissipation of turbulent kinetic energy [m^{3}s^{-3}]

ϵ_{ij} strain rate tensor

κ von Kármán constant (0.42)

λ wavelength [m]/viscosity coefficient

μ molecular viscosity [Pa·s]

μ_t turbulent/Eddy viscosity [Pa·s]

ν kinematic viscosity [m^{2}s^{-1}]

ρ density [kgm^{-3}]

$\sigma_{\epsilon,k}$ empirical k-ϵ turbulence model constants

τ_{ij} stress tensor

τ_w wall shear stress [Pa]

Φ turbulent dissipation function

Subscripts

P first nodal point from the wall

a axial

b beat

c cyclone/centrifugal

d drag

e effective

dr drift

i, j, k summation/Cartesian coordinate indices

k phase identifier

l liquid

m mixture

n total number of constituent phases of a system

p particle/phase identifier

q phase identifier

r radial

s slurry/solid

t tangential

w wall

∞ far field

Superscripts

n fluid tangential velocity component radius exponent (-1 < n < 1)

Chapter 1

Introduction

This dissertation relates the outcome of an investigative assessment of the hydrodynamic behaviour of the *hydrocyclone*. The adopted computational investigative procedure was implemented through the application of *computational fluid dynamics* (CFD) using the commercial code Fluent version 6.1.22.

1.1 Historical background to the investigation

The immense impact of mining-related activities on modern day society dictates a constant review of current mining processes [9] [10]. Among the concerns are ecological, environmental [9] and energy consumption issues [10] [11] [12]. In recognition of this, concepts such as *ecological economics*, *environmental philosophy*, *sustainable development* [10] and *life-cycle assessment* [13] [14] have evolved [12]. These global scale concerns have led to strategies and initiatives being sought to facilitate industrial growth without adverse effects, particularly on the environment. A meeting by world leaders at the Earth Summit in Rio de Janeiro (Brazil) in 1992 attempted to address these concerns [11] [12]. Subsequent to this, The World Summit on Sustainable Development held in Johannesburg (South Africa) in 2002 was targeted at evaluating the decade-long implemented initiatives as well as devising new and sustainable direction for the future [12]. Although sustainable development by definition remains elusive and may adopt different meanings for different industries [12], for the mining and mineral industry it encompasses "the advancement of human prosperity in a way that does not compromise the potential prosperity and quality of life for future generations" [11]. In light of remaining true to this philosophy, tremendous effort is being channeled towards sustainable development, within a sustainable mining framework [11], in order to ensure that the mining industry remains viable and operational in a global sense, so as to provide continued economic sustenance, more so in developing countries.

Mining operations currently employ explosive blasting as well as crushing and milling circuits for *comminution*. The subsequent downstream processes used for mineral extraction include *classification* and *flotation*. The commercial use of the hydrocyclone, for classification in mineral processing applications, dates back to 1937 [1]. In present day, the hydrocyclone, used primarily in closed circuit grinding, finds widespread acceptance as the standard industrial classifier [3] [15] due to its mechanical simplicity [1], compactness [7] and relatively low capital and maintenance costs [3] [16]. Despite the existent historic preference of the hydrocyclone for classification applications, there still exists room to enhance its classification efficiency for improved mineral extraction [1].

Although mechanically simple, the hydrocyclone presents a complex internal flow structure [1] [7] [17] that is subject to a substantial amount of ongoing research [3]. In view of the large thrust in modern mining toward the use of numerical methods for the optimisation of current and the design of new mineral processing processes, a step change from the current semi-empirical models is inevitable. This is where CFD modelling comes into its own and as such led to the proposal of a research project of this nature. However, inasmuch as CFD offers an alternative to the experiment-based approach and enables parametric studies to be conducted in considerably reduced time scales, it still suffers the drawback of being unable to be professed adequately, without continued reference to experimental validation [18] [19].

1.2 Terms of reference

This research project was initiated by Dr. Malcolm Powell of the *Mineral Processing Research Unit* (MPRU) of the University of Cape Town's Chemical Engineering Department. The long term goal of this research is to develop an experimentally validated CFD model of the three-product cyclone, aimed at providing an assessment of the cyclone's hydrodynamic performance. In line with this objective, the MPRU is currently conducting experimental investigations on the operation of the three-product cyclone, for application in the platinum industry [20].

1.3 Hypothesis

Mechanistically appropriate modelling of the hydrocyclone flow and pressure fields can provide an improved understanding of the particle classification mechanism that is effected within the device.

1.4 Objectives

The principal objective of this research project was to provide an understanding of the hydrodynamics of a hydrocyclone by modelling the behaviour of the fluid flow field. This was to be achieved by setting up single phase (water-only) and multiphase (water/air) two-product CFD hydrocyclone models. The CFD model predictions were to be validated against experimental data and related to the classification mechanism in a hydrocyclone. The milestone of this research is to extend the application of CFD hydrocyclone modelling to the three-product cyclone, at practical slurry concentrations. The long term objectives, which fall outside the scope of the current project, are presented in order to put the short term objectives into perspective.

1.4.1 Detailed objectives

It was proposed to set up a two-product CFD hydrocyclone model to identify/establish:

1. Suitable hydrocyclone geometry meshing procedures.
2. The turbulence and multiphase models suited to single and multiphase modelling of hydrocyclone flow.
3. The governing transport equation discretisation schemes that yield numeric flow field predictions exhibiting physically realistic flow behaviour.
4. Computationally economic solution strategies for modelling both single and multiphase hydrocyclone flows.
5. The procedural methodology for development and optimisation of the air core.
6. An understanding of the hydrodynamic behaviour of the hydrocyclone and its classification mechanism through interpretation of the predicted velocity and pressure field profiles.
7. An understanding of the mechanism for inception and development of the air core.
8. The effects of variable inlet geometries on the hydrocyclone flow field.

1.4.2 Long term objectives

The long term objectives of this research involve expanding on the outcomes of the current research, by using the resulting CFD hydrocyclone models to:

1. Develop an air core and to investigate its dynamics and influence on the hydrocyclone flow field.

2. Provide an understanding of the effects of variable viscosity on the flow, for a fixed set of boundary conditions.

3. Employ the Lagrangian particle model to obtain three-dimensional particle tracking predictions within the hydrocyclone flow field, through the introduction of a limited number of various-sized solid particles, in order to gain insight into the hydrocyclone classification mechanism.

4. Investigate high wear regions and to undertake parametric geometry optimisation, in order to identify means by which turbulence and component wear may be minimised.

1.5 Proposed CFD methodology of solution

In view of the research objectives, it was proposed to:

1. Employ both low and high order turbulence models and to examine their relative abilities in predicting hydrocyclone flow dynamics. The turbulence models to be investigated include the:

   - Standard k-ϵ model
   - Reynolds stress model (RSM)
   - Large eddy simulation model (LES)

2. Investigate the effects of circular and rectangular inlet geometries on the hydrocyclone flow field.

1.5.1 Anticipated computational modelling problem areas

Among the identified potential problems concerned with setting up a fully functional CFD hydrocylone model are:

1. Effective meshing of complex hydrocyclone geometries e.g. the complexity of hydrocyclone inlet geometries may dictate use of an unstructured grid that merges with a structured grid in the main chamber of the hydrocyclone, resulting in undesirable numeric diffusion [21] due to non-conformal meshing at the structured-unstructured grid interface [7].

2. A correct choice of a discretisation scheme providing suitable pressure-velocity coupling [18] while exhibiting minimal numeric diffusion [21], at economic simulation run times.
3. A correct choice of the turbulence model for purposes of modelling the intricate anisotropic turbulent features of the hydrocylone flow [7] [17] comprising a compound vortex, as well as short circuit and Eddy flows [3].
4. The difficulty associated with providing a realistic prediction of both the air core and flow split [7] [19].
5. The inability to accurately model solid-solid and solid-fluid particle interactions [19].
6. The handicap of current numerical algorithms capable of handling only fluid dynamics problems at low solids concentrations [19].

1.6 Plan of development

Chapter 2 is aimed at furnishing the reader with background theory relating to hydrocyclones. In accordance with the research objectives, the discussion focusses primarily on the flow patterns exhibited by the internal flow field of a hydrocyclone. Careful consideration is also given to the influence that the associated internal flow structure has on the solid particle classification effected within the device. The intricacy of the classification and other mechanisms, which are responsible for effecting functional operation of the hydrocyclone, are noted. The lack of a complete understanding of the general hydrodynamic behaviour of the hydrocyclone is also emphasised. The inadequancy of current empirical models in describing and quantifying the dynamics of the hydrocyclone, which further motivates the need for the adoption of computational techniques in order to supplement experimental research on the subject, is also motivated. In conclusion, a review on the current state of CFD hydrocyclone modelling is given.

Chapter 3 discusses the iterative development of the strategies employed in simulating both single phase (water-only) and multiphase (water/air) hydrocyclone flows via the CFD hydrocyclone models. Specific details are given on the means used to avert the problems commonly encountered with the meshing of complex cyclone geometries. The turbulence and multiphase models used for the numerical modelling of hydrocyclone flows are, together with the limitations imposed on them, discussed.

Chapter 4 discusses the numerical flow field predictions arising from the CFD hydrocyclone models, with regard to the velocity and pressure field profiles. The consistency of the numerical predictions with experimentally observed and inferred phenomena is examined and discussed. The insights drawn from the CFD predictions, some of which challenge common conceptions on specific phenomena, are interpreted such as to give credible accounts of the dynamics of the actual physical processes

A statement of the extent to which the objectives of the research project have been met is given in chapter 5. Finally, recommendations regarding future research on the subject, are made in chapter 6.

Chapter 2

Literature Review

This chapter presents a review of the fundamentals relating to *hydrocyclones* and *computational fluid dynamics* (CFD), within the context of this dissertation. Section 2.1 introduces conventional hydrocyclone nomenclature and highlights the geometric features of the device, with particular reference to feed inlet designs. The internal flow structure of the hydrocyclone constitutes the main focus of the discussion. As such, an in-depth discussion of the flow patterns exhibited by both fluid and solid particles is presented. The significant complementary flow features that include the *particle force balance* and the *air core* are also discussed, in the context of particle *classification* and flow *stability*, respectively. The intricacy of the internal flow field of the hydrocyclone is highlighted through a discussion of the *short-circuit* and *Eddy flows*, the three liquid velocity components and the associated *compound vortex* structure. The significance of the pressure drop effected across the hydrocyclone is also highlighted. In conclusion, current experiment-based research techniques that offer potential for use and which have been used to validate hydrocyclone CFD models, are discussed.

Section 2.2 discusses the current state of CFD hydrocyclone modelling. Particular reference is made to CFD studies that have led to the realisation of physically realistic hydrocyclone flow field predictions. The review on these publications aims to motivate the level of difficulty of this task and to provide an understanding of the rationale used in devising the CFD modelling strategies adopted in this work. In this regard, the difficulties involved with and the means used to address the meshing of complex hydrocyclone geometries are discussed. The turbulence and multiphase models as well as the numeric discretisation schemes suited to modelling hydrocyclone flow are also identified.

2.1 Hydrocyclone fundamentals

The *cyclone* is a separation device that induces swirl motion in a *fluid* or *slurry*, thus imposing an enhanced *radial acceleration* on a *dispersed secondary particulate* or *liquid suspension* for the purpose of *separation* or *classification* from a *continuous primary fluid phase* [5]. When water is used as the primary fluid phase, it is termed a *hydrocyclone*. In this and subsequent sections, the word cyclone will be used in place of hydrocyclone, following common practice. Explicit use of the word hydrocyclone will solely imply the use of water for the primary fluid phase.

The mechanical simplicity of the hydrocyclone deceptively suggests non-intricate and well understood device hydrodynamics. On the contrary, improved understanding on the operation of the hydrocyclone is still being sought in order that its full classification potential may be realised [17] [22]. Consequently, this section is intended to motivate the need for continued research on hydrocyclone flow dynamics as well as to furnish fundamental concepts relating particularly to hydrocyclones.

2.1.1 Preliminary overview

a) Historical outline

It is speculated [1] that hydrocyclones may have been used for various classification applications before 1890. In 1891, Bretney was granted a patent on a device for separating sand and water [23] that bears some resemblance to present-day water desanding cyclones [1]. The classification process reached new frontiers in 1937, which marked the first commercial application of the hydrocyclone in the treatment of cellulose fiber in the pulp and paper industry [1]. Following this, the cyclone was soon adopted for coal washing and concentration and found increasing use in the mineral processing industry by the mid 1950s [1]. Significant research into its principles of operation ran in parallel with this development.

Subjected to continued research [3], the hydrocyclone has undergone extensive design refinement since the production of the first prototype [15]. As such, component erosion, for example, can now be alleviated through the use of replaceable rubber liners or components [3]. Despite its legacy in classification applications, the hydrocyclone still presents difficulties in its operation. Despite its short-comings, some of which are highlighted in section 2.1.1 (e), the hydrocyclone nonetheless remains widely used to present-day.

b) Cyclone geometry

The conventional *outer wall tangential* cyclone, depicted in figure 2.1, is geometrically *cylindroconical*. Its main features comprise an inlet duct tangentially linked to the main cylindrical chamber that is connected to a conical section. An axially positioned discharge duct termed the *vortex finder* projects downwards into the main cylindrical chamber, and the *spigot* is situated at the cone apex.

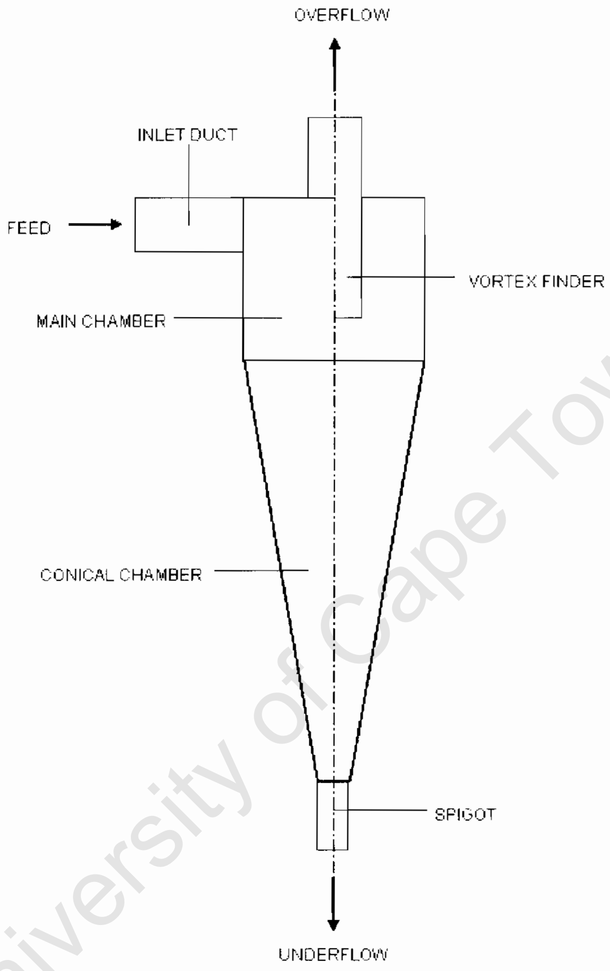

Figure 2.1: Conventional cyclone cross-section

There are a number variations of the conventional cyclone. One such cyclone is the *three-product cyclone* that has an additional vortex finder, called the *inner vortex finder*, positioned concentrically relative to the conventional vortex finder and providing two overflow streams.

i) Cyclone feed inlet designs Figure 2.2 depicts three cyclone feed inlet designs that are currently in use and may be categorised as [1]:

1. Outer wall tangential - the outside of the feed nozzle is tangent to the inside diameter of the cyclone feed chamber.
2. Involute - both the outside and inside edges of the feed nozzle are tangent to the inside diameter of the feed chamber.
3. Centreline tangential - the centreline of the nozzle is tangent to the inside diameter of the cyclone feed chamber.

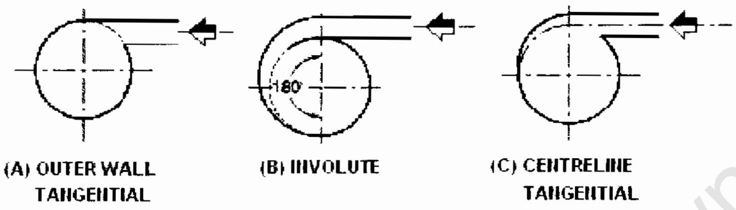

Figure 2.2: Cyclone feed inlet designs [1]

Cyclone feed inlets exhibit cross-sectional variations ranging from rectangular to square and circular geometries. The most common feed inlet designs are the outer wall tangential and involute types depicted in figures 2.2 (a) and (b) [1]. The feed inlet type has a profound effect on the internal flow structure of the cyclone and is a key design aspect for optimum performance thereof [1]. Inlet geometry effects include flow field turbulence, which may have adverse effects on classification, and component wear, hence they are worth investigating and are ideally suited to CFD analysis.

c) Hydrocyclone principle of operation

With reference to figure 2.3, the pressurised fluid is fed tangentially through the inlet duct into the cylindrical chamber, where a strong swirl motion is established [22]. The *centrifugal forces* arising from this motion cause the solid particles coarser than the *cut point size* [3] to migrate to and concentrate at the cyclone wall [16] [22]. These water-deficient particles are conveyed by the outer spiral and discharge as a thickened suspension [16] at the cone's apex, through the spigot. This stream, consisting the faster settling and coarser particles, is called the *underflow*. A second stream mainly comprising solid particles finer than the cut point size and of lower settling velocities, called the *overflow*, discharges with the inner spiral fluid, through the vortex finder located at the top of the cyclone [16]. In this manner, the coarse and fine *size* *fractions* are separated. Depending on the circuit configuration, the underflow may be recirculated for additional grinding while the overflow is processed in subsequent downstream processes. Radial particle classification, in the context of radial particle size distribution, is discussed in detail in section 2.1.2 (d).

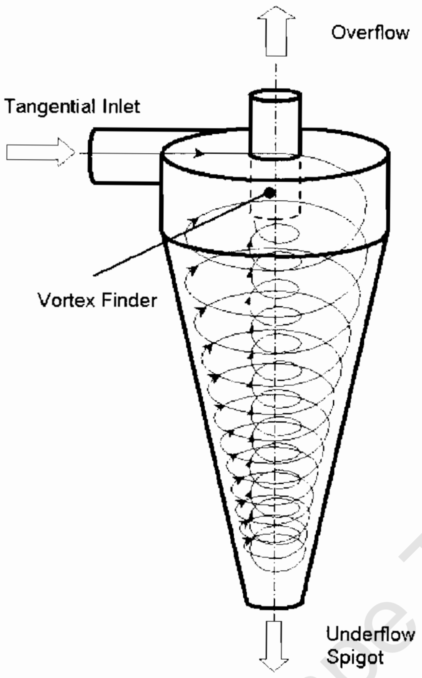

Figure 2.3: Cyclone flow schematic [2]

d) General hydrocyclone applications

Hydrocyclone applications are derived on the basis of their ability to separate particle suspensions in accordance with *particle size* and *density*, and *shape* [1]. The hydrocyclone exhibits extreme versatility in its applications as indicated by its capability for use as a *thickner*, a *classifier* or a *concentrator* and a *clarifier* [3]. In the context of mineral processing applications, hydrocyclones are generally used for desliming, dewatering, liquid clarification, liquid degasing, slurry thickening, solids washing and solids classification [1] [16] [17] [22]. The hydrocyclone lends itself to numerous applications, examples of which include:

- Food industry - protein level reduction via starch washing as well as starch effluent treatment [24]
- Chemicals industry - precipitate removal [24]

- Oil industry - oil-water and oil-solid particulates separation [25] [26]
- Mineral processing classification of products fine enough for downstream mineral extraction

e) Hydrocyclone pros and cons

The cyclone is preferentially adopted over competitive equipment for numerous classification applications. Some advantages and disadvantages of the cyclone include [3]:

Advantages

- robust, due to simple construction and lack of moving parts
- compact, ensuring space savings and simple structural supports
- relatively low capital and maintenance costs
- flexible mounting positions during operation, due to high internal separating forces generated
- short residence times permitting high control action speeds
- versatility in design, allowing ease of component replacement to address high wear issues

Disadvantages

- large energy expenditure, requiring large pumping unit to overcome pressure drop across device
- lack of sharpness of separation
- limit imposed on degree of separation, irrespective of range of separation sizes
- presence of unclassified contents in overflow stream due to short circuit flow
- high sensitivity to operating conditions e.g. feed behaviour instability hampers performance
- involves numerous classification efficiency determining input variables such as feed pressure, feed size distribution and fluid media viscosity, in addition to its partially understood intricate hydrodynamics, leading to inefficiency in its operation

- difficulties associated with on-line measurement and determination of fluid media viscosity and product stream particle size distributions complicate direct performance evaluation and control.

2.1.2 Hydrocyclone flow characteristics

The nature of the flow within a hydrocyclone can supposedly be classified as *laminar* or *turbulent* on the basis of the flow *Reynolds number*, Re, and is discussed as published by Kelly [3] and Svarovsky [27]. The definition of Re with regard to a hydrocyclone is two-fold in the sense that it may be formulated on the basis of a characteristic particle dimension, Re_p, or a combination of a characteristic device dimension and the mean flow velocity, Re_c. The multiple definitions for Re present a problem in the choice of an applicable definition for flow characterisation within a hydrocyclone, for a specific set of operating conditions. The definition normally adopted is:

$$Re_c = \frac{\rho \overline{u} D}{\mu} \tag{2.1}$$

where

Re_c – cyclone characteristic Reynolds number
ρ – fluid density
$\overline{u}$ – main chamber mean flow velocity
D – main chamber diameter
μ – fluid viscosity

and

Re_p – particle characteristic Reynolds number
d_{50} – diameter of particles with equal probabilty of discharge with overflow or underflow stream

On the basis of Re_c as defined in equation 2.1, values of Re_c in the range $10^4 - 10^6$ would imply turbulent flow within the feed inlet duct. A turbulent flow structure at the feed inlet duct does not however impose similar flow conditions within the main body of the hydrocyclone. Laminar flow conditions can in fact be maintained to higher Re in curved channels and on the basis of Re_p, d_{50} correlations tend to suggest laminar settling behaviour within the main body of the hydrocyclone. The subsequent discussion on *residence time distribution* (RTD) is due to Levenspiel [28].

a) Residence time distribution

Any distinct fluid or solid particles which traverse different paths upon entering the cyclone may require different time intervals before being discharged with either the overflow or underflow stream. The distribution of these times, which is only applicable to the discharge streams, is termed the *residence time distribution* (RTD). The *stimulus-response* technique, which involves the introduction of a tracer input into the flow system, for which a time record of the discharge response may be obtained, has been successfully employed to study and characterise bulk fluid flow behaviour. However, the *mean residence time* (MRT) $\bar{t}$, is often adopted for practical applications because it can be readily determined via equation 2.2, if the volume V_c of the cyclone and the volume flow rate $\overset{\bullet}{V}_s$ of the slurry are known.

$$\bar{t} = \frac{V_c}{\overset{\bullet}{V}_s} \tag{2.2}$$

where

$\bar{t}$ – mean residence time
V_c – cyclone volume
$\overset{\bullet}{V}_s$ – slurry volume flow rate

Cyclones generally have short mean residence times, on account of the high particle accelerations arising from the swirl motion of the flow [3]. A knowledge of the MRT is essential because it determines the frequency with which any flow measurements should be made in order to adequately capture any details for the purpose of flow characterisation. In a computational modelling sense, the MRT also gives an indication of the simulation time span that is necessary for the determination of meaningful flow predictions.

b) Hydrocyclone primary flow patterns

The most significant flow pattern in a hydrocyclone, depicted in figure 2.3, is the spiral within a spiral [3] [22]. The outer spiral is responsible for discharging the underflow through the spigot and the inner spiral for transporting the overflow through the vortex finder located in the roof of the cyclone [22]. The swirl motion of these two spirals is unidirectional, with the exception of the vertical velocity component which exhibits velocity reversal [3]. The spiral motion [3] of the fluid particles constitutes *free* and *forced vortices* [5] [29], which are discussed in detail in section 2.1.2 (e).

c) Hydrocyclone secondary flow patterns

Secondary flow patterns occuring within the cyclone and prevalent in the main cylindrical chamber include *short circuit* and *Eddy flow*, which are depicted in figure 2.4. The short circuit flow results from the obstruction of the tangential velocity of the bulk flow [3] and evolves in the region near the cyclone roof and the outer wall of the vortex finder, with the consequent substantial retardation of the bulk fluid motion [22]. Photographic evidence, visual inspection and *sampling* indicate that, for a slurry, the short circuit flow path indicated in figure 2.4 constitutes a concentrated band of coarse solid particles that are discharged with the overflow without classification [16]. The vortex finder, in addition to discharging the overflow, is intended to minimise the short circuit flow [3]. The Eddy flow, on the other hand, is the direct result of the overflow orifice failing to handle the upflowing vortex [3]. These issues present an ideal application of CFD, particularly in investigating geometry changes that may be effected such as to improve the classification efficiency of the cyclone.

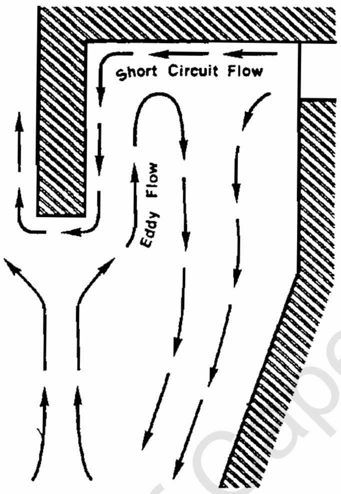

Figure 2.4: Hydrocyclone upper region flow structure [3]

d) Hydrocyclone flow complementary features

i) The hydrocyclone particle equilibrium orbit theory In addition to the hydrocyclone flow patterns already described, there occurs interesting particle-related phenomena in the hydrocyclone *radial* and *axial* directions that establish *equilibrium orbits* and *loci* respectively. According to the *particle equilibrium orbit theory*, the hydrocyclone particles reach an *equilibrium orbit* in the *radial* direction when the *centrifugal force* on them is balanced by the fluid *drag force* [4] [30]. An illustration of this particle force balance is given in figure 2.5.

The mechanism of radial particle classification within the hydrocyclone is commonly accounted for through the particle equilibrium orbit theory [4] [30] [31] [32]

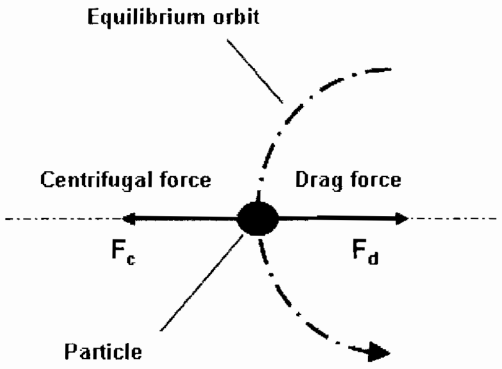

Figure 2.5: Hydrocyclone particle equilibrium orbit [4]

[33]. As such, in a radial sense, particle classification is understood to result primarily from a centrifugal-drag force balance [33], with radial drag of small particles towards the core, throughout the conical section, and centrifugal drift of large particles towards the cyclone wall [31]. In accordance with this understanding, Wills [32] reports that the faster settling coarser particles migrate to the cyclone wall, where the fluid velocity is lowest, and discharge with the underflow. Conversely, the slower settling finer particles migrate towards the low pressure zone located along the central axis of the cyclone, due to the action of the drag force and are discharged with the overflow [32]. Although Cullivan et. al [31] also report this common conception of radial particle classification, they, in turn, challenge it. However, their research which sought to shed new light on this phenomenon, on the basis of three-dimensional particle tracking using the *Lagrangian particle model*, without experimental validation, is inconclusive.

Axially, the motion of the fluid elements within the hydrocyclone occurs in two opposing directions [22]. This necessitates flow reversal and results in a condition of zero axial velocity for fluid elements intermediate between the cone apex and the region consisting of fluid elements migrating towards the vortex finder [22]. The significance of the *locus of zero axial velocity*, depicted in figure 2.6, and on which d_{50}-sized particles are assumed to lie [4] [33], is discussed in section 2.1.2 (e).

ii) The air core Hydrocyclones experience very high liquid velocities in the vicinity of the central vertical axis that cause a pressure reduction capable of yielding a gas-liquid interface in the region of the core [17]. If operating conditions are such that the discharge orifices of the hydrocyclone are exposed to the atmosphere, the core region is transformed into a central *air core* [17] [22]. For sufficiently low back pressures, liquid vaporisation may occur, resulting in the preferential formation of a vapor core

[17]. The alternative is the complete suppression of any core formations [22]. Following this discussion, the implication is that both air core inception and development are pressure-driven. However, a new understanding of the mechanism leading to air core development due to Cullivan et. al. [31] has evolved. Their CFD water-only simulations, for which experimental validation was acquired, demonstrated air core development to be transport-driven as opposed to being pressure-driven. These phenomena refer to air core development by mass diffusion, due to flow reversal, and through the introduction of an influx of air at the spigot orifice, on account of the generation of a sub-atmospheric core-pressure, respectively [31].

Air core geometries are operating condition dependant and may assume the form of linear or precessing sinusoidally-shaped cylinders [16] [17] extending in part or throughout the hydrocyclone length [16] [22]. The common understanding that the presence of an air core within a hydrocyclone is a desirable feature, because of implied vortex stability, is widely professed in the literature [3] [22]. The air core is also associated with the type of underflow discharge [34]. The spray-type discharge indicates the existence of an air core [34] and marks the condition where solids and liquid discharge in a violent spray in the shape of a hollow cone, with maximum removal of solids [3]. The lack of an air core is indicated by the rope-type discharge [34] in which the discharge is a rotating solid spiral. Kelsall [16] reported the diameter of a cylindrical air core, positioned coaxially with the cyclone and extending into the vortex finder, to be dependent on and constrained by both the diameter of the orifice at the apex of the conical chamber and the internal diameter of the vortex finder. In contrast, experimental evidence due to Williams et. al. [35] indicated the diameter of a cylindrical air core to be strongly dependent only on the diameter of the apex. A detrimental condition, prohibiting formation of the overflow stream, would arise if the diameter of the air core were to exceed that of the vortex finder [16].

e) The three velocity components in a hydrocyclone

Any three-dimensional velocity within a hydrocyclone flow field may be resolved into three mutually perpendicular components namely [3] [16]:

- axial/vertical component (u_a) - parallel to central cyclone axis
- radial component (u_r) - in horizontal plane along radius
- tangential/horizontal component (u_t) - in horizontal plane and perpendicular to central cyclone axis at all radii

Results of these velocity components are depicted at different scales in figures 2.6, 2.7 and 2.8 as produced by Kelsall [16], from an optical study of a dilute suspension of aluminium particles. Although these results do not reflect particle behaviour at practical slurry concentrations, they are regarded to give the most reliable indication of hydrocyclone flow patterns [3]. Consistent results were obtained by Hsieh [6] in a recent study employing *Laser Doppler Anemometry* (LDA). Details of this technique and the experiment are discussed in sections 2.1.4 (b) and (c), respectively. In their experimental studies, both Kelsall [16] and Hsieh [6] measured the fluid tangential and axial velocity components at different horizontal levels and calculated the radial velocity component from the continuity equation. The subsequent discussion on the three liquid velocity components in a hydrocyclone is largely due to Kelly [3].

i) Liquid axial velocity The liquid axial velocity component is an indication of the magnitude of the two spirals and therefore determines the volumetric distribution of the product between the overflow and underflow streams. The *locus* or *envelope* of *zero axial velocity*, which is a significant feature of this velocity component [4], is depicted in figure 2.6. This velocity envelope divides the outer downward flowing and the inner upward flowing fluid layers. In both cases, an increase in the axial velocity component is observed with increase in distance from the envelope. The velocity increase is greater in the upward than the downward direction of flow.

Hsieh [6] noted marked asymmetry of the axial velocity profiles about the cyclone central axis, in the region between the vortex finder and the hydrocyclone wall, on account of the geometric inlet asymmetry [6]. This asymmetry was less pronounced in the sub-vortex finder region but reappeared in the vicinity of the apex of the conical chamber, where the flow passage narrows, leading to increased turbulence that in turn causes fluctuation of the air core [6]. With reference to figure 2.12, Hsieh [6] reported the short-circuiting flow depicted in figure 2.4, to be most pronounced at 270^0 and to increase with increase in fluid viscosity and inlet volumetric flow rate. Axial flow reversal was also noted [6] to occur along most of the hydrocyclone length, with the exception of regions in close proximity to the apex of the conical chamber. This phenomenon reportedly [6] accounts for the minimal fluid content of the underflow stream.

ii) Liquid radial velocity Of the three liquid velocity components in a hydrocyclone, the radial component is the least in magnitude. As depicted in figure 2.7, it increases in magnitude, up to a maximum in the vicinity of the cyclone wall. The positive velocity profiles indicate a radially inward-directed flow field. As a result of

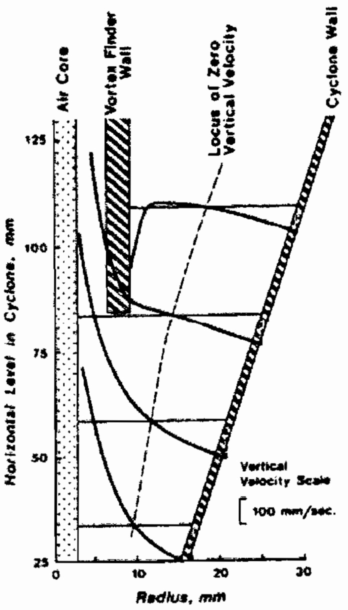

Figure 2.6: Distribution of hydrocyclone axial velocity component [3]

centrifugal force, particles need to settle against this component in order to enable their discharge as underflow. With the exception of Eddy flow in the region between the cyclone inlet and the exterior of the vortex finder, with reference to figure 2.4, this component is normally directed radially inwards.

iii) Liquid tangential velocity With respect to figure 2.8, the following trends, in the spatial distribution of the tangential velocity component, are observed [16]:

1. At horizontal levels above the bottom of the vortex finder, there occurs a velocity increase, traversing from the vicinity of the cyclone wall to the exterior of the vortex finder. In close proximity to the vortex finder, the velocity reaches a maximum before decreasing suddenly.
2. The sub-vortex finder region is marked with a similar but relatively steeper velocity increase that reaches a maximum in the vicinity of the air core, before decreasing rapidly.
3. The vertical inclination of the arbitrary *locus of constant tangential velocity* signifies that the resulting *velocity envelopes* consist cylinders coaxial with the hydrocyclone [3] [6].

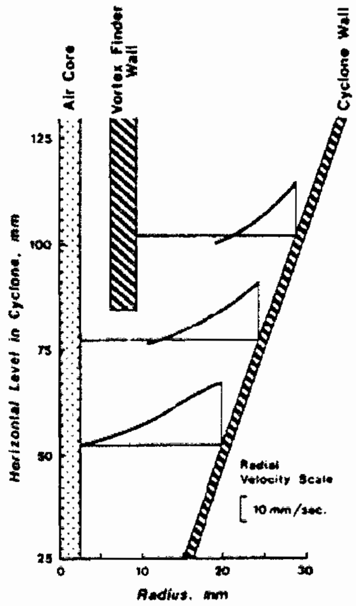

Figure 2.7: Distribution of hydrocyclone radial velocity component [3]

In contrast to the significant asymmetry exhibited by the axial velocity profiles about the central axis of the hydrocyclone, Hsieh [6] observed similar but less pronounced asymmetry of the tangential velocity profiles. This observation was particularly consistent in the regions around the vortex finder and the apex of the conical chamber.

The mathematical relationship between the radius r, measured radially from the axis of rotation, and the tangential velocity component at this radius, for all positions within the cyclone, ranging from the wall to the immediate vicinity of the central air core [16], assumes the form [1]:

$$u_t r^n = \text{constant} \tag{2.3}$$

Viscous shearing actions within real fluids are capable of causing fluid rotations that can develop into *compound vortices* [36] with inner cores approximating *forced vortices* and outer regions approximating *free vortices* [9]. Such a combined vortex flow structure is termed a *Rankine vortex* [19] [29]. Hydrocyclone flow similarly assumes a *free vortex* in the outer region as n tends to unity and the equation defining this swirl motion is given by the relation:

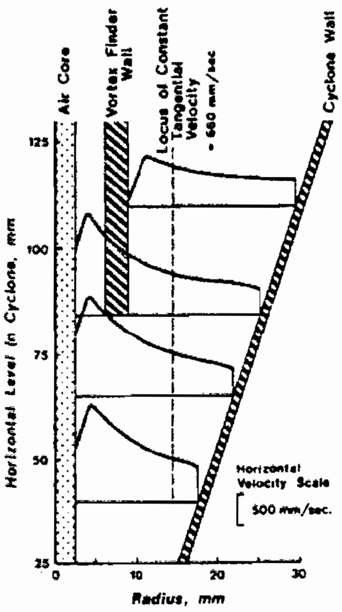

Figure 2.8: Distribution of hydrocyclone tangential velocity component [3]

$$u_t r = \text{constant} \tag{2.4}$$

According to equation 2.4, u_t theoretically becomes infinite at the centre of the vortex [3] [9] [36]. This behaviour is closely approximated by real flows which assume a vortex core instead, bearing a different relationship between the tangential velocity component and radius. There occurs a transition, traversing from this air core to the surrounding area, which is subjected to a *forced vortex* that revolves at *constant angular velocity*, exhibiting '*solid body rotation*' [36]. The mathematical definition of forced vortex motion is stated as:

$$u_t r^{-1} = \text{constant} \tag{2.5}$$

Figure 2.9 depicts a vertical cross-sectional view of the typical tangential velocity profile exhibited by particles contained within a hydrocyclone flow field. Also indicated, is the Rankine vortex structure, which constitutes free and forced vortices near the hydrocyclone wall and central vertical axis respectively. The corresponding regions, in which the free and forced vortex equations i.e. equations 2.4 and 2.5, are respectively valid, are indicated by the construction lines. The parabolic peak, intermediate between the two vortex regions, marks a gradual transition between the two distinct

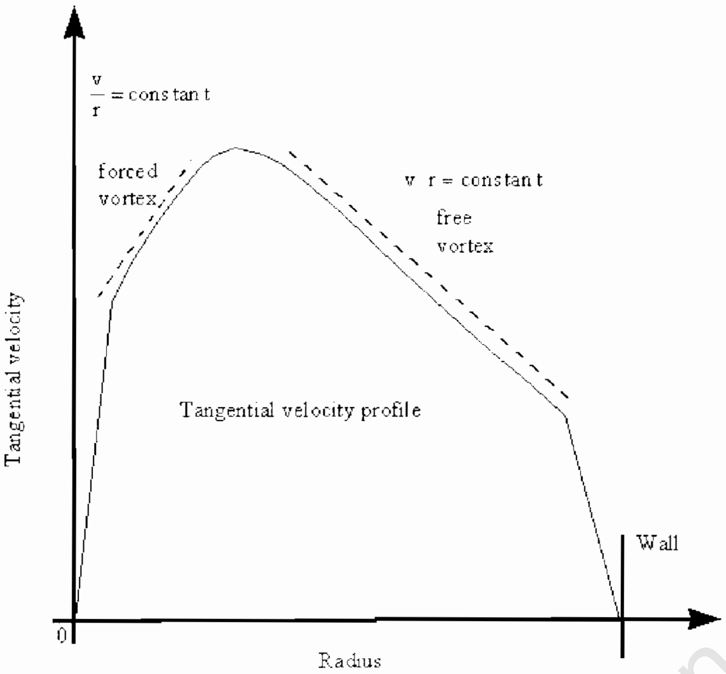

Figure 2.9: Hydrocyclone Rankine vortex structure [5]

and uniquely defined vortex structures. The hypothetical condition of infinite tangential velocity at the hydrocyclone axis, implied by equation 2.4, is closely approximated by the line extending from the origin.

f) Solid particle behaviour within a hydrocyclone

Unfortunately, very little information on the behaviour [3] [22] and measurement of the distribution [34] of solid particles within a hydrocyclone flow field is published. Investigation of the internal flow structure of a hydrocyclone, for practical applications, is normally impeded by the opacity of the slurry [37] and the walls of the device [34]. As such, the subsequent discussion merely describes probable solid particle behaviour due to studies conducted by Renner and Cohen [3] [32].

Figure 2.10 indicates the four regions labelled A-D into which the interior of the hydrocyclone can be subdivided based on particle size distribution. The information on particle size distribution can, on a regional basis, be summarised thus [3] [32]:

A – feed size distribution i.e. unclassified feed
B – essentially coarse product size distribution
C – essentially fine product size distribution
D – intermediate-sized particle distribution

The concentration of the intermediate-sized particles in region D is higher than in either the feed or the remainder of the hydrocyclone contents as a whole [3]. This region coincides, in part, with the region subjected to Eddy flow motion, as depicted in figure 2.4. As such, particles in this region accumulate only to be displaced due to lack of room [3]. This phenomenon is indicative of the region acting as a locus of active classification [32] and lack of its proper formation, stemming from a poor design and/or operating conditions, may lead to poor classification [3]. An assessment of fluid flow behaviour in this region, for variable cyclone geometries and operating conditions, such as to provide an improved understanding of the classification mechanism, falls within the realm of CFD.

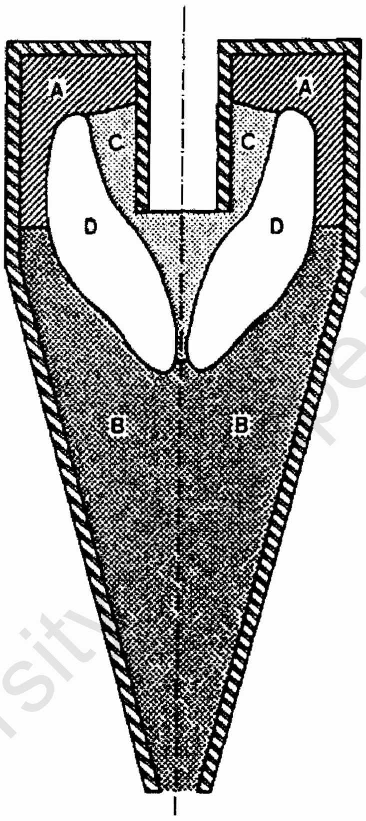

Figure 2.10: Hydrocyclone variable particle size spatial distribution [3]

The flow field of a cyclone is reportedly [6] [17] [38] asymmetric about the central axis. Consequently, the axisymmetry in particle size distribution depicted in figure 2.10 is unrealistic. Similar numerical results, which are based on Maxey's theorem, are also reported by Dyakowski and Williams [39]. The limitations imposed on the simulation of high solids concentration flows via computational fluid dynamics (CFD) are reported by Slack [7], Olson and Van Ommen [19] and Nowakowski et. al [38]. However, *Electrical Impedance Tomography* (EIT), a technique that maps solid particle and fluid media distributions on the basis of their electrical properties, offers promising prospects but has only been used to map cyclone flow fields in horizontal planes [34]. Details of this technique are discussed in section 2.1.4 (a).

2.1.3 Pressure drop across the hydrocyclone

The *total pressure* at any point in a cyclone is the sum of the *static pressure* and *velocity pressure* at that point [40]. Numerous factors reportedly contribute to cyclone pressure drop but the most noteworthy, which also consumes energy during its formation [40], is the Rankine vortex. In accordance with Bernoulli's principle, which is a statement of conservation of energy of a physical system, velocity changes across sections of non-uniform cross-sectional area, are accompanied by inverse pressure variations in the flow direction [36]. With particular reference to cyclone flow, when pressurised slurry is fed into the main chamber of the hydrocyclone, it experiences a high swirl motion that results in radial acceleration of the particles. The particle accelerations, due to increased bulk flow velocity, inevitably set up a negative pressure differential between the cyclone inlet and any downstream position within the body of the cyclone. Of interest is the pressure drop that leads to the formation of a central air core, which has already been discussed in section 2.1.2 (d). The pressure drop across the inlet and discharge ducts is also significant, due to its tendency to impose high energy expenditure pumping requirements. Unfortunately, despite the much needed knowledge of the pressure variation across the cyclone, of all the numerous empirical, semi-empirical and theoretical cyclone pressure drop relationships that have evolved, none proves to be universally applicable [40].

2.1.4 Current experimental research techniques

The discussion on current experimental research techniques is limited to *Electrical Impedance Tomography* (EIT) and *Laser Doppler Anemometry* (LDA), which are used to determine the spatial distribution of fluid and particulate media within a hydrocyclone flow field as well as to measure fluid velocity, respectively. Details of the experimental work due to Hsieh [6], which employed LDA and that which provides the necessary input used to set up the CFD models in this work, are also discussed.

a) Electrical impedance tomography

The multiphase flow imaging capability of EIT offers great potential for fluid flow model validation, separator design and on-line process monitoring [34]. The advantage derived from the application of EIT in mapping hydrocyclone flow media is that the acquistion of measurements is not impeded by the opacity of the feed slurry [34]. Measurements are also taken non-intrusively and rapidly, suggesting that rapid (e.g 2ms per frame) flow fluctuations can be measured [34].

EIT is implemented by mounting plate electrodes around the periphery of the cyclone and measuring the slurry voltage on horizontal planes [34] [35]. Measured voltage data, captured via a data acquisition system, is then interpreted using a quantitative image reconstruction algorithm and tomographic images giving a map of the constituent phases obtained [35]. Comprehensive accounts of EIT and generic image reconstruction algorithms and their limitations are presented by Williams et. al [35] [41].

b) Laser Doppler anemometry

LDA is an optical technique used for localised velocity measurements of small tracer particles suspended in a flowing fluid. Tracer particle velocities are established via the determination of the *Doppler shift* or laser light scattered from the moving particles. Doppler shifts refer to the frequency changes that occur in any form of wave propagation, owing to the relative motion of a *source* and a *receiver*. This discussion is due to Drain [42] and is limited to the *Differential Doppler Technique* (DDT).

The DDT employs two laser beams of equal intensity, which are focused by a single lens and crossed at the point under investigation. The light scattered from the focal point is then focused onto a photodetector. On account of this light reaching the photodetector simultaneously, a *beat frequency* that is equivalent to the difference in Doppler shifts corresponding to the two angles of scattering is obtained. The beat frequency f_b is given by equation 2.6. Several means, which include spectrum analysis, are available for processing the photodetector output signal. DDT permits light collection over a wide aperture and offers considerable signal to noise advantage for low particle concentrations.

$$f_b = \frac{2u}{\lambda}\sin\left(\frac{\alpha}{2}\right) \tag{2.6}$$

where

f_b – beat frequency
u – tracer particle velocity at focal point
α – angular displacement between scattered beams
λ – light source wavelength

The most significant limitation of LDA is its dependence on the presence of particles in the flow, which may be prohibited and/or undesirable in certain instances. Provision should also be made to grant optical access to the area of interest via transparent inteverning media. The application of LDA, however, presents no obstruction to the flow and permits high resolution that is typically of the order of 20 - 100 μm. In addition to being a high response technique, LDA also permits directional discrimination of tracer particle velocities.

c) Laser Doppler anemometry experimental details

Figure 2.11 depicts a schematic of Hsieh's [6] experimental set up. The laser system was affixed to a three-dimensional traverse system, with digital tracking of spatial coordinates, accurate to 0.01 mm. The laser beam was split into two beams of equivalent intensity by a beam splitter. A focussing lens, collecting lens and pin hole, in turn, focussed, collected and localised the coherent light source onto a photo detector, which converted the light energy into electrical energy. The water jacket served to minimise optical refraction of the incident light beam. The frequency shifter detected the flow direction and measured the velocity of the tracer particles within the fluid media. The resulting Doppler signals were displayed on the oscilloscope and converted into a voltage signal via the signal processor. The data processor converted the output to velocity data.

Hsieh [6] employed LDA with a 75-mm glass hydrocyclone to measure the axial and tangential velocity components of water, in the presence of an air core. With respect to figure 2.12, the tangential velocity measurements were taken at 0^0 and 180^0, and the axial velocity measurements at all the indicated 90^0 intervals. All velocity measurements were taken at specific horizontal levels. Fluctuations in the air core prohibited measurement of the radial velocity component hence its computation from continuity, using the measured axial and tangential velocities. Mass flow rates at the inlet duct, vortex finder and spigot discharge orifices were also measured. The overflow and underflow streams were discharged at atmospheric pressure into the sump and recirculated via the pump. Figure A.1 depicts the cyclone used for the experiment and details of its physical dimensions are given in table A.1. Hsieh's [6] high quality experimental data set was selected for this work because it is published in a manner suited to validation of the multiphase CFD hydrocyclone models.

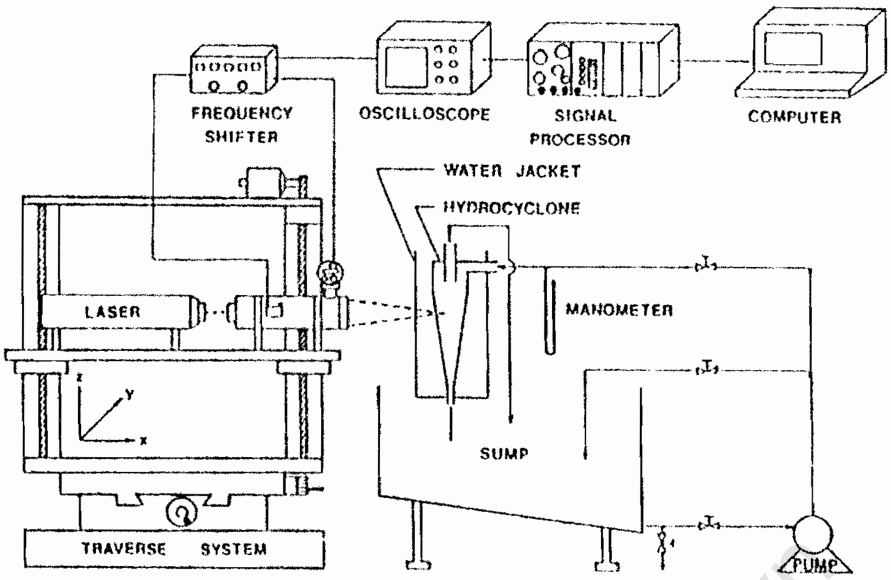

Figure 2.11: Hydrocyclone - laser-Doppler anemometry system [6]

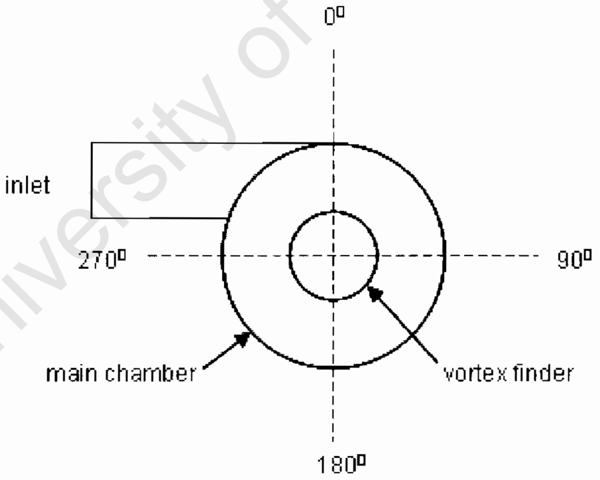

Figure 2.12: Angular definition with respect to LDA system [6]

2.1.5 Summary

Classification has been established as being imperative to numerous industrial processes, more so where it impacts directly on the final product yield. Consequently, an attempt has been made to justify the reason why classification devices such as the hydrocyclone that contribute directly to the revenue generated in such industries, receive much deserved attention, aimed at improving their operation efficiencies. Fundamental concepts relating to hydrocyclones have therefore been discussed in section 2.1 in order to provide the reader with a background on their applications and principle of operation. The inherent intricacy in the hydrodynamic behaviour of hydrocyclone flow has also been highlighted. The highly empirical nature of current hydrocyclone models has been noted and the need for continued complementary research via computational techniques such as CFD, motivated. A set of experimental data due to Hsieh [6] that can be used to validate the multiphase CFD hydrocyclone models derived from the current research has also been identified.

2.2 CFD hydrocyclone modelling

Computational fluid dynamics (CFD) is, in essence, the field concerned with the analysis of systems involving fluid flow, heat transfer and associated phenomena by means of computer-based simulation [18]. This section discusses CFD hydrocyclone modelling as reported in the literature. Without shifting focus from the set objectives of this dissertation, it is perceived instructive to give an overview of CFD as a means of providing insight into its underlying fundamental concepts. As such, if deemed appropriate, reference should be made to Appendix B, which gives a qualitative treatment of the basis of CFD. The solution techniques employed in commercial CFD codes are also discussed, with particular reference to the *finite volume* technique employed in Fluent version 6.1.22.

2.2.1 Preliminary overview

New design tools are being sought to facilitate concept design evaluation and optimisation prior to prototyping [19]. The motivation is primarily to reduce the costs involved with the design and production of machine components. Such objectives are in the realm of CFD, due to its inherent ability to facilitate parametric investigations to be conducted at relatively reduced time scales in comparison with experimental techniques [18].

Although CFD can potentially be used to investigate fluid flow phenomena in a hydrocyclone, there still exist numerous limitations to the modelling capability of commercial CFD codes, imposed by the incorporated computational algorithms and computer hardware capabilities. As a result, CFD suffers a drawback in that it cannot be professed adequately without continued reference to experimental validation [18]. For this reason and due to the inability of companies to support the high cost of computational infrastructure, CFD has lagged in mineral processing and other applications [7] [19]. However, with advances in both computer technology and computational algorithms, we remain "poor but not destitute" [43].

Despite the widespread availability of CFD technology, a high level of skill and understanding is still required to produce meaningful results using commercial CFD codes. Nonetheless, the preferential adoption of CFD over experimental techniques, in the design of fluid flow systems, may be attributed to [18]:

- the significant lead time and cost reductions associated with new designs
- the ability to computationally investigate and control systems in ways that may have otherwise proved difficult or impossible experimentally

- the ability to simulate potentially hazardous systems up to and beyond their performance limits

- the ability to simulate results with an unlimited level of detail, perhaps not observed or readily apparent experimentally

2.2.2 Current CFD hydrocyclone modelling research

Numerical solution of the intricate multiphase swirling flow field in a hydrocyclone via CFD is reportedly [7] [17] [37] [44] non-trivial. Improved understanding of the strategies necessary to tackle this problem is however being gained through continued research [19] [45]. This section discusses literature publications of current successfully implemented CFD hydrocyclone modelling strategies. Particular reference is given to experimentally validated cases that have shown good correlation to experimental data. The hydrocyclone modelling guidelines are largely due to Slack [7] and Brennan [37], both of whom have undertaken the seminal hydrocyclone CFD study, validated with experimental LDA results due to Hsieh [6]. Pioneering non-CFD work on hydrocyclone flow dynamics modelling was conducted by Hsieh [6] and co-workers Monredon et. al. [46] via a phenomenological model.

a) General overview

The extent of volume mesh resolution has a significant effect on the numerical accuracy of the resulting solution. For improved accuracy, common practice dictates increased volume mesh resolution, more so in regions exhibiting large variations in flow variables [18]. The Fluent [8] solver incorporates a dynamic self-adaptive meshing capability, for mesh optimisation in this regard. In instances where this option cannot be employed, the onus is on the CFD user to design a mesh that is a suitable compromise between the desired accuracy and solution cost. To minimise *false* or *numeric diffussion*, it is imperative to align the mesh in the flow direction [18] [21]. It is estimated [18] that over 50% of the time spent in industry on a CFD project is devoted to geometry definition and meshing of the computational domain . As such, the importance of this phase cannot be over-emphasised because of the direct relationship between the accuracy of a numerical solution and its cost in terms of the necessary computer hardware and computational time, for a specified grid resolution.

b) Established hydrocyclone-related CFD modelling practices

Some of the problems anticipated to be concerned with setting up the CFD hydrocyclone model that were highlighted in chapter 1, section 1.5.1 are re-iterated for emphasis as well as to indicate the procedures adopted to overcome or address them in part.

i) Geometry definition and meshing The existence of numerous variable cyclone geometric configurations complicates the task of attempting to establish a generic procedure for generating the geometries such that they can be meshed with suitably structured grids. The most notable complication, from a meshing perspective, is presented by some types of feed inlet designs and/or inlet duct cross-sections, examples of which were discussed in section 2.1.1 (b). Some inlet duct-main chamber configurations may dictate the use of different mesh types for the two components, which would in turn, effect non-conformal meshing at the common interface. Such a meshing strategy was adopted by Slack [7] for the outer wall tangential, circular cross-sectional inlet duct cyclone depicted in figure 2.13, the shortfalls of which he reports to be:

- high susceptibility to interpolation error, of fluxes between the different meshes at the non-conformal interface
- the need to use high order discretisation schemes and comparable mesh sizes in order to minimise the associated flux interpolation error
- marked false diffusion due to the use of different element types e.g. tetrahedral-shaped elements are more diffusive than the hexahedral type, which compounds the diffusive effects of the strongly convective hydrocyclone flow

The volume meshing complications arising from the inclusion of the inlet duct, in the definition of the cyclone geometry, could be avoided through its exclusion. A *user-defined function* (UDF) could then be used to specify a suitable input velocity profile on a boundary representing the interface between the inlet and main chamber. However, it is evident from experiment and CFD predictions that the inlet serves as a source of asymmetry and that its inclusion in the numerical modelling process is imperative for successful simulation of hydrocyclone flow [31]. Inasmuch as the prescription of a UDF for the inlet velocity profile would serve to simplify the problem, establishing a suitable input velocity expression may prove difficult, especially for high flow rates in which the flow may not be fully developed on entrance into the main chamber.

Three-dimensional meshes that were aligned in the flow direction, in an attempt to minimise numeric diffusion, were adopted by Slack [7] and Brennan [37] for the main body of the cyclone. Numeric diffusion, aggravated by the implementation of a Cartesian versus a cylindrical coordinate system, for the purpose of modelling a

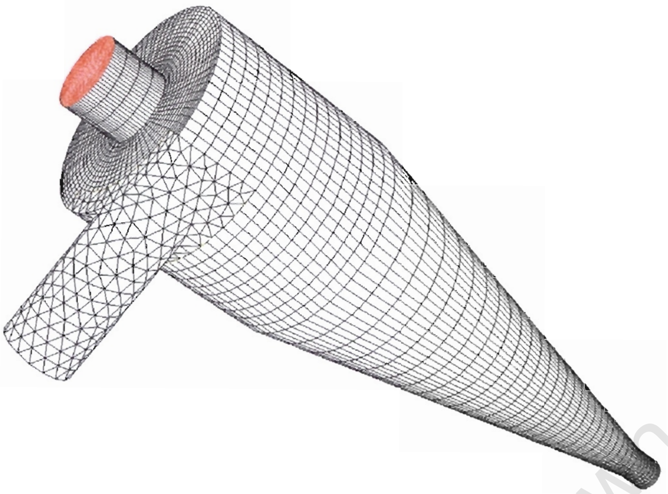

Figure 2.13: Non-conformal inlet-duct main chamber mesh [7]

cylindrical geometry [47], was further minimised through the application of high order discretisation schemes. A critical factor in deciding on the mesh resolution is ensuring that cell aspect ratios are moderate because high aspect ratio cells are known to cause convergence difficulties, more especially in swirling flows [48]. The general guideline [48] dictates that cells should ideally not exceed aspect ratios of 1:5. For the purpose of modelling multiphase flows, it is further required that the reference pressure location be located in the region containing the least dense of the fluids, in which the variation in static pressure is least, to reduce round off error [8].

ii) Boundary condition specification Hsieh [6] experimentally determined the volumetric flow rates of the feed, the overflow and underflow streams of the hydrocyclone circuit configuration depicted in figure 2.11, for which the cyclone discharge orifices are at atmospheric pressure. These experimental measurements and conditions are sufficient to enable adequate specification of the boundary conditions necessary for a CFD simulation of the hydrocyclone. The commonly specified boundary conditions for this set up include a velocity inlet condition at the duct inlet and pressure outlet conditions at the vortex finder and spigot discharge orifices [7] [37]. A no-slip wall boundary condition [49] is also specified for the remainder of the cyclone.

In as far as boundary condition specification is concerned, the following is generally advised [7] [48]:

1. The adoption of wall functions for boundary layer resolution [50], which is justifiable due to:
    (a) turbulence being generated in, and remaining restricted to, the main flow
    (b) the lack of experimental data of boundary layer flow, for validation of the CFD models, as a result of the difficulty involved with the experimental measurement of flow quantities such as velocity components close to the cyclone wall [6]
    (c) the predominant occupation, by coarse particles, of the region near the vicinity of the wall, in practical applications
2. Fine grid resolution of the spigot orifice in order to adequately capture the underflow in the event that an annular gap, due to the formation of an air core, is established in the spigot.
3. The specification of radial pressure distribution at the vortex finder and spigot discharge orifices, for the adequate resolution of the radial pressure gradients generated due to high swirl of the cyclone flow [47] [49].

In his CFD cyclone studies [37], Brennan [50] employed non-equilibrium wall functions, for boundary layer resolution but suggested that the implementation of standard wall functions, although not investigated, was potentially adequate. In contrast, Slack [7] took precaution and adopted the more conservative boundary layer meshing approach for the near-wall region.

iii) Turbulence modelling The standard k-ϵ model has been found unsuitable for modelling the anisotropic turbulence exhibited by hydrocyclone flows [7] [37] [44] due to its simplifying assumption which enforces equality of the normal Reynolds stresses, thus rendering the flow isotropic [17]. The high swirl due to the Rankine vortex, already discussed in section 2.1.2 (e), introduces marked instability of the tangential velocity component [7], leading to its inaccurate resolution by the standard k-ϵ model [19]. The RSM has been shown to represent the minimum order of accuracy for modelling hydrocyclone flow turbulence, through successful implementation with both single and multiphase flows [7] [37]. Experience shows that a significant number of iterations are required before stability of the peak tangential velocity component is attained, even with the RSM [7] [47]. The numerous unstable flow features of hydrocyclones are only adequately resolved through transient calculations [37] [47], using a time step at least 100^{th} of the cyclone residence time [7]. A transient pattern is observed if the hydrocyclone flow is resolved through steady state simulations and this is evidenced by a cycling in the residuals [7]. The LES model provides an alternative to the RSM but is computationally more expensive [51].

iv) Multiphase modelling Most CFD modelling of hydrocyclones has been limited to single phase flow i.e. water only [52], which is without the added complication and computational expense involved with modelling the air core and solid particles [7]. An air core is reportedly [34] established through the introduction of air as a component of the feed and adequately resolved as a dispersed phase via the Algebraic Slip Mixture Model (ASMM) [37]. This has been achieved [37] through the specification of a volume fraction of unity at the cyclone discharge orifices, a condition which ensures that only air recirculates across the outlet boundaries, accumulates and segregates along the cyclone central axis, establishing an air core. The formulation and solution technique of the ASMM are discussed in Appendix B, section B.1.2 (b).

v) Constitutive equation discretisation The fidelity of CFD predictions of hydrocyclone flow is largely dependent on the choice of the discretisation schemes employed in the discretisation of the convective terms contained in the fluid flow transport equations [48]. Despite the existence of a wide range of discretisation schemes, only the first, second and third order accurate ones, which are widely validated, are commonly implemeted in the solution of fluid flow systems [18]. The *pressure staggered option* (PRESTO) finds wide use in the spatial discretisation of the pressure field [49]. The benefit to using the PRESTO option, for which a structured grid is a co-requisite [49], is that the pressure and velocity fields are stored on staggered grids [18]. Consequently, reconstruction of the pressure field, via interpolation at each iteration during the solution process, is averted [49]. Any spatial oscillations exhibited by the pressure field are also discerned so that physically realistic pressure field predictions result [18]. The continuity and momentum equations are commonly coupled via the *Semi-Implicit Method for Pressure-Linked Equations* (SIMPLE) [44] [53] and SIMPLE-Consistent (SIMPLEC) [49] algorithms. The second order upwind differencing scheme [37] [44] and the third order accurate *Quadratic Upstream Interpolation for Convective Kinetics* (QUICK) scheme [49] [53] have been utilised in the discretisation of velocity and turbulent quantities. The upwind differencing scheme is suited to modelling strongly convective flow behaviour [18] such as that exhibited by hydrocyclones, due to its inherent ability to identify flow direction. The QUICK scheme offers an alternative discretisation scheme of a much higher accuracy.

c) Reported CFD hydrocyclone modelling solution strategies

The literature lacks detailed information on the CFD modelling solution strategies of hydrocyclone flow, especially with regard to air core development in multiphase flow simulations. Schuetz et. al. [44] and Slack et. al. [53] have suggested initialising the simulation with a steady state solver, using the RSM for turbulence closure. This solution strategy, which assumes a laminar flow field, is associated with tremendeous solution instability that is coupled with divergence behaviour [44]. Solution stability is therefore achieved by initialising the simulation at a volume flow rate lower than the operating value, to which it is gradually increased, during the iteration process [44]. The resulting velocity and pressure profiles were found to exhibit a physically sensible local distribution but compared poorly to experimentally determined values, with the pressure drop commonly under-predicted by a factor of two or three [44]. Further inadequancies due to the resolution of the hydrocyclone flow field via a steady state solver have already been discussed in section 2.2.2 (b).

The subsequent implementation of an unsteady state solver, for the transient solution of the hydrocyclone flow field, does not guarantee solution convergence. Several key factors, which include the extent of flow development and grid resolution as well as the choice of the simulation time step also need to be taken into consideration to ensure solution stability and convergence. The choice of a simulation time step is often of paramount importance in this regard and a conservative time step of 10^{-5} s is indicated [44] [50] [53] to be generally appropriate for the simulation of hydrocyclone flow. In the interest of reducing simulation time spans, Brennan [50] suggests a gradual increase of the simulation time step up to a value of 10^{-3} s. Brennan [37] has also suggested the use of a water-only solution flow field, with a negative pressure at the core [50], as input for hydrocyclone multiphase flow simulations. He reports [50] a premature excecution of this solution strategy to lead to diverged solutions. The only documented solution strategy for air core development, based on the literature survey conducted by the author, has already been discussed in section 2.2.2 (b).

It is required to give careful consideration when modelling the pressure strain term i.e. term IV, via the Reynolds stress equation given by the relation in equation B.16 [49]. The modelling considerations are particularly significant with high swirl flows for which the correlation between the fluctuating pressure and velocity is sensitive [49]. A comparison of hydrocyclone flow field predictions due Cullivan et. al. [31] identified the quadratic pressure strain model as a lower bound for turbulence modelling of hydrocyclone flow [49], in contrast to the linear pressure strain model. It is suggested by Brennan [50] to employ the linear pressure strain model in order to mantain solution stability and to switch to the more sensitised quadratic pressure strain model on formation of a stable air core.

d) CFD cyclone modelling limitations and developments

The software and/or algorithm limitations, which pose a challenge for both current and future CFD hydrocyclone dynamics research were highlighted in chapter 1, section 1.5.1. Recent developments in computational algorithms pertinent to multiphase flows offer promise for alleviating some of the problems associated with the numerical simulation of these type of flows. This section discusses the development of an Eulerian-Eulerian multiphase algorithm for use with the RSM.

The current Fluent [8] implementation of the ASMM employs the Euler-Langrange approach, when used in conjunction with the RSM, for the numeric modelling of turbulent multiphase flows [47]. Despite the successful implementation of this approach in hydrocyclone flow modelling, it is reported by Fluent [8] and Slack [7] to be unsuitable for modelling flows in which the volume fractions of any secondary phases are in excess of 10% by volume. Unfortunately, such conditions are typical of practical slurry feed concentrations. A complete Eulerian-Eulerian multiphase algorithm, which solves disctinct momentum equations for each secondary phase, represents the most definitive methodology currently available for modelling hydrocyclone flows with phasic volume fractions representative of typical operating conditions [7] [52]. Recent work due to Cokljat et. al [52] employed an Eulerian-Eulerian algorithm, coupled with the RSM, in the study of hydrocyclone flow that consisted of six phases. This work, which formed part of the development phase of an updated version of the Fluent version 6 solver [47], has enabled the extension of CFD hydrocyclone modelling to high and medium density flows [52]. Advances in cyclone modelling using unstructured grids are also reported by Slack et. al. [53].

2.2.3 Summary

The prerequisite for the realisation of physically realistic fluid flow predictions of any fluid dynamics problem is a thorough knowledge of the physical behaviour of the system. Some key aspects, which are essential for successful CFD hydrocyclone modelling have been highlighted in conjuction with the associated challenges. The need to model the hydrocyclone in a three-dimensional domain with hexahedral mesh elements aligned with the circumference of the cyclone and in the flow direction, so as to minimise numeric diffusion, has been identified [48]. The appropriate choice of a turbulence model that is suited to the purpose of accurately capturing the free to forced vortex transition, which is associated with anisotropic turbulence, has also been discussed. The role of discretisation schemes in minimising numeric diffusion and providing suitable coupling between the fluid flow governing equations has also been mentioned. Transient simulations, although sensitive to the extent of grid resolution and the choice of simulation time steps, have also been noted to improve solution stability and the definition of the central low-pressure core [48].

The limitations imposed on current CFD techniques have also been discussed. Perhaps worthy of mentioning is the fact that despite these limitations, meaningful results on hydrocyclone flow dynamics have been derived [7] [37] [44] [52]. Some of the challenges still facing CFD hydrocyclone modelling stem, in part, from the inability to acquire experimental data that represents realistic boundary conditions for a CFD model [48]. Single point measurements of static pressure, made at cyclone discharge orifices are, for example, not representative of the radial pressure distribution effected at these orifices due to the swirl [48]. The difficulty associated with modelling the air core also imposes a serious restriction to the usefulness of CFD hydrocyclone models because cyclones commonly operate with air cores, which are fundamental to their operation because they determine the flow split to the overflow and underflow [48]. For CFD modelling purposes, it is suggested [48] not to prescribe the mass split to these streams, even if the mass flow rates of the overflow and underflow streams are known, because the problem becomes over-constrained. Despite only having highlighted the fundamentals related to hydrocyclones, it is hoped that the intricacy involved with the CFD modelling thereof, has been adequately motivated.

Chapter 3

CFD Methodology of Solution

This chapter outlines the key aspects of the CFD hydrocyclone model geometry generation and meshing procedures adopted. The discussion focuses on the iterative development of the mesh and motivates the final choice thereof. The methodology of solution is also presented and is discussed in terms of the implemented boundary conditions and the iterative establishment of suitable solution strategies for single phase (water-only) and multiphase (water/air) flow modelling. Emphasis is placed on the procedural methodology adopted in attempting to develop the multiphase model, which is aimed at providing an understanding of the mechanism for inception and development of the air core. The rationale used in devising the exploratory and adopted solution strategies is, together with the decision to implement the selected numerical models and governing transport equation discretisation schemes, motivated.

A first order accurate pressure strain Reynolds Stress Model (RSM) and the homogeneous implementation of the Algebraic Slip Mixture Model (ASMM) were used for turbulence and multiphase flow modelling, respectively. The procedures adopted in order to establish computationally economic solution strategies, in accordance with the research objectives, are highlighted. The choice of the circular inlet hydrocyclone geometry depicted in figure A.1, which imposes difficulties with meshing, was motivated by the availability of a good experimental data set due to Hsieh [6], which provides the means for validation of the multiphase CFD hydrocyclone models. To investigate inlet geometry effects, flow field predictions are derived from identically-sized circular and rectangular inlet hydrocyclones and the outputs contrasted in chapter 4. The exploratory meshing and flow field simulation strategy investigations are conducted via the circular inlet hydrocyclone and their rigour tested via the rectangular inlet geometric configuration.

3.1 Iterative development of solution strategies

This section outlines the ideas explored with both geometry generation and meshing. The solution strategies are discussed with respect to the Reynolds Stress Model (RSM) and the Algebraic Slip Mixture Model (ASMM) that were used for turbulence and multiphase flow modelling, respectively.

3.1.1 Geometry generation and meshing

a) Geometry generation

The basic cyclone geometry used for the CFD model is depicted in figure 3.1, with respect to the *global* coordinate system. For simplicity, the external duct connection to the vortex finder is modelled as a 25mm protrusion and the wall thickness of the vortex finder is neglected. The origin of the *local* coordinate system is located along the central axis, in the plane of the roof of the cyclone. The positioning of this origin is functional because it also serves as the reference pressure location. The significance of the spatial position of the reference pressure location, with regard to multiphase flow modelling, was discussed in section 2.2.2 (b). The top-down geometry generation approach was adopted in generating the hydrocyclone CFD model i.e. geometry components were created using standard geometry primitives that were subsequently manipulated via boolean operations, in order to establish the required cyclone geometry. The basic cyclone geometry depicted in figure 3.1 was further subdivided into smaller constituent volumes, in accordance with the adopted meshing strategies, which are discussed in the subsequent section.

b) Meshing

Some of the aspects that are considered critical with respect to the meshing of cyclone geometries that have already been discussed include the difficulties associated with meshing the various inlet-main chamber geometric configurations. The shortfalls of non-conformal meshing were highlighted [7] in line with this consideration, in section 2.2.2 (b). The importance of including the inlet duct in defining the geometry of the CFD hydrocyclone model, due to the asymmetry it introduces to the internal flow structure [6], has already been pointed out [31]. The difficulty associated with defining a suitable velocity profile via a user-defined function (UDF) at the equivalent of an inlet-main chamber interface has also been addressed. Alignment of the grid in the flow direction [18] [21] [48] and the appropriate selection of discretisation schemes [47], for the purpose of minimising numeric diffusion, were also emphasised. Further grid-related requisites that include the design of grids consisting of low aspect ratio

Figure 3.1: Basic CFD cyclone model geometry

cells, in order to ensure numeric stability of the solution [18], were identified. The meshing requirements of the viscosity-affected near-wall region were, in the context of turbulence modelling, also discussed with respect to adoption of the wall function and boundary layer meshing approaches. This section therefore discusses the devised meshing concepts, which were aimed at addressing the above-mentioned mesh-related problem specifics.

i) Inlet-main chamber meshing The tetrahedral element meshing scheme (TGrid) [8] constitutes the default meshing scheme of the cyclone inlet duct depicted in figure 3.1, by virtue of the ease with which tetrahedral elements can be mapped onto the highly skewed portion of the geometry. An example of a non-conformal inlet duct-main chamber meshing configuration is depicted in figure 2.13. The use of tetrahedral mesh elements is, however, undesirable due to their relatively high numeric diffusion capacity [7]. A hexahedral mesh therefore presents a better meshing option because it allows for flow direction alignment of the grid, particularly in the main body of the cyclone, in addition to averting non-conformal meshing at the cyclone inlet-main chamber interface.

To enable hexahedral meshing of the inlet duct, its longitudinal face was bisected horizontally and vertically via planes parallel and perpendicular to the roof of the cyclone, respectively. The *vertex types* of the *vertices* located along the longitudinal bisectors, which lie in the vertical plane, were subsequently converted from *sides* to *ends*, in order to enable the application of the *mapping scheme* (Hex-Map) [8] on the longitudinal inlet duct faces as well as the overall hexagonal element meshing (Hex/Wedge-Cooper) [8] of the inlet duct. The dual perpendicular planar bisection of the longitudinal face of the inlet duct also gives the advantage of increased control in the manipulation of the longitudinal inlet duct grid density, on account of the capability of explicit node allocation along the established longitudinal edges. The structural regularity of the grid at the inlet face to the inlet duct presents another factor that requires careful consideration with respect to meshing of the inlet duct, particularly in instances where solid particles are to be introduced as part of the feed. Cullivan et. al. [31] have established that solid particle trajectories are largely influenced by the point of entry at the inlet face to the inlet duct. This mesh regularity-influenced bias in particle trajectories could negate particle classification analyses.

ii) Cyclone body meshing This section presents the two concepts that were considered for the purpose of meshing the main body of the cyclone and motivates the choice for, adoption, of one meshing concept over the other. Common to both meshing concepts, are meshes predominantly structured and aligned in such a manner as to capture the main flow features that include the short-circuit, the Eddy, and bulk flow swirl. Additional considerations that were made for the appropriate meshing of certain specific regions of interest are also addressed.

Meshing concept A The mesh due to meshing concept A, which represents the meshing concept initially considered, is depicted in figure 3.2. Despite the predominantly regular radial structure of this hybrid meshing configuration, its core consists of an unstructured cylindrical column that is likely to introduce numeric instability and to enhance numeric diffusion in the vicinity of the central axis of the hydrocyclone. By virtue of this region being highly unstable physically, on account of the axial flow reversal exhibited and the establishment of an intrinsically unstable air core, such numeric instability is highly undesirable because it can potentially lead to diverged solutions. In addition, the establishment of a physically realistic flow field as well as the inception, development and sustenance of an air core, may either be prolonged or prevented. In view of this potential predicament, the diameter of the unstructured cylindrical column was set small enough to ensure a maximum radial regular mesh structure while retaining an unstructured core of a radius potentially smaller than that of a fully developed air core. The choice to employ a cylindrical column of constant cross-sectional area, extending across the whole length of the cyclone, was motivated by the simplification introduced to the meshing procedure.

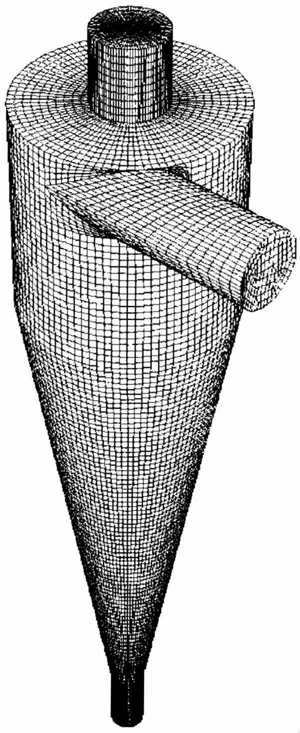

Figure 3.2: Cyclone meshing concept A

Although the choice of a certain specific diameter for the cylindrical, irregularly-meshed central column may present an optimum solution, the choice thereof is non-trivial. A restriction on the diameter of the cylindrical column is, for example, imposed by the need for significant regular mesh resolution of the spigot discharge orifice, for the purpose of adequately resolving any spray discharge likely to be effected due to the possible formation of an air core. Furthermore, on account of the 1:1 periphery edge nodal ratio of the spigot and the central cylindrical column, a higher mesh density, as depicted in figures 3.3 (a) and (b), arises at the core. Unfortunately, in order to ensure solution stability via moderate aspect ratio-sized cells at the core, it is required to construct an uneconomically fine mesh, by increasing the mesh density in the axial direction. The mesh due to meshing concept A resulted in approximately 300 000 mesh volumes, for which further refinement would present a prohibitively fine mesh, with regard to the computational resources (3.06 GHz Pentium 4 processor, 2 GB RAM).

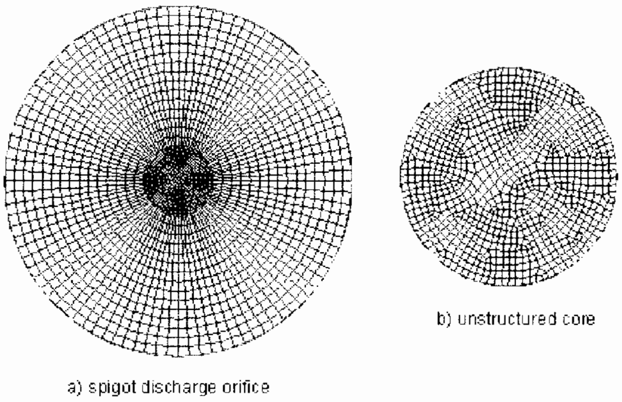

Figure 3.3: Spigot discharge orifice with irregularly structured circular core

Meshing concept B The main feature that distinguishes meshing concept B from A, is the alternative means it presents for meshing the core of the cyclone. The resulting hybrid mesh was derived by sub-dividing the basic cylone geometry, via the x-y and y-z planes, into quarter segments, as depicted in figure 3.4. The central cylindrical column from meshing concept A was replaced by two square columns, positioned within the vortex finder and the spigot and connected via a pyramidal frustrum located at the core of the conical chamber. The pyramidal frustrum tapered down from the size of the square column protruding through the vortex finder, to the size of the square column within the spigot, facilitating identical meshing of the vortex finder and spigot discharge orifices. The hybrid mesh structure at the spigot discharge orifice is depicted in figure 3.5.

Figure 3.4: Concept B geometry planar view

Similarly, the 1:1 periphery edge nodal ratio of the conical chamber ends results in a higher mesh density at the conical chamber-spigot interface, which also imposes the adoption of a prohibitively fine mesh in the axial direction, in order to ensure cells of moderate aspect ratios. Such a situation was averted through the application of a nodal distribution size function along the longitudinal conical chamber edges, which established a progressive increase in the node-to-node spacing, traversing from the spigot to the main chamber. Meshing concept B resulted in approximately 257 000 mesh volumes, which, in addition to addressing all the meshing shortfalls inherent to meshing concept A, presents a significantly more computationally economic meshing solution. The hydrocyclone CFD model mesh structure was therefore based on meshing concept B.

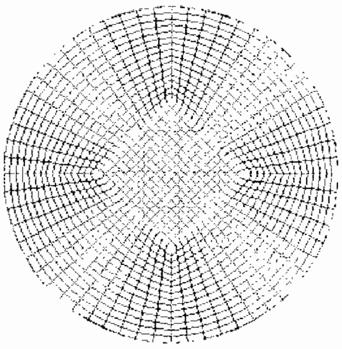

Figure 3.5: Spigot discharge orifice with regularly structured square core

3.1.2 Boundary condition specification

A system volume flow rate of 66.99 kg/min was generated [6] via a pressure drop of 46.7 kPa. The resulting magnitude of the inlet velocity of the water was computed via equation 3.1 [36], using the default [8] liquid water with density and viscosity values of 998.2 kg/m^3 and 0.001003 Pa·s, respectively. An *inlet velocity* boundary condition type and a velocity of 2.28 m/s were specified at the duct inlet.

$$\overset{\bullet}{m} = \rho A \overline{u} \tag{3.1}$$

where

$\overset{\bullet}{m}$ – mass flow rate
ρ – fluid density
A – inlet duct cross-sectional area
$\overline{u}$ – mean flow velocity

hence

Boundary	**Boundary condition type**	**Boundary condition specification**
duct inlet	inlet velocity	2.28 m/s
overflow discharge	pressure outlet	0 Pa (gauge)
underflow discharge	pressure outlet	0 Pa (gauge)
cyclone wall	wall	0 m/s (no-slip)

Table 3.1: CFD hydrocyclone model boundary conditions

$$\begin{aligned}\overline{u} &= \frac{\overset{\bullet}{m}}{\rho A} = \frac{66.99}{60\,(998.2)\,(\pi/4)\,(0.025)^2} \\ \overline{u} &= 2.28 \text{ m/s}\end{aligned}$$

Pressure outlet boundary condition types were specified at both cyclone discharge orifices at which a standard atmospheric pressure condition of 101 325 Pa (0 Pa - gauge) was specified. The radial pressure gradient that is generated due to the swirl of the hydrocyclone flow [48] was accounted for by allowing for radial equilibrium pressure distribution across the cyclone discharge orifices. A detrimental condition, which artificially suppresses the swirl and influences the internal hydrocyclone flow structure, arises if a constant pressure is, instead, specified at the discharge orifices [48]. A *no-slip wall* boundary condition was specified at the cyclone wall boundaries. A summary of the implemented boundary conditions is given in table 3.1.

The mean residence time $\overline{t}$ of the hydrocyclone, which is an important parameter for characterising the flow, was determined via equation 2.2 and found to be 0.67s, for the specified volume flow rate $\overset{\bullet}{V}_s$ of 66.99 kg/min. The geometric volume V_c of the cyclone was determined in Autodesk Inventor [54].

$$\overline{t} = \frac{V_c}{\overset{\bullet}{V}_s}$$

hence

$$\begin{aligned}\overline{t} &= \frac{V_c}{A\overline{u}} = \frac{7.502 \times 10^{-4}}{(\pi/4)\,(0.025)^2\,(2.28)} \\ \overline{t} &= 0.67s\end{aligned}$$

3.1.3 Turbulence modelling

The RSM, which was identified [7] [37] [49] to represent the lower bound for turbulence modelling of hydrocyclone flow, was implemented for turbulence closure. Standard wall

Equation	Discretisation scheme
Pressure	PRESTO
Pressure-velocity coupling	SIMPLEC
Momentum	QUICK
Volume fraction	QUICK
Turbulence kinetic energy	QUICK
Turbulence dissipation rate	QUICK
Reynolds stresses	QUICK

Table 3.2: Implemented governing transport equation discretisation schemes

functions were adopted for the near-wall treatment of the flow field. The methodology adopted in order to verify the validity of their implementation with the RSM, for the selected grid configuration, is discussed in detail in section 3.1.6 (c). The linear pressure strain model was used to model the pressure strain term in the Reynolds stress equation given by the relation in equation B.16.

3.1.4 Multiphase modelling

The ASMM, which finds wide use [19] [37] [52] in the modelling of multiphase hydrocyclone flow fields, was implemented for the two-phase (water/air) CFD simulations. The iterative development of a suitable multiphase flow modelling solution strategy, in which the water constitutes the primary phase, is discussed in detail in section 3.1.7.

3.1.5 Constitutive equation discretisation

The importance of the appropriate selection of the discretisation schemes used for the numerical prediction of the hydrocyclone flow field, was emphasised in section 2.2.2 (b), with respect to reports presented in the literature. Unless otherwise specified, the governing transport equations were discretised as indicated in table 3.2.

3.1.6 Iterative development of single phase flow solution strategy

The single phase solution represents a water-only simulation. Although it is suggested [44] [53] to initiate the solution flow field with a steady state solver, insufficient detail is given on the appropriate input parameters necessary to obtain a converged solution. Attempts to initiate the simulation at inlet velocities less than the operating value of 2.28 m/s, as suggested by Schuetz et. al. [44], gave diverged solutions. Solution convergence via a steady state solver was thus achieved through the application of under-relaxation factors of 0.35 and 0.5 to the momentum and turbulent viscosity equations, respectively. The flow was subsequently simulated transiently, with convergence criteria of 0.001 specified for all solution variables.

a) Progression of steady state single phase flow solution

The convergence history of the solution is depicted in figure 3.6, with respect to continuity and the three velocity components. Convergence plots of the turbulence kinetic energy, the turbulence dissipation rate and the Reynolds stresses, which are bounded by continuity, are omitted for clarity. As indicated, the solution appears to converge up to approximately 2500 iterations, beyond which divergence is initiated, before the residuals level off in a cyclic fashion. This point of transition represents the period during which flow reversal across the spigot discharge orifice is effected, supposedly due to the development of a negative pressure within the spigot, as depicted in figure 3.7. On account of this destabilising axial flow reversal, solution divergence ensues, as indicated by the residual plot of the axial velocity component. From a mass conservation perspective, flow reversal across the spigot discharge orifice implies that mass "accumulates" within the hydrocyclone i.e. the mass flow rate at the inlet is not equivalent to the combined discharge flow rates, hence continuity is not conserved. The divergence in the continuity residual plot is testament to this fact.

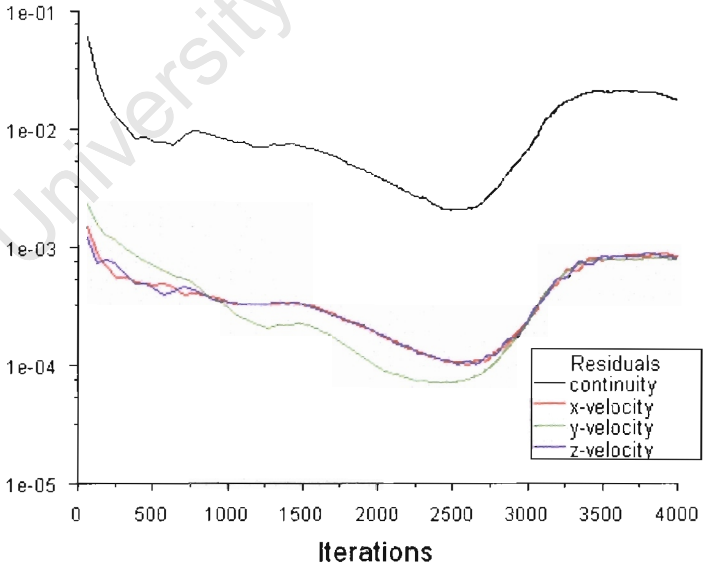

Figure 3.6: Convergence history of single phase flow simulation

The steady state solution was simulated for a total of 9000 iterations. Despite knowledge of the transient behaviour of hydrocyclone flow, the steady state solver was implemented with the primary objective of achieving economy with the overall simulation time. It was also intended to develop physically realistic velocity and pressure field profiles, before employing the relatively computationally expensive unsteady state solver. The stipulated convergence criteria were dissatisfied via solution with the steady state solver. The overall progression in flow development and the justification of the adoption of the transient solver are discussed in the subsequent section.

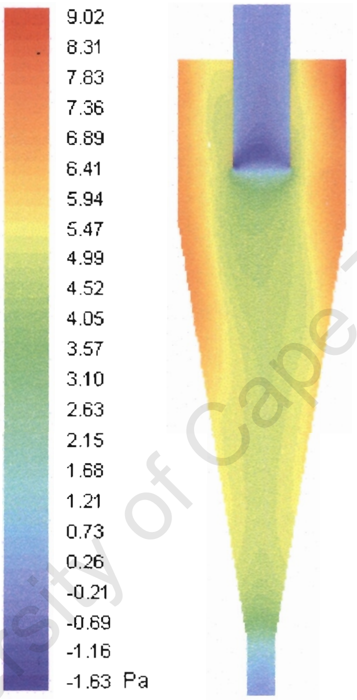

Figure 3.7: Predicted vertical planar start-up condition pressure profile

b) Progression of transient single phase flow solution

The inadequancy of the steady state solver in resolving transient flow was indicated by a cycling in the residuals as reported by Slack [7]. At this juncture, the transient solver was subsequently employed, with an optimum simulation time step of 10^{-3}s. In order to achieve convergence, it proved neccessary to switch from single to double precision numerical represantation. A total flow time of 1.5s, which is approximately equivalent to two mean residence times, was simulated over a seven and a half-day period, with convergence at each time step. The significance of the total simulation period is that it permits meaningful predictions to be derived because it is greater than the maximum particle retention period, which was assumed to be equivalent to the total time taken by a particle to travel from the inlet to the spigot and back up such as to be discharged with the overflow stream.

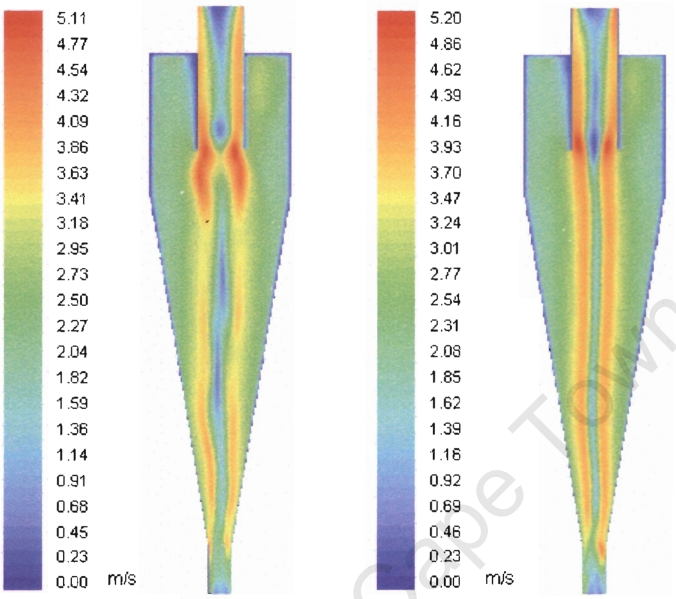

a) steady state (9000 iterations)

b) transient (1s)

Figure 3.8: Comparison of steady state and transient vertical planar velocity profile predictions

In accordance with reports due to Slack [7] and with reference to figures 3.8 and 3.9, the adoption of the transient solver improved the definition of the velocity and pressure field profiles, respectively. The steady state solution also indicated 8000 iterations to be sufficient for developing a negative core pressure, which otherwise subsequently diminished. A converged and numerically stable solution was obtained for a further two mean residence times, without significant changes in the velocity and pressure field profiles. All pressure profile plots depict pressures that are relative to an atmospheric pressure value of 101 kPa (101 325 Pa).

c) Grid considerations with respect to near-wall flow treatment

A y^* value of 14.383 was found after transient resolution of the hydrocyclone flow field over a simulation period of 1s. Such a considerable deviation in y^*, from the recommended lower bound value of 30, signifies that the adoption of the standard wall function approach is highly inappropriate, for this specific grid configuration. Since $y^* > 11.225$, a turbulent boundary layer is assumed, and the mean fluid velocity at all near-wall nodes P is determined via the logarithmic mean velocity law given by

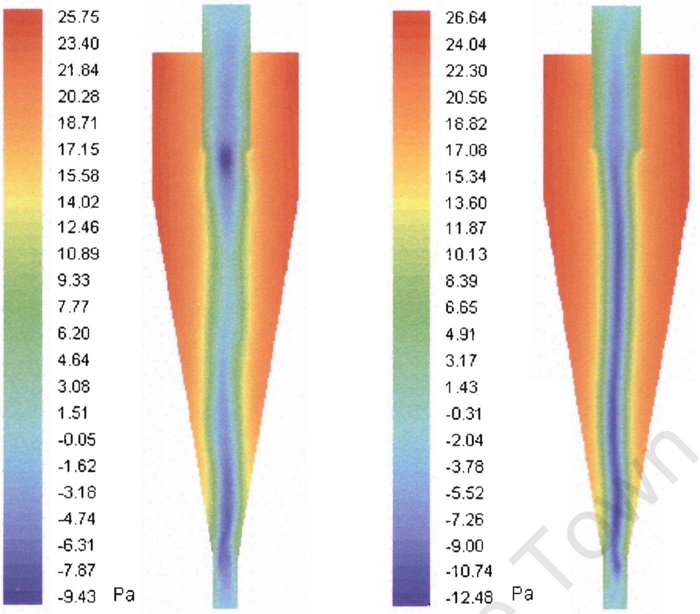

a) steady state (9000 iterations)

b) transient (1s)

Figure 3.9: Comparison of steady state and transient vertical planar pressure profile predictions

equation B.27a. Although this methodology for determining the validity in application of the standard wall function approach appears plausible, it is not rigorous. By virtue of having variable perpendicular nodal-wall distances, of the near-wall nodes P, in different regions of the cyclone, it is, in fact, misdirected to assume a global value for y^*. The deduction made on the choice of the velocity law suited for the determination of the velocities at the near-wall nodes P, on the basis of the standard wall function y^* criteria, is in fact likely to be invalid in the spigot and vortex finder regions where the mesh density, in the vicinity of the internal wall boundaries, is highest. A more rigorous approach, in which the different wall boundaries were considered in isolation, is discussed in section 3.2.1 (a).

3.1.7 Iterative development of multiphase flow solution strategy

A water-only flow field solution corresponding to a flow time of 1s, was used to initiate the multiphase (water/air) flow simulation. In accordance with reports due to Brennan [50], use of a water-only flow field solution with an adequately developed sub-atmospheric core pressure, as input for the hydrocyclone multiphase flow simulation, proved necessary in order to obtain a converged solution.

$$\begin{aligned} V_{f_{air}} &= \frac{V_{air}}{V_c} \\ V_{f_{air}} &= \frac{3.817 \times 10^{-5}}{75.02 \times 10^{-5}} \\ V_{f_{air}} &= 5\% \end{aligned} \tag{3.2}$$

An estimate of the operating volume fraction of air $V_{f_{air}}$, was obtained via equation 3.2, by approximating a fully developed air core as a cylindrical air column of spigot diameter, extending across the length of the cyclone. On the basis of this assumption, an air volume fraction of 5%, which is half the 10% by volume of a secondary phase, beyond which the ASMM is reported [7] [8] to be unsuitable for modelling multiphase flows, was obtained.

a) Preliminary multiphase flow investigations

To account for the conglomerate volume fraction of the air that may be dispersed in the bulk flow, an operating volume fraction of air of 9% was assumed and introduced at the inlet, as part of the feed. The boundary conditions given in table 3.1 were implemented with two multiphase models, run in parallel, which employed the slip velocity and homogeneous formulations of the ASMM, respectively. An inlet velocity of 2.35 m/s was specified, for the 2.5 mm diameter particles of the secondary phase, with the multiphase model which employed the slip velocity formulation. A simulation time step of 10^{-4}s was identified as optimum and as much as 500 iterations per time step, were allowed for, in order to ensure solution convergence at each time step.

Upon entry into the main chamber, of the air introduced at the inlet, the backflow volume fraction of air was set to unity, at both the spigot and vortex finder discharge orifices [37], in order to artificially develop an air core. However, the investigations revealed that in order to obtain a converged solution, the backflow volume fraction of air at the discharge orifices had to be increased gradually from zero to unity, only at this juncture. Successive increaments of 0.25, at every one quarter period of the residence time, proved sufficient to satisfy convergence conditions. Nonetheless, the hydrocyclone flow field remained largely unchanged and no air core inception was observed at the spigot, with either solution strategy, over a simulation period of approximately two residence times. As expected, the solution employing the non-homogeneous implementation of the ASMM, proved computationally more expensive due to the additional slip velocity equation requiring solution, for the secondary phase particles. Unless otherwise specified, the generic aspects of the strategy established during this iterative solution strategy formulation process, will be employed for the multiphase flow models. The subsequent section discusses a strategy which led to the successful simulation of air core inception.

b) Preliminary multiphase flow solution strategy

In the interest of achieving economy with simulation run times, the homogeneous implementation of the ASMM was employed with the multiphase flow CFD hydrocyclone model. The operating volume fraction of air was increased to 50%, despite the estimated operating value of 5%. This was done with the intention to expell, into the atmosphere, any excess air not contributing to the formation of the air core nor to the volume of air remaining entrained in the bulk flow, during the artificial air core development process. In a manner consistent to experimentally observed phenomenon, air core inception was initiated at the spigot discharge orifice. Figures 3.10 (a) to (c) depict an increase in the normalised volume fraction of air admitted via the spigot discharge orifice, across which significant recirculation persists. The blue-coloured region is indicative of an atmospheric spray discharge of liquid water. The instance at which a significant portion of the area across which recirculation is exhibited, was predominantly occupied by air, as depicted in figure 3.10 (b), is represantative of the juncture at which a value of unity was specified for its backflow volume fraction, across both discharge orifices.

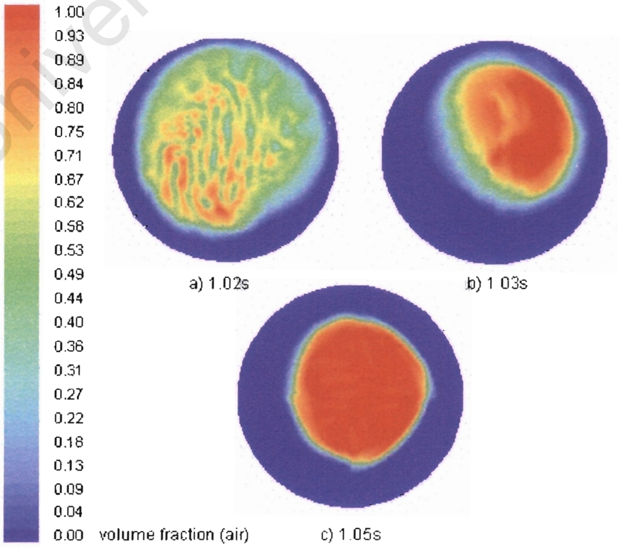

Figure 3.10: Normalised spigot discharge orifice air volume fraction profiles

Accordingly, solution instability and divergence occured due to the inherently unstable air core formation process and the lack of conservation of continuity, respectively. To mantain a converged solution at an optimum simulation time step of 10^{-3}s, the convergence criteria of all the solution variables were relaxed to 0.05, at the instance where the recirculation of air across the discharge orifices was initialised. Continued air core development and sustenance were achieved by progressively relaxing the convergence criteria, at the point of solution divergence. All convergence criteria were relaxed to a final value of 0.0625, beyond which solution convergence could not be achieved, even with variable and smaller simulation time steps of up to 10^{-6}s.

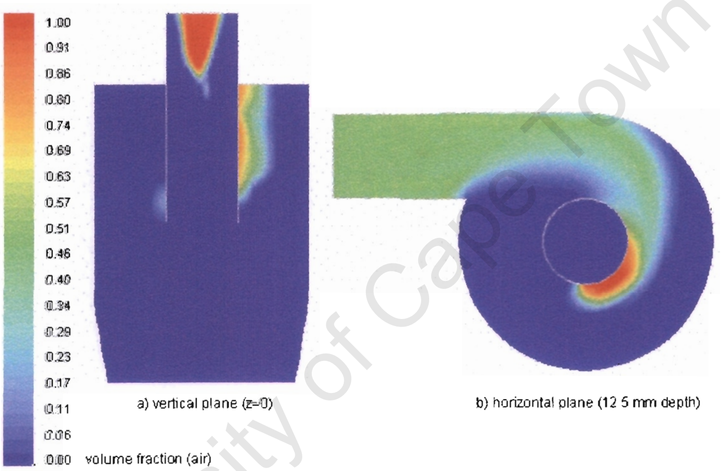

a) vertical plane (z=0)

b) horizontal plane (12 5 mm depth)

Figure 3.11: Artificial vortex finder air core inception and inlet feed air trajectory

Upon entry into the main chamber, the air-water mixture introduced at the feed inlet is deflected radially outwards by the incident swirling flow field, as depicted in figure 3.11 (b). Subsequently, on account of the radial pressure gradient and the differential operating media densities, the less dense air stream is conveyed radially inwards by the clockwise swirling fluid motion. Following this, it is then trapped against the outer wall of the vortex finder, along which the constituent bubbles coalesce and segregate. When this air rich flow stream short-circuits as depicted in figure 3.12, it reinforces with the artificially induced air core that is prevalent within the vortex finder. This flow mechanism, which is inherent to hydrocyclone flow dynamics, is indicative of the potential for the successful implementation of this strategy, in the artificial development of the air core from both discharge orifices. However, figure 3.11 (a), which depicts the artificially induced air core without any short-circuit flow of the air stream, seems to suggest that air core inception and development may be achieved via the introduction of little or nor air, at the feed inlet. Such a simulation strategy would result in significantly reduced computational expense. The air core inception effected at the spigot discharge orifice is depicted in figures 3.13 (a) to (d), up to the point approaching maximum air core development. The spontaneity of the air core inception event, which is indicated by the time span from the initial burst to the nearly fully developed air core, accounts for the numeric instability of the solution.

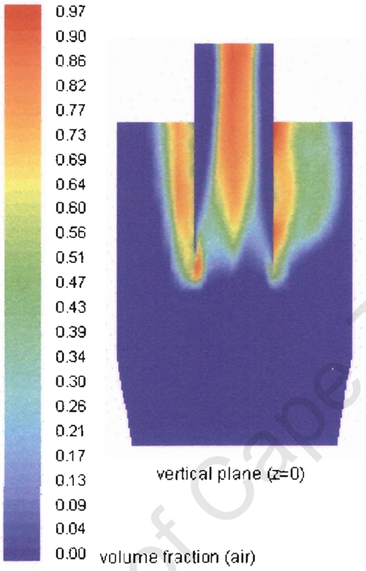

Figure 3.12: Enhanced artificial air core development

3.2 Implemented solution strategies

This section presents the solution strategies implemented with both single phase and multiphase hydrocyclone flow fields. The exploratory solution strategy adopted with the single phase flow model was also implemented with an identically-sized cyclone with a 25mm × 20 mm rectangular, outer wall tangential inlet. This exercise was aimed at providing an assessment of the genericity of the devised meshing procedure as well as facilitating the investigation of inlet geometry effects on the hydrocyclone flow field. Meshing concept B and a conformal, regularly-structured inlet-main chamber geometry mesh were employed in meshing the rectangular inlet cyclone. The grid considerations made in order to account for the near-wall treatment of the flow field are also discussed in detail. The preliminary multiphase flow solution strategy discussed in section 3.1.7 (b) was also adopted, with slight modifications, for the multiphase flow model.

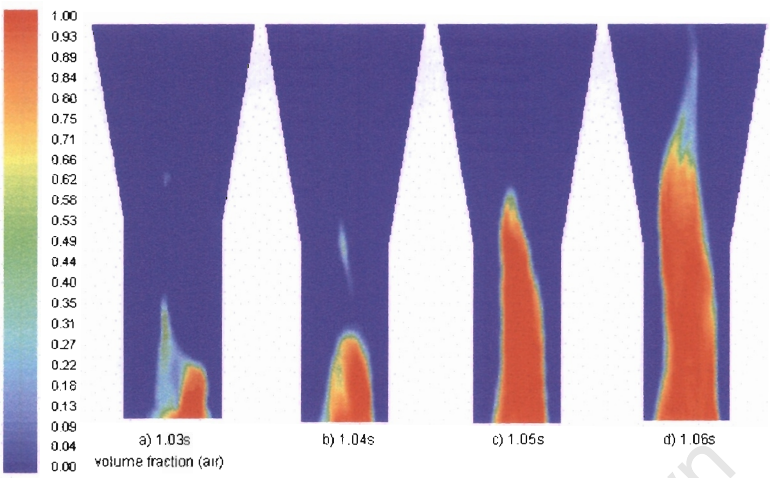

Figure 3.13: Spigot air core inception and development

3.2.1 Implemented single phase flow solution strategy

The hexahedral element meshing scheme (Hex-Map) [8] constitutes the default meshing scheme for the selected rectangular cross-sectional geometry of the cyclone inlet. As such, no geometric manipulations were implemented in order to avert non-conformal meshing of the inlet-main chamber geometric configuration. The mesh used with this cyclone geometric configuration consisted of approximately 200 000 mesh volumes and is depicted in figure 3.14. To ensure the validity of the application of standard wall functions, for the near-wall treatment of the flow field, the perpendicular distances of the near-wall nodes P from the disctinct internal wall boundaries, were increased. The pertinent details are discussed in the subsequent section, in terms of the y^* validation criteria. The results are contrasted with those of the outer wall tangential, circular inlet cyclone, for which the disctinct internal wall boundaries were considered in isolation.

a) Grid considerations for near-wall flow field treatment

As projected in section 3.1.6 (c), with reference to the y^* values listed in table 3.3, the internal wall boundaries of the vortex finder and the spigot, represent the regions where the logarithmic mean velocity law given by equation B.27a, is inappropriate for determining the velocity distribution in the near-wall region, for the mesh employed with the circular inlet cyclone. This grid-related inadequancy is also exhibited in the vicinity of the conical chamber wall. The y^* criteria, in addition to giving an indication of the expression used to approximate the velocity distribution in the near-wall region, also provides a means for evaluating the validity in its application, which determines the extent to which the boundary layer is suitably bridged, with respect to

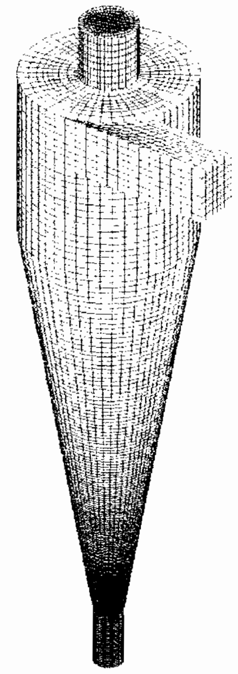

Figure 3.14: Rectangular cross-sectional inlet cyclone mesh

a specific grid configuration. Fortunately, despite grid inadequancies that may result in the inappropriate application of the wall function approach, the Fluent [8] solver reportedly [8] defaults to the laminar stress-strain relationship given by equation B.28, within near-wall region cells in which $y^* < 11.225$. The shortfall of this functionality is that any severe flow variable gradients exhibited in the near-wall regions may be inadequately resolved. Depending on the severity of the grid inadequancy, diverged or physically unrealistic solutions may result, hence the need for proper assessment of the applicability of this approach, with respect to a specific grid configuration.

A significant improvement with regard to grid generation, in the context of the adoption and the appropriate implementation of the wall function approach, is observed with the y^* values of the rectangular inlet cyclone, which are listed in table 3.3. Save for the spigot, all the y^* values after 1s of flow, are within 37.4% of the recommended [8] value of 30, in contrast to the 63% descrepancy indicated by the y^* value of the conical chamber wall of the circular inlet cyclone. The y^* results due to the meshes of the variable cyclone inlet geometric configurations, seem to suggest that the application of a boundary layer mesh within the spigot would be more appropriate. The lack of the need to adopt this more conservative approach, particularly with respect to the remainder of the internal wall structure of the cyclone, was motivated

inlet cross-section type	**circular**			**rectangular**		
simulation type	steady		transient	steady		transient
iterations/flow time	1000	9000	1s	1000	9000	1s
wall	y^* **value**					
1. inlet duct	29.983	30.050	30.048	27.151	27.193	27.189
2. cyclone roof	10.125	12.585	12.468	18.191	20.511	20.253
3. vortex finder (ext.)	10.976	15.908	15.546	19.721	28.550	27.435
4. vortex finder (int.)	7.761	11.967	11.584	13.825	25.106	25.067
5. main chamber	16.362	17.866	17.306	27.953	29.450	29.070
6. conical chamber	8.890	12.751	11.121	15.881	21.220	18.779
7. spigot	2.476	3.703	3.989	3.287	4.892	5.123

Table 3.3: Wall function validation criteria of circular and rectangular cross-sectional inlet cyclones

in section 2.2.2 (b) and is supported by the y^* results corresponding to the rectangular inlet cyclone. Given the physical dimensions of the spigot, if the associated grid were set up such as to satisfy the y^* criteria, the underflow fine spray discharge stream that flows against the spigot internal wall boundary would be inadequately resolved. However, from a practical perspective, inadequate resolution of the hydrocyclone flow field within the spigot is not critical because the indication from figure 2.10 is that no active classification occurs within its confines. In addition, the overflow stream spiral which predominantly conveys fine particles, also reverses in the vicinity of the apex of the conical chamber. Nonetheless, from a CFD point of view, this aspect is potentially critical. The results presented in table 3.3 indicate that the rectangular inlet cyclone grid configuration is better suited to the adoption of the standard wall function approach.

b) Progression of single phase flow simulation

The single phase flow simulation progressed in a similar manner to that discussed in sections 3.1.6 (a) and (b). Suprisingly, given only a 2% discrepancy in volume flow rates, the relative development of the flow field of the rectangular inlet cyclone, was marginally quicker. The relatively marginal economy achieved with the overall simulation time may be attributed to the significant variation in mesh densities. Qualitatively consistent velocity and pressure field profiles were obtained with both cyclone geometric configurations and quantitative comparisons of the flow field variables are drawn in the subsequent chapter.

3.2.2 Implemented multiphase flow solution strategy

A similar simulation strategy to that discussed in section 3.1.7 (b), was employed with the multiphase CFD hydrocyclone model. In contrast, convergence criteria were relaxed gradually from 0.001 to 0.005 and improved solution stability, at the point of air core inception, was achieved by altering the discretisation scheme for all the equations employing the third order accurate [18] QUICK scheme to the first order accurate upwind differencing scheme. A pulse of air core inception at the spigot, which is identical to that observed during the physical start-up process of a hydrocyclone [49], was successfully simulated. Following this pulse, the air core developed at the spigot subsided, leaving behind the artificially simulated portion prevailing within the core of the spigot. Solution stability, without any subsequent air core inception at the spigot, was mantained for a further 0.05s of simulated flow time, which was achieved over a two-week simulation period. Figures 3.15 (a) and (b), depict the air recirculation zones at the spigot discharge orifice, at instances after the point of maximum air core development and near disappearance, respectively. A significant reduction in the air recirculation zones as well as the pure air fraction content recirculated, are observed.

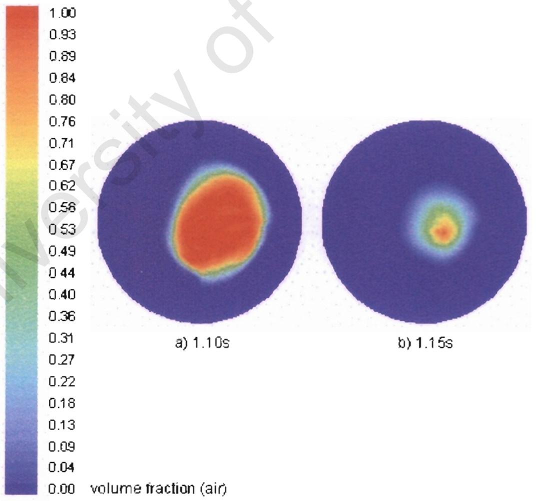

a) 1.10s b) 1.15s

Figure 3.15: Diminished spigot discharge orifice air recirculation zones

3.2.3 Summary

A discussion on the exploratory and implemented strategies that are relevant to the numerical simulation of both single phase and multiphase hydrocyclone flow fields has been presented. Certain specifics, which are concerned with geometry generation and meshing of the cyclone geometry, boundary condition specification and flow equation discretisation as well as turbulence and multiphase flow modelling, have also been highlighted. An assessment of the integrity of the predicted numeric results is made in the subsequent chapter.

Chapter 4

CFD Results and Discussion

The numerical flow field predictions due to the CFD hydrocyclone models that were highlighted in chapter 3, are presented and discussed in detail in the present chapter, with regard to the velocity and pressure field profiles. The unsuccessful simulation of the air core, although beyond the scope of this work, renders the selected [6] air core-operated hydrocyclone experimental data set unusable for the purpose of validating the water-only CFD hydrocyclone models developed in this work. Furthermore, the lack of published experimental data on water-only operated cyclones also presents no means to validate the CFD hydrocyclone models. The integrity of the CFD predictions is thus motivated via qualitative comparison with experimental air core-operated hydrocyclone velocity trends that are reported in the literature.

Unless otherwise stated, all results are discussed with respect to the flow field predictions due to the circular inlet hydrocyclone. Inlet geometry effects are assessed by contrasting the turbulence intensity levels of the flow field in the feed entry sections of circular and rectangular inlet hydrocyclones. Superimposed graphical plots of horizontal planar component velocity profile predictions due to these variable hydrocyclone geometric configurations, which can be used for future comparative studies, are presented in Appendix C. Comment is also given on the appropriateness in implementation of the standard wall function approach, with regard to the near-wall treatment of the hydrocyclone flow field. The insight gained from the multiphase flow simulations, which present a credible account of the possible mechanism for air core inception and development, is also discussed. All pressure profile plots depict pressures that are relative to an atmospheric pressure value of 101 kPa (101 325 Pa). The coordinate system adopted is consistent with that defined in chapter 3, section 3.1.1 (a). All vertical planar cross-sectional views of the hydrocyclone represent the x-y plane, in which the three-dimensional overflow discharge spiral is also depicted.

4.1 Predicted single phase flow fields

Experimental observation indicates that upon initiation of inlet flow into a void cyclone, circumferential flow is established against the peripheral internal wall structure [19]. The cyclone subsequently fills from the spigot upwards, facilitating the expulsion of the centrally entrained air core via the overflow discharge orifice, thus allowing for the pre-air core inception flow field to develop as a water-only flow [19]. The numerical flow field was initiated with a water-filled cyclone bearing the boundary conditions listed in table 3.1. As such, the initial phase of the start-up period of the actual physical process, which is of no practical significance, was not captured. While bearing in mind this inherent limitation of the CFD hydrocyclone models, predictions providing insight on its hydrodynamic behaviour from the completely-filled to the equilibrium single phase flow condition, were derived and these are discussed in the subsequent section.

4.1.1 Predicted hydrocyclone flow field development dynamics

The hydrodynamic development of the hydrocyclone flow field is discussed with respect to the velocity and pressure field predictions. The start-up and equilibrium flow conditions are considered, which, unless otherwise stated, correspond to a 1000-iteration and a two-second simulation period, of flow field resolution via the steady state and transient solvers, respectively. Unless otherwise stated, all horizontal planar flow field profile views depict plots on the plane that constitutes the horizontal inlet duct bisector, which is located at a depth of 12.5 mm below the roof of the hydrocyclone.

a) Velocity flow field development and exhibited spatial distribution trends

Upon initiation of the inlet flow, the inlet stream translates linearly into the main chamber, where it impinges upon the static stream, as depicted in figure 4.1 (a). On account of the negative pressure gradient established between the inlet and the discharge orifices, the inlet stream is accelerated to a local flow velocity higher than that specified at the inlet boundary. A radial velocity gradient is thus established within the confines of the vortex finder-main chamber annulus, within which slower moving fluid streams are observed in the vicinity of the walls. On account of the progressive decceleration of the dynamic inlet fluid stream, progressively less momentum is imparted onto the static fluid contained within the main chamber, hence the establishment of the stagnant fluid zone, in the vicinity of the vortex finder, as indicated by the blue-coloured regions in figures 4.1 and 4.2 (a). Fluid displacement, via mass diffusion, through the vortex finder and spigot constrictions, leads to its linear acceleration and atmospheric discharge, as depicted in figure 4.2 (a). Likewise, an asymmetric velocity distribution that comprises faster flowing periphery fluid streams and a stagnant central fluid zone, is exhibited in the vertical plane, as depicted in figure 4.2 (a). During this phase, which marks pre-establishment of swirl within the bulk of the fluid, short-circuit flow represents the only secondary flow pattern developed.

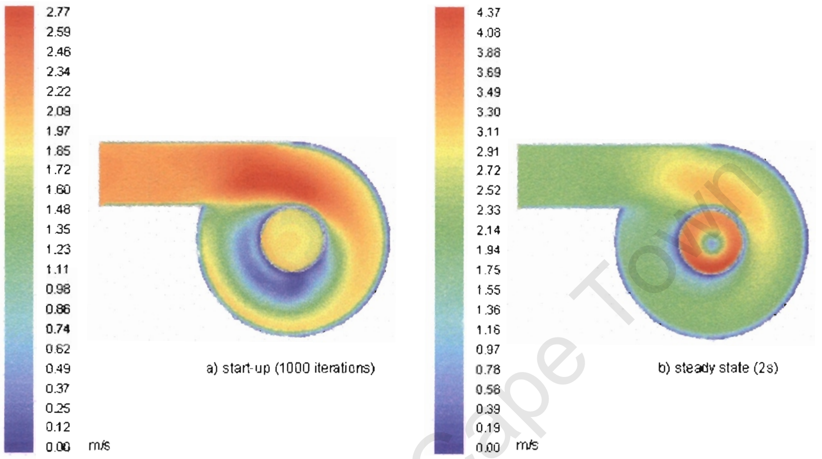

a) start-up (1000 iterations)

b) steady state (2s)

Figure 4.1: Horizontal planar start-up and steady state velocity profiles

With reference to figures 4.1 and 4.2 (b), which represent the equilibrium flow condition, the bulk of the flow field mantains a relatively constant velocity, as indicated by the dominant green-coloured regions. In contrast to the start-up conditions, the inlet fluid stream is, upon entry into the main chamber, briefly accelerated by the swirl motion before it assumes the bulk flow velocity. A relatively insignificant portion of the fluid remains stagnant within the vicinity of the exterior of the vortex finder. The no-flow condition exhibited on the internal wall structure is consistent with the no-slip condition specified at these boundaries, in close proximity to which, insignificant velocity gradients are observed. The establishment of the stagnant fluid zones that are located within the core of the vortex finder and the spigot, as depicted in figure 4.2 (b), may be attributed to the flow reversal effected across the discharge orifices on account of the sub-atmospheric pressure generated along the central axis of the hydrocyclone. The relatively marked buildup of this fluid within the vortex finder, in contrast to that contained within the spigot, is due to the additional downward-directed gravitational force exerted on the fluid, against which the fluid recirculating across the spigot discharge orifice has to act. Such fluid recirculation across the spigot discharge orifice is physically unrealistic and merely represents a mathematical feature of the CFD hydrocyclone models, which provides the means by which they treat flow across pressure outlet boundaries. An insignificant portion of a slow moving stream, which stretches along the length of the conical chamber, also exists at the core of the flow field.

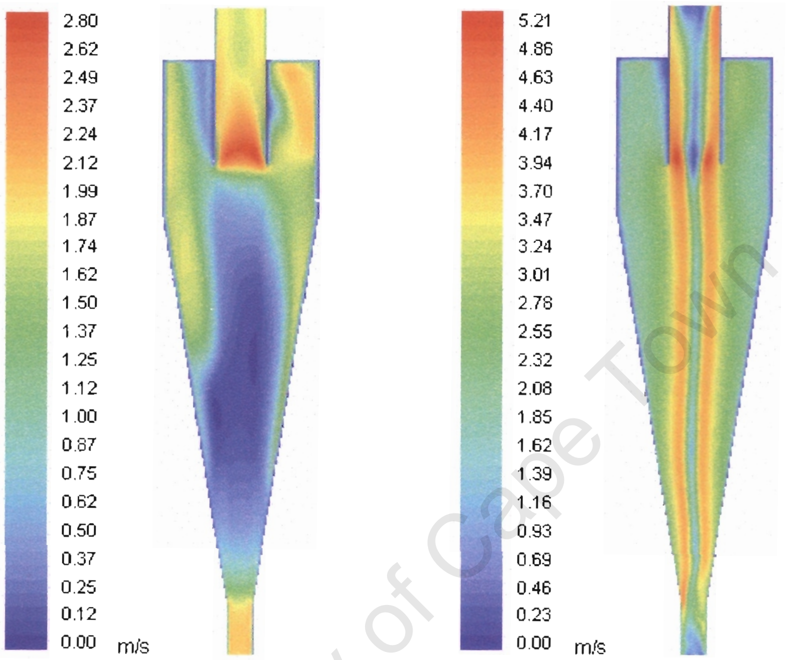

a) start-up (1000 iterations)

b) steady state (2s)

Figure 4.2: Vertical planar start-up and steady state velocity profiles

In the vicinity of the central axis of the hydrocyclone, lie the fastest asymmetric fluid flow streams, which extend from the apex of the conical chamber up to the vortex finder discharge orifice, as depicted in figure 4.2 (b). The circular horizontal cross-sectional view of the precessing fluid stream depicted in figure 4.1 (b), consists of a cylindrical annulus that encircles slower moving secondary streams. This implies that the outermost precessing fluid stream is the overflow stream which constitutes the innner spiral depicted in figure 2.3. Solid body rotation, which is synonymous with the forced vortex structure discussed in section 2.1.1 (c), is also implied. The graphical plot in figure 4.3 depicts spirals that comprise the overflow and underflow discharge streams, as well as pathlines of fluid particles released from the inlet.

b) Pressure field development and exhibited spatial distribution trends

The development of the flow pressure field is marked by the initial establishment of sub-atmospheric pressures within the spigot and vortex finder, as depicted in figure 4.4

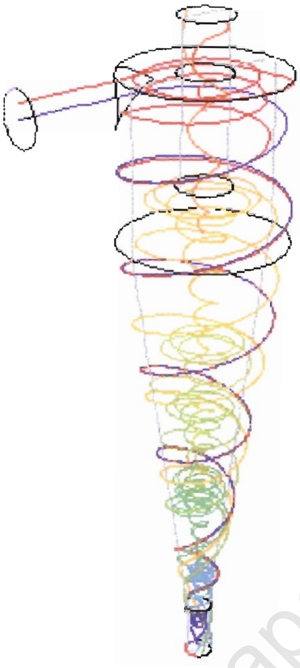

Figure 4.3: Overflow and underflow discharge stream particle pathlines

(a). During this phase, the remainder of the body of the hydrocyclone constitutes a positive pressure field, which exhibits a positive gradient, traversing radially outwards. Figure 4.4 (b) depicts the asymmetric flow field pressure distribution at the equilibrium condition. As indicated, and in accordance with experimentally inferred phenomenon, atmospheric exposure of the discharge orifices leads to the formation of a negative core pressure. High pressure gradients are predicted within the vicinity of the central axis. The radial extent of this region is, in the same respect as the inner spiral depicted in figure 4.2 (b), restricted to the diameters of the spigot and vortex finder.

4.1.2 Predicted single phase flow component velocity profiles

This section presents quantitative fluid component velocity data plots due to the single phase (water-only) flow field predictions arising from the circular inlet CFD hydrocyclone model. On account of the failure to successfully simulate an air core, and the lack of published water-only cyclone experimental data, no means are available for validation of the CFD hydrocyclone models. The credibility of the CFD predictions is thus accounted for by highlighting their similarity to literature-reported experimental velocity profiles, derived from air core-operated hydrocyclones. The origin of the local

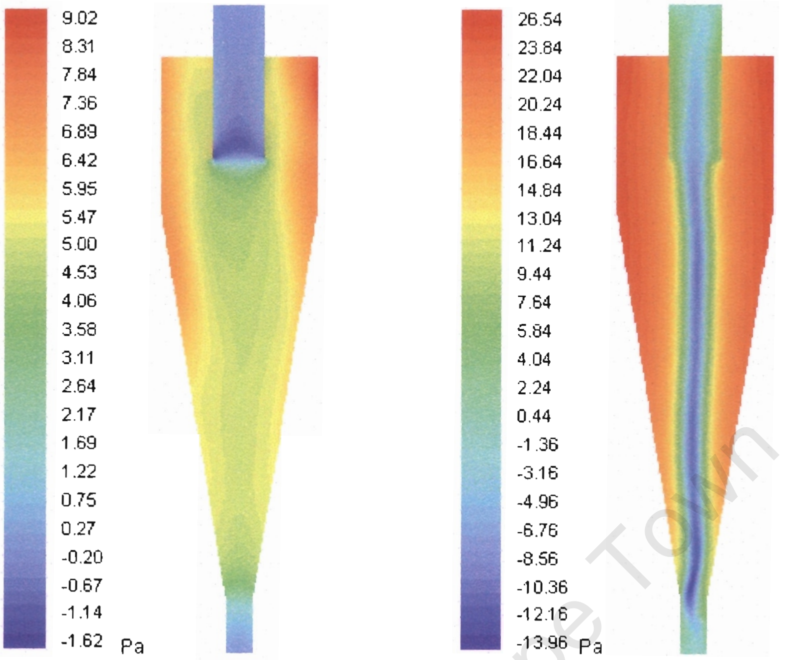

a) start-up (1000 iterations) b) steady state (2s)

Figure 4.4: Vertical planar start-up and steady state pressure profiles

coordinate system is located along the central axis, in the plane of the roof of the cyclone. Liquid component velocities are considered at horizontal planes located at vertical depths lying 30, 60, 120, 180 and 240 mm below the roof of the cyclone. The physical dimensions of the cyclone are indicated in figure A.1 and listed in table A.1. The spatial orientation of the geometry of the CFD hydrocyclone model is depicted in planar view in figure 4.9.

a) Axial velocity component

The spatial distribution of the liquid axial velocity component is depicted in figures 4.5 (a) - (e). At a 30mm depth, in the positive radial direction, the flow is directed upwards in the vicinity of the exterior of the vortex finder wall and downwards thereafter. This flow reversal pattern signifies the possible formation of Eddy flow currents. In contrast, no flow reversal is exhibited in the negative radial direction. The maximum negative velocity observed in close proximity to the exterior of the vortex finder wall is perhaps due to short-circuit flow. In the vicinity of the interior of the vortex finder wall and at the core, occur high and low liquid velocities, which are due to the high velocity overflow discharge spiral and the relatively stagnant centrally located fluid stream, respectively. This observation is consistent with the velocity profile depicted in figure

4.2 (b). Although this trend persists down to a 240mm depth, the differences in velocity between the two streams are only significant within the main chamber. The recirculation due to the the possible formation of Eddy flow currents is also observed at a 60mm depth, with recirculation spiral formation in both axial directions and in opposite senses of rotation. The axial flow reversal exhibited in both radial directions, within the conical chamber, is indicative of the formation of the vertically opposed overflow and underflow discharge streams.

The asymmetry in the predicted velocity profiles, across the entire cyclone length under consideration, is consistent with observations due to Hsieh [6]. The marked asymmetry in the axial velocity profiles within the main chamber, which arises on account of the asymmetric inlet [6], is also equally predicted. Likewise [6], the reduction in the extent of this asymmetry in the sub-vortex finder region, is also observed. The predicted velocity profiles demonstrate, in the same manner as reports due to Kelly [3], that the axial velocity component is an indication of the magnitude of the overflow and underflow discharge spirals, which determine the volumetric distribution of the two product streams. Traversing down the length of the cyclone, the horizontal axis intercept of this locus appears to migrate radially inwards in an equivalent fashion to observations due to Kelsall [16], as depicted in figure 2.6, and Leith [10]. In accordance with the literature [3], fluid motion within this abstract envelope of zero axial velocity is directed upwards, and downwards beyond its periphery. In general, an increase in the absolute axial velocity component was predicted with increase in radial distance from this envelope. The increase is greater in the upward than the downard direction of flow. This prediction is also consistent with experimental observation [6] [16], as depicted in figure 2.6.

b) Radial velocity component

The spatial distribution of the liquid radial velocity component is depicted in figures 4.6 (a) - (c). The common practice [6] [16] is to measure the axial and tangential velocity components, and to compute the radial component from continuity. On account of the difficulty involved with taking velocity measurements close to the wall [6], radial velocity data for the near-wall region is normally unavailable, as depicted in figure 2.7, which is due to Kelsall [16]. Suprisingly, only positive radial velocity component data was plotted [16] in figure 2.7, despite the availability of axial and tangential velocity data up to the air core position, as depicted in figures 2.6 and 2.8, respectively. Asymmetric and near-symmetric velocity profiles are predicted within the main chamber and conical chamber, respectively, as depicted in figures 4.6 (a) - (c). The single tangential inlet supposedly serves as the source of the radial velocity profile asymmetry

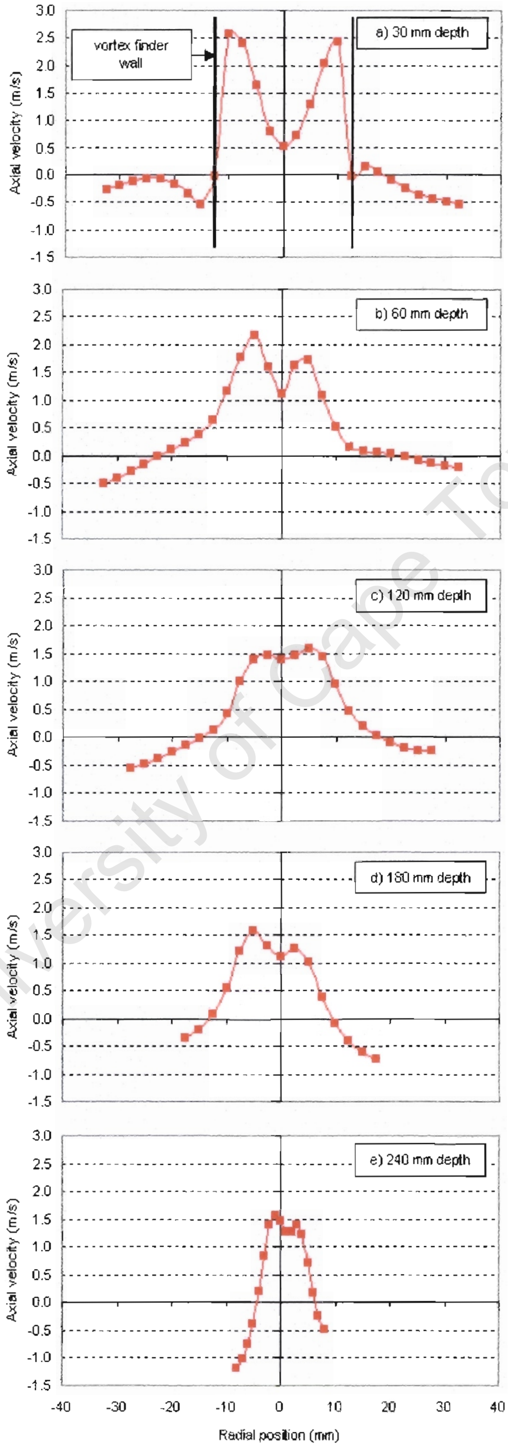

Figure 4.5: Horizontal planar axial velocity profiles (30-240 mm)

observed within the main chamber [31]. Of the three velocity components, the radial component, which is at about half the axial velocity values, represents the least in magnitude, in accordance with reports presented in the literature [3] [16].

Alternating positive and negative liquid radial velocity fields, which are reportedly [32] [33] of relevance to radial solid particle classification, are predicted within the conical chamber. These predictions are consistent with the CFD results reported by Cullivan et. al. [31], who have, on their basis, challenged the common understanding of radial particle classification. The particle equilibrium orbit theory forms the basis of this classical approach, which mantains that the radial velocity component is, with the exception of Eddy flow, always directed radially inwards, such as to cause radial transport of fine particles towards the hydrocyclone core. The centrifugal drift of large particles towards the cyclone wall, which effects radial particle classification, is thus achieved via a particle centrifugal-drag force balance [3] [32] [33]. Contrary to this classic understanding, the CFD predictions reveal that within a significant portion of the regions in the positive radial direction, the centrifugal and drag forces are in fact additive i.e. directed radially outwards, if approximate homogeneous motion of the fluid and solid particles is assumed. The establishment of insignificant radially inward-directed fluid velocity fields in the vicinity of the conical chamber wall, in the positive radial direction, may be attributed to bulk flow wall reflection effects. The oppositely-directed flow fields established on either side of the central axis of the hydrocyclone, within the main chamber regions lying external to and in the sub-vortex finder regions, is indicative of Eddy flow current formation. The relatively minute liquid radial velocity magnitudes, which do not exceed unity, seem to suggest that radial particle displacement and classification are predominantly due to the action of the centrifugal force and that inward radial particle migration is a mass displacement effect.

c) Tangential velocity component

The spatial distribution of the liquid tangential velocity component is depicted in figures 4.7 (a) - (c). In accordance with common practice, the graphical plots depict absolute values that are plotted as such in order to reflect a physically realistic Rankine vortex flow structure. The predicted tangential velocity component trends are consistent with those reported by Kelsall [16], as depicted in figure 2.8, and Hsieh [6]. At a 30mm depth, which lies above the tip of the vortex finder, a velocity increase is observed when traversing from the cyclone wall to the exterior of the vortex finder. In close proximity to the vortex finder, a maximum is reached before as sudden decrease is exhibited. A similar trend is observed in the sub-vortex finder and conical chamber

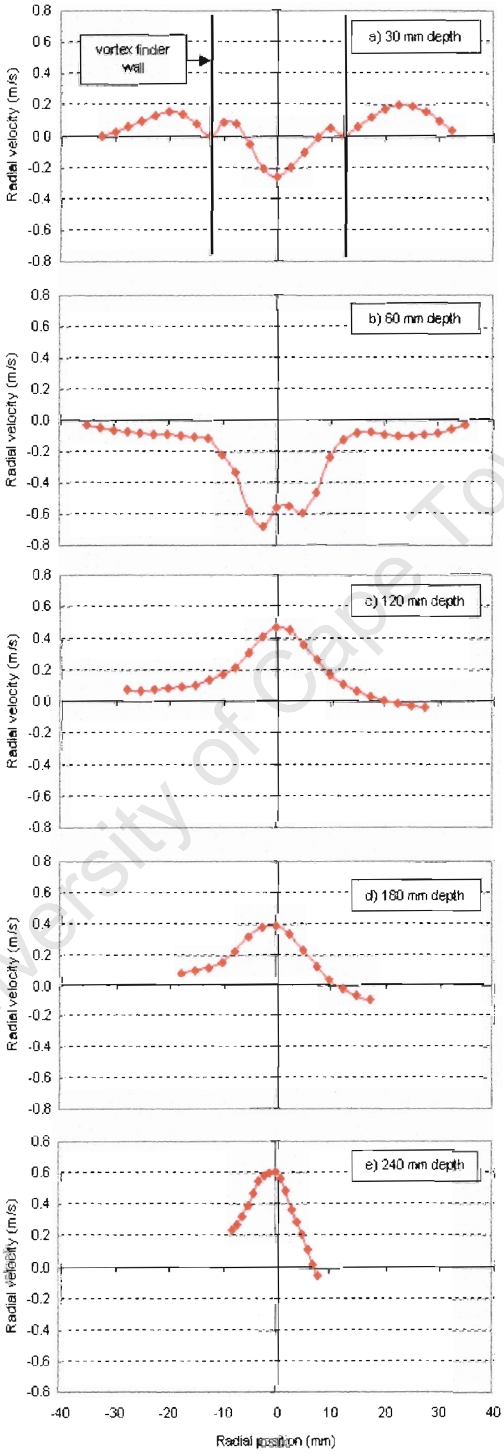

Figure 4.6: Horizontal planar radial velocity profiles (30-240 mm)

regions, where steeper velocity gradients occur traversing towards the central axis of the hydrocyclone. Insignificant asymmetry in the tangential velocity profiles is, in accordance with reports due to Hsieh [6], predicted.

The Rankine vortex structure depicted in figure 2.9, which constitutes free and forced vortices near the hydrocyclone wall and central axis, respectively, is accurately predicted numerically. The hypothetical condition of infinite tangential velocity at the hydrocyclone axis, which is implied by equation 2.1, is also closely approximated by the lines extending from the central axis. Solid body rotation due to forced vortex motion is also observed, even within the vortex finder. The reinforcement of the peak axial and tangential velocity components in the vicinity of the central axis, accounts for the high absolute liquid velocities observed in this region, particularly within the vortex finder. This observation is consistent with the equilibrium velocity flow profile depicted in figure 4.2 (b). Interestingly and contrary to common reports, the vortex motion is constrained by the vortex finder and main chamber wall structures, as depicted in figure 4.7 (a). The continuity in velocity across the vortex finder wall, which is depicted in figure 2.8, as reported by Kelsall [16] and other authors [3] [6], is in the opinion of the author, physically unrealistic, especially given the presence of short-circuit flow in the vicinity of the vortex finder internal and external wall structures. Such a continuity in velocity would, in the opinion of the author, be dissatisfied even with *hydraulically smooth* wall surfaces. The zero-velocity condition predicted on the vortex finder walls is due to the no-slip condition specified at all internal wall boundaries.

d) Qualitative component velocity predictions

This section presents the fluid component velocity profile predictions qualitatively. It is hoped that the outcomes presented in the previous section will become readily apparent through direct visual interpretation of figure 4.8. Figure 4.8 (a), which depicts the spatial variation of the axial velocity component, confirms the existence of the overflow and underflow spiral streams, which are oppositely directed. Although not very distinct, the indication is that axial flow reversal due to the overflow spiral, is initiated at the apex of the conical chamber. Additional mass diffusion, supposedly due to the axial flow reversal exhibited across the spigot discharge orifice on account of the sub-atmospheric axial pressure developed, appears to be effected within the spigot and to contribute to axial flow in the positive axial direction. Although figure 4.8 (a) depicts no Eddy flow currents, the existence of short-circuit flow is confirmed by the establishment of the radially-inward directed flow fields depicted at the tip of the vortex finder in figure 4.8 (b). The lack of fluid acceleration within the spigot, despite the constriction in flow area, is indicative of solid body rotation at the core

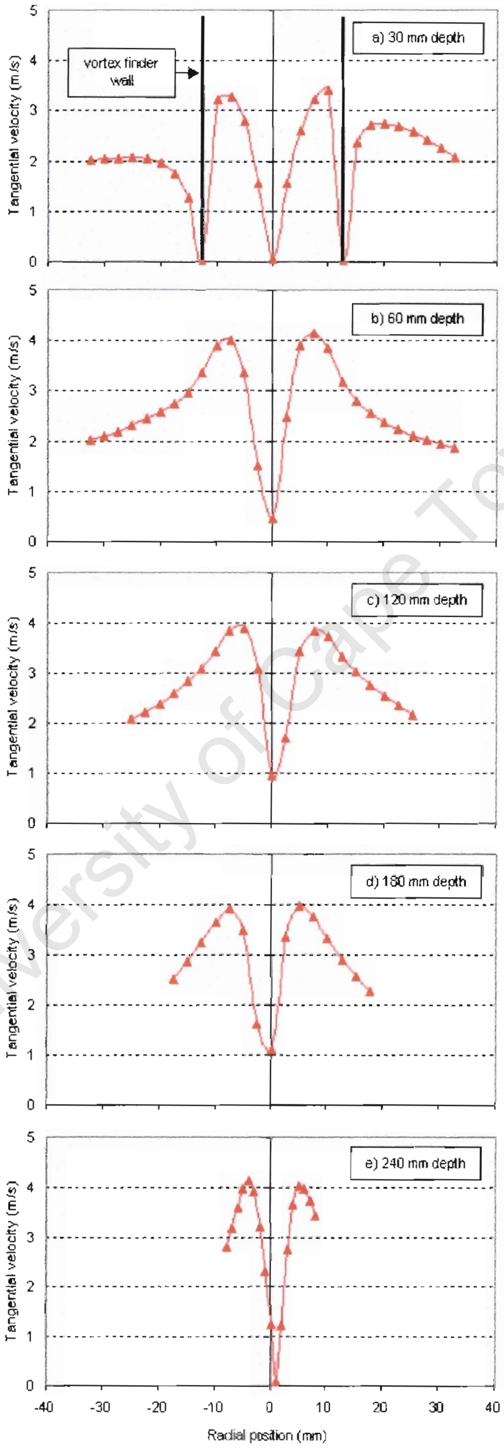

Figure 4.7: Horizontal planar tangential velocity profiles (30-240 mm)

of the flow structure. The credibility of this hypothesis is, in fact, supported by the presence of a fluid stream of near-constant angular velocity, at the core of the hydrocyclone, as depicted in figure 4.8 (c). The fastest downward-flowing streams, which are representative of the fluid stream which flows along the conical chamber wall, without being influenced by the flow structure established within the main flow, are observed in the immediate vicinity of the spigot wall.

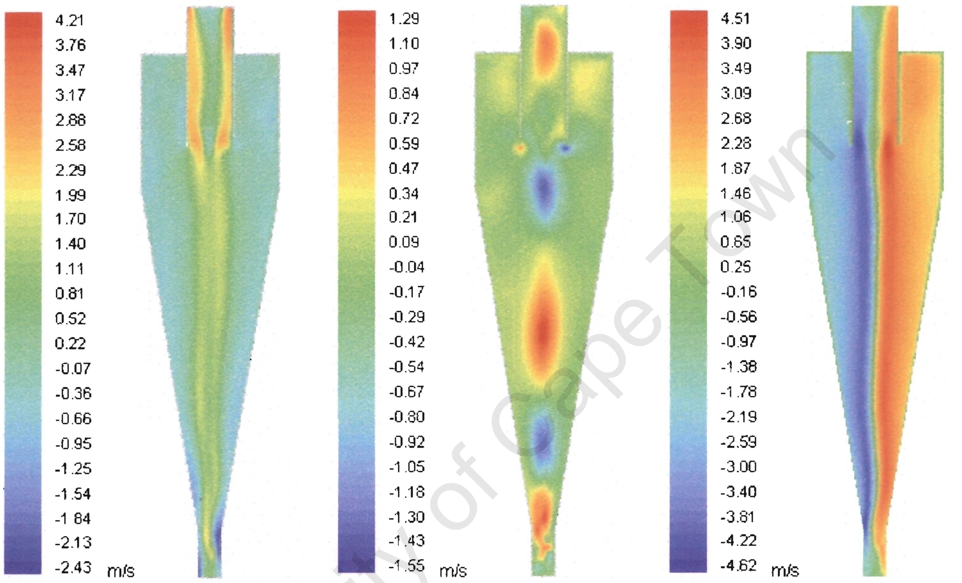

a) axial velocity b) radial velocity c) tangential velocity

Figure 4.8: Qualitative vertical planar fluid component velocity profiles

The alternating positive and negative radial velocity fields highlighted in section 4.1.2 (b) and equally depicted in figure 4.8 (b), are consistent with reports due to Cullivan et. al. [31]. Nonetheless, the indication is that the argument presented in section 4.1.2 (d), which challenges the classical understanding of the radial particle classification mechanism, stands to be rendered null and void if an air core is established along the central axis, such as to eliminate the red and blue-coloured regions of alternating positive and negative radial velocity. However, despite projections of the possibility of such air core-influenced flow field changes, it is highly unlikely that any such changes would significantly alter the state of the water-only equilibrium flow condition. The depiction of positive and negative tangential velocity profiles on either side of the central vertical axis of the hydrocyclone cross-sectional view depicted in figure 4.8 (c), gives evidence of the establishment of swirl motion in the flow structure. Confirmation of the presence of the Rankine vortex is given by the extension of the vortex motion across the entire length of the hydrocyclone, with near-constant tangential velocities of the central fluid stream, indicating solid body rotation due to forced vortex motion.

The velocity profile predictions are largely consistent with experimentally determined trends. They also serve to confirm physically observed phenomena such as short-circuit and Eddy flow currents. The CFD predictions have, however, provided a level of detail perhaps not observed or readily apparent experimentally. In addition, some of the common fundamental hypothetical concepts, which have been formulated to account for the dynamics of the internal flow field of the hydrocyclone, such as the equilibrium orbit theory, which forms the basis of the classical account of the mechanism of radial particle classification, have been challenged. The subsequent section discusses the variations exhibited in the flow fields arising from the circular and rectangular inlet CFD hydrocyclone models.

4.1.3 Comparison of single phase flow fields due to variable cyclone geometric configurations

The difficulty involved with classifying a hydrocyclone flow field as laminar or turbulent on the basis of the flow Reynolds number was discussed in chapter 2, section 2.1.2. It was further established that a turbulent flow field is likely to be developed within the inlet duct and that laminar settling may occur within the body of the hydrocyclone. In accordance with reports due to Kelsall [55], excessive turbulence prevails within the feed entry section of a hydrocyclone, where the inlet stream comes into contact with the swirling flow field contained within the main chamber. The turbulence mixing subsequently effected is reportedly due to the resultant shock effects. The turbulent kinetic energy per unit mass, k, which is a measure of the energy generated via the fluctuating turbulent velocity components of a flow field, is used to quantify and contrast the turbulence intensity levels in the feed entry sections of the circular and rectangular inlet CFD hydrocyclone models. Turbulent flow characterisation and the CFD modelling thereof, is discussed in detail in Appendix B, section B.1.1. With respect to figure 4.9, k was determined in quadrants 1 and 2, at a depth of 12.5 mm below the roof of the hydrocyclone and at a radial position midway between the vortex finder and main chamber walls. Equispaced data acquisition positions spanning an angular displacement of 180^0 were used, with the negative x-coordinate direction representing the datum. An equilibrium flow condition corresponding to a one-second simulation period is considered.

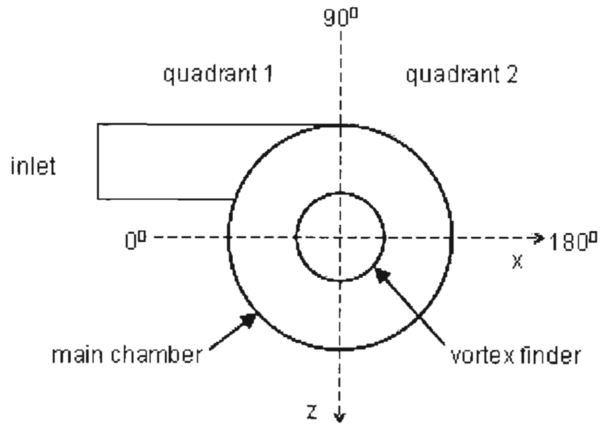

Figure 4.9: CFD hydrocyclone model coordinate system descriptor

The variation of k with angular displacement is depicted in figure 4.10. The rapid increase in k, with increase in angular displacement, up to a maximum at 90^0, for the circular inlet hydrocyclone configuration, serves to confirm the establishment of a feed entry section flow field of higher turbulence intensity. Subsequently, the incoming fluid stream is progressively deccelerated hence a progressive reduction in the momentum imparted onto the bulk flow, which, in turn, effects a decrease in k. Finally, the flow field assumes a near-constant angular velocity due to the swirl motion of the bulk flow hence turbulence is minimal and k approximately constant.

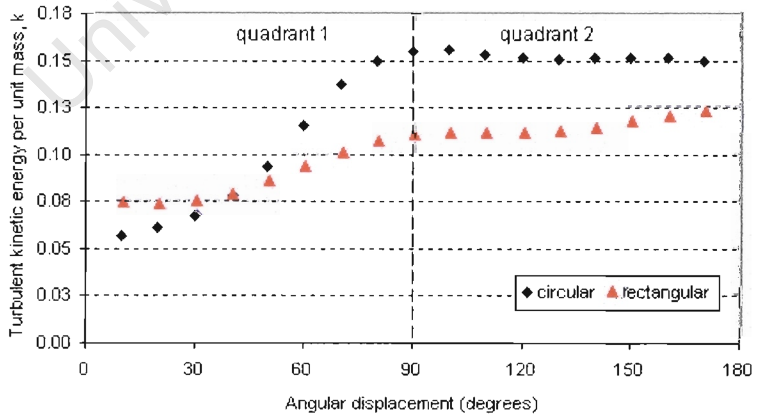

Figure 4.10: Variation of turbulent kinetic energy per unit mass in hydrocyclone feed entry section

The flow field arising from the rectangular inlet hydrocyclone mantains an average

k-value of approximately 0.1. Its relatively less steeper k-gradients indicate the establishment of near-equilibrium inlet-swirl flow conditions. Such steady flow conditions favour the operation of a hydrocyclone, since feed behaviour instability hampers its performance [3]. The different inlet duct-main chamber interface geometries account for the variation in the shock effects exhibited within the feed entry sections of the variable cyclone geometric configurations. The capability by CFD to faciliate investigation and quantification of hydrocyclone geometry effects demonstrates its potential for use as a hydrocyclone design tool.

4.1.4 Assessment of the appropriateness in application of the wall function approach

The validity in application of the standard wall function approach is examined and discussed with respect to the relatively critical grid configuration implemented with the circular inlet hydrocyclone, the details of which are discussed in chapter 3, section 3.1.1 (b). A preliminary assessment of the validity of the adoption of this approach was conducted in the same chapter, in section 3.2.1 (a), with respect to the y^* criteria. Further assessment is conducted in this section by comparing the single phase flow field predictions with water-only experimental and CFD data due to Slack [7]. Although insufficient detail is given [7] on the experimental operating, and implemented CFD model boundary conditions, the comparison is undertaken to indicate the consistency of the CFD predictions with both experimental and CFD data as well as to assess the integrity of the numerical results in the treatment of the near-wall flow field, in the context of the implementation of the standard wall function approach. The Monredon [16] type 1 cyclone geometry, which was used for setting up the CFD models in this work, was also investigated by Slack [7]. In accordance with the CFD predictions, the near-wall gradients exhibited by the tangential velocity component profiles were steepest, hence the most critical. As such, tangential velocity profiles at 50 and 120mm depths, below the roof of the cyclone, are compared, as depicted in figure 4.11.

The CFD predictions compare well in both cases, in the vicinity of the central axis. The discrepancies observed in the radial positions and numerical values of the peak velocities may, in combination with the off-set predicted beyond the maxima, be attributed to the possible implementation of different boundary conditions. The indication is that the operating inlet velocity prescribed by Slack [7] was higher in magnitude. Accordingly, the numerical results also under-predict the experimental data, in both cases, but the discrepancies are marginal in the vicinity of the near-wall region. However, on account of the implementation of standard wall functions in the near-wall region of the CFD hydrocyclone model, under-predictions of both

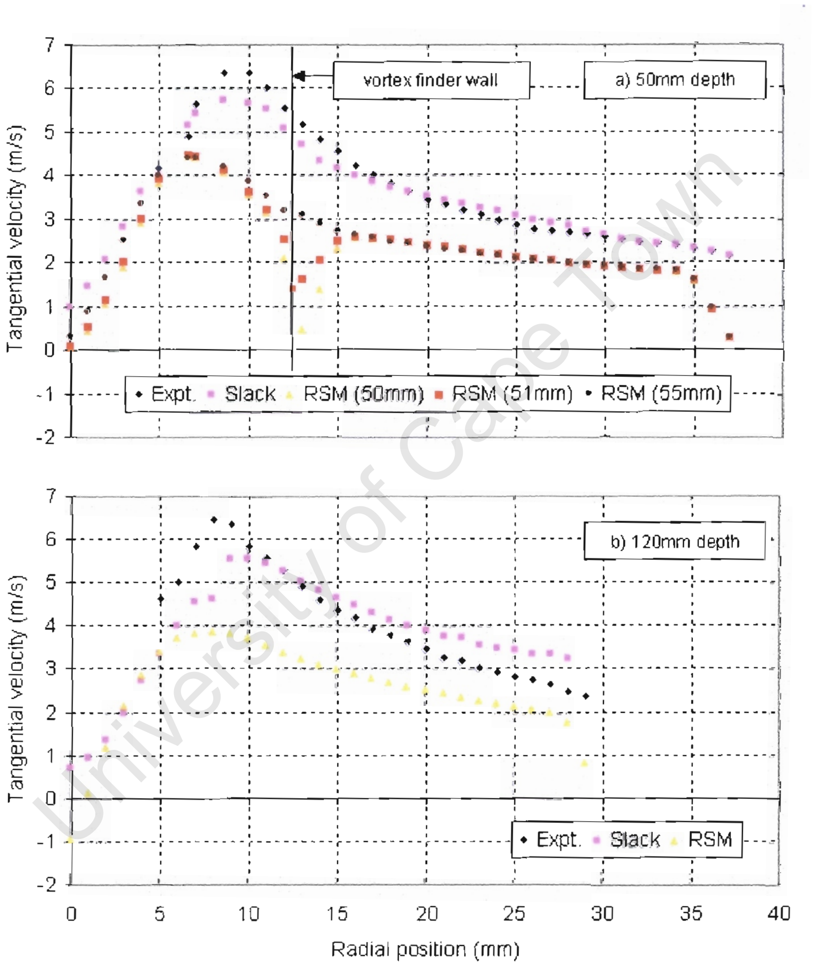

Figure 4.11: Comparison of experimental and CFD tangential velocity predictions

the CFD [7] and experimental data are here observed, at both horizontal levels under consideration. Steep local velocity gradients are also predicted. This grid-related inadequancy can be improved upon by modifying the grid configuration in the near-wall region such as to better satisfy the y^* criteria so that improved local velocity predictions may be obtained.

The CFD predictions [7] are fairly consistent with the experimental data, particularly at a 50mm depth. The accurate prediction of the flow field in the near-wall region, at a 50mm depth, is possibly due to the appropriate implementation of wall functions, but more likely the adoption of the more conservative boundary layer meshing approach. The numerical [7]-experimental data discrepancy exhibited at a 120mm depth, is possibly due to turbulence model-compounded flow resolution inadequancies. The author challenges the indication of a continuity in velocity at the tip of the vortex finder, in the results presented [7] in figure 4.11 (a). A comprehensive discussion, which forms the basis of this argument, was presented in section 4.1.2 (c). With reference to figure 4.11 (a), and in accordance with the presented argument, the CFD predictions due to the author confirm that such a discontinuity in velocity is exhibited at the tip of the vortex finder, which is located at a 50mm depth. The indication is that a decline in velocity occurs in close proximity to either side of the wall, even at a depth of 1mm below the tip of the vortex finder. As can be expected, a non-zero minimum velocity is however exhibited at the radial location corresponding to the radial extent of the vortex finder. Continuous velocity profiles, which are similar to that plotted at a 55mm depth, as depicted in figure 4.11 (a), are in fact obtained only with some appreciable vertical clearance from the tip of the vortex finder. Despite the highlighted grid-specific inadequancies, the CFD predictions indicate the potential for the joint implementation of standard wall functions and the RSM, such as to obtain physically realistic hydrocyclone flow field solutions, particularly in the near-wall region. The integrity of such wall function velocity predictions can, however, only be verified via comparison with experimental data. The subsequent section discusses the multiphase flow predictions arising from the CFD hydrocyclone models.

4.2 Predicted multiphase flow fields

The multiphase (water/air) flow field predictions are discussed with respect to the velocity and pressure field profiles. Comparisons are drawn between the single phase (water-only) and multiphase flow field predictions in order to provide a better understanding of the hydrodynamic behaviour of the hydrocyclone flow field. An account is also given of the probable mechanism for air core inception and development.

4.2.1 Multiphase flow field velocity profile predictions

Upon introduction of the secondary phase, the velocity field remains largely unchanged. High liquid velocities, which are indicative of the faster flowing overflow discharge spiral that is constrained by the spigot and vortex finder, are, in a similar manner to the single phase flow field predictions, observed in the vicinity of the central axis. However, a comparison of figures 4.2 (b) and 4.12 (a), indicates improved radial velocity resolution. With reference to figures 4.12 (a) and (b), the near-stagnant fluid zones contained within the spigot and the vortex finder, are displaced by the incoming atmospheric air streams. The air core induced at the spigot appears to be bounded, in part, by the overflow discharge spiral depicted in figure 4.12 (a). The indication from figure 4.12 (b) is that the underflow stream flows against the spigot wall boundary before discharging into the the atmosphere as a fine spray, as a result of the significant reduction in the spigot discharge orifice cross-sectional area available for its discharge.

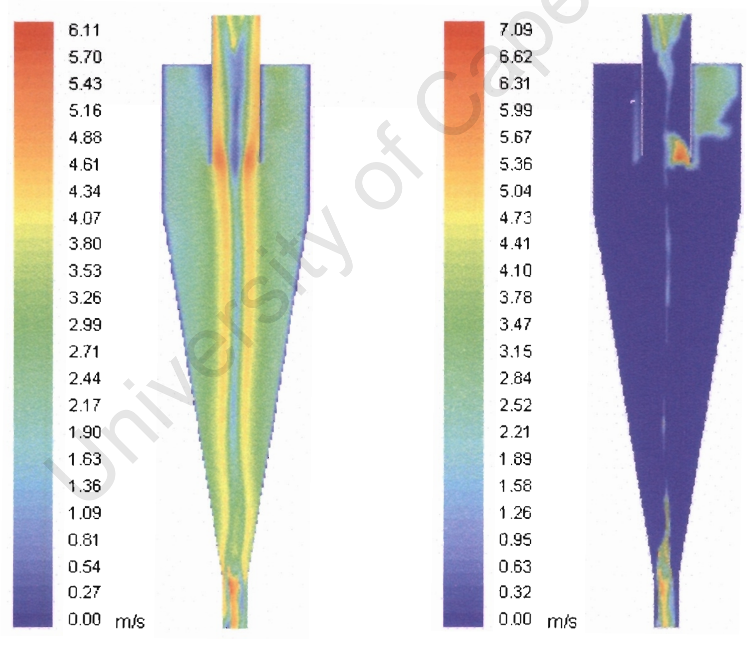

a) multiphase – (water/air)

b) single phase – (air)

Figure 4.12: Vertical planar mixture and air velocity profile comparison

Evidence of short-circuit flow is indicated in figure 4.12 (b), by the air introduced as part of the inlet feed stream. The short-circuiting stream is, however, driven to the low pressure core on account of the differential densities between the operating media. This phenomenon further supports the idea of the potential for successful implementation of the strategy to introduce air as part of the feed stream and to enforce its sole recirculation across the discharge orifices, such as to artificially develop an air core from both discharge orifices. With reference to figure 4.12 (b), a thin air stream, supposedly transported by the centrally-located slow-moving water stream depicted in figure 4.12 (a), also establishes a connection between the air core contained within the spigot and that artificially induced at the vortex finder. The indication from figures 4.12 (a) and (b), is that the local velocities of the air streams are higher than those exhibited by the mixture, suggesting relative motion between the constituent phases. As such, and in accordance with reports due to Brennan [37], the indication is that implementation of the variant of the ASMM which employs the slip velocity formulation is better suited to resolving multiphase hydrocyclone flows because it allows for drift between the constituent phases, such as to facilitate and enhance the establishment of distinct air and water regions. The homogeneous implementation of the ASMM was, as discussed in chapter 4, section 3.1.7 (b), adopted in order to achieve economy with simulation run times. Upon establishment of a fully developed air core, it was intended to switch to the variant of the ASMM incorporating the slip velocity formulation, such as to obtain improved resolution of the water-air interface. The subsequent section discusses the spatial distribution of the multiphase flow pressure field.

4.2.2 Multiphase flow field pressure profile predictions

Contrary to the velocity field, the pressure field is strongly influenced by the introduction of the secondary phase. The changes exhibited in the pressure field are in magnitude rather than spatial distribution. With reference to figures 4.13 (a) and (b), which depict the equilibrium single phase flow and the near-maximum air core development pressure profile conditions, the indication is that a significant rise in internal pressure occurs with the multiphase flow field. Inasmuch as the primary liquid phase is incompressible, upon inception of the air core, the coexistence of distinct and homogeneous liquid and gaseous phase regions, forces the liquid phase to occupy a reduced volume, for the same volume flow rate, hence the increase in internal pressure. In addition, given the atmospheric exposure of the discharge orifices, the generation of a sub-atmospheric core pressure is indicative of the atmospheric pressure field pushing the liquid phase against the internal wall structure, such as to effect an increase in internal pressure. Absolute pressure increments of 23.5 and 12.3 kPa are observed in the values of the maximum and minimum pressures, respectively. With reference to figure 4.13 (b), the local absolute pressure values range from 89 to 125 kPa, which is consistent with typical [3] operating conditions. However, on account of the inherent physical fluctuating behaviour and instability of the air core, a fluctuating pressure field is equivalently effected. Despite the partial development of an air core, a 23.8 kPa pressure drop, which is about half that developed [6] with an air core established across the entire length of the cyclone, was predicted across the inlet and vortex finder discharge orifice. An improvement in the accuracy of the predicted pressure drop would be expected with further development of the air column. The values of the predicted absolute pressures are however partially influenced by the presence of the 50% by volume air stream introduced at the inlet, which is excessive and physically unrealistic. The simulation times indicated in figure 4.13 represent cumulative values.

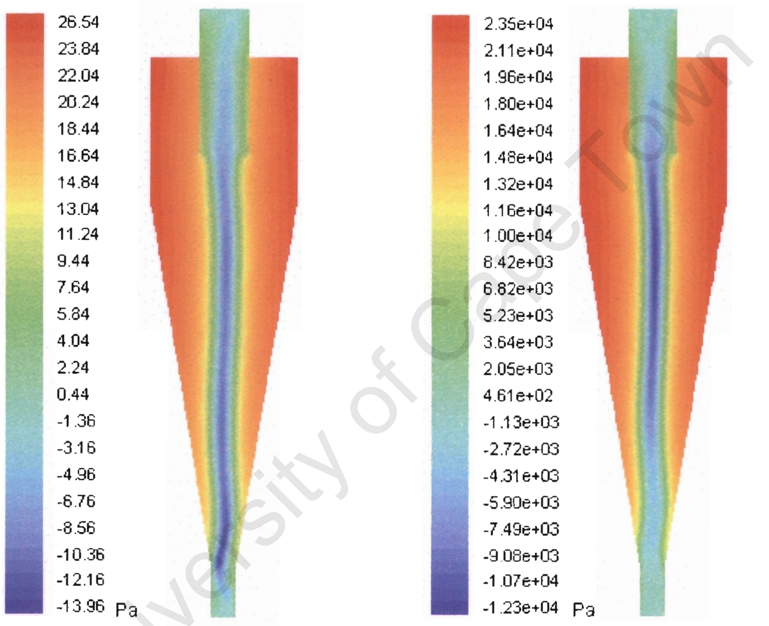

a) single phase – (water) (2s) b) multiphase – (water/air) (3.06s)

Figure 4.13: Vertical planar water and mixture pressure profile comparison

The Rankine vortex-induced sub-atmospheric core pressure depicted in figure 4.13 (a) is partially depleted in the spigot and vortex finder regions of figure 4.13 (b), on account of the inception of atmospheric air as depicted in figure 4.12 (b). The possibility of the velocity and pressure field profiles being probable mechanisms for the inception and development of the air core is discussed in the subsequent section.

4.2.3 The predicted air core inception and development mechanism

The validity of the report due to Cullivan et. al. [49], which concludes, on the basis of CFD predictions, that the axial hydrocyclone pressure is predominantly above atmospheric, prior to the development of the air core, cannot be refuted, on account of the differences in the inlet boundary conditions specified as well as the simulation strategies employed in their work and in the current research. Cullivan et. al. [49] modelled the hydrocyclone flow field, initiated with zero inlet flow and atmospheric pressure outlet boundary conditions, transiently. Although the pre-air core inception flow field in the present research was also developed as a water-only flow, the investigations, in accordance with reports due to Brennan [50], proved it necessary to attain a negative core pressure, prior to the introduction of the secondary phase, else diverged solutions were obtained.

Inasmuch as the hydrodynamics of different-sized hydrocyclones reportedly [3] [17] [45] vary, any such differences in the predicted flow fields of the 50.8mm and the 75mm diameter cyclones investigated by Cullivan et. al. [49] and in this work, respectively, should, in the opinion of the author, be insignificant. The sub-atmospheric core pressure developed with the CFD hydrocyclone models investigated in this work can thus only be accounted for via the 62% discrepancy in the inlet volume flow rates employed. The higher inlet velocity of the CFD hydrocyclone models due to the author would ensure a higher peak tangential velocity, hence greater flow swirl and steeper radial velocity gradients that would in turn facilitate the development of a lower core pressure, particularly with exposure of the discharge orifices to the atmosphere. It may therefore not be conclusively deduced as to whether or not a negative core pressure is essential for air core inception, except to say that it proved necessary in order to obtain converged solutions, for the specific cyclone geometry and operating conditions investigated. Nonetheless, in accordance with intuitive and common understanding, it may be inferred that a sub-atmospheric core pressure is essential in order for suction of air to be effected across the spigot discharge orifice.

Spigot inception of a partially developed air core, which is largely identical to that depicted in figure 4.14 (a), is reported by Cullivan et. al. [49]. Contrary to the pressure profile depicted in figure 4.14 (c), their CFD predictions revealed a sub-atmospheric pressure in the region immediately adjacent to the spigot discharge orifice and a significantly positive pressure field within the remainder of the hydrocyclone internal flow field structure. Such a spatial pressure field distribution is largely consistent with that depicted in figure 4.4 (a) and would support the inception of an air core at the spigot, while equally suppressing the subsequent development thereof. On the basis of this observation, Cullivan et. al. [49] are further opposed to the common conception which holds that air core development is pressure-driven and mantain therefore that it must be transport-driven.

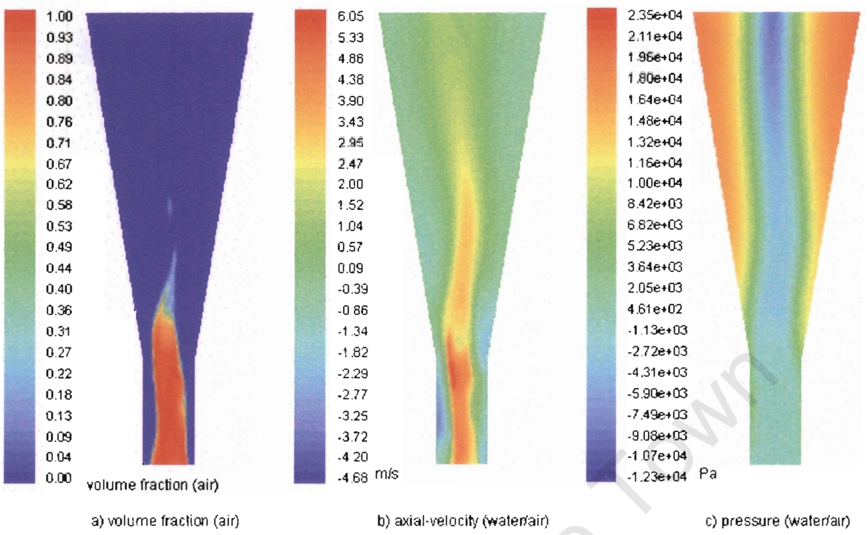

a) volume fraction (air) b) axial-velocity (water/air) c) pressure (water/air)

Figure 4.14: Probable convective transport-pressure field air core development mechanism

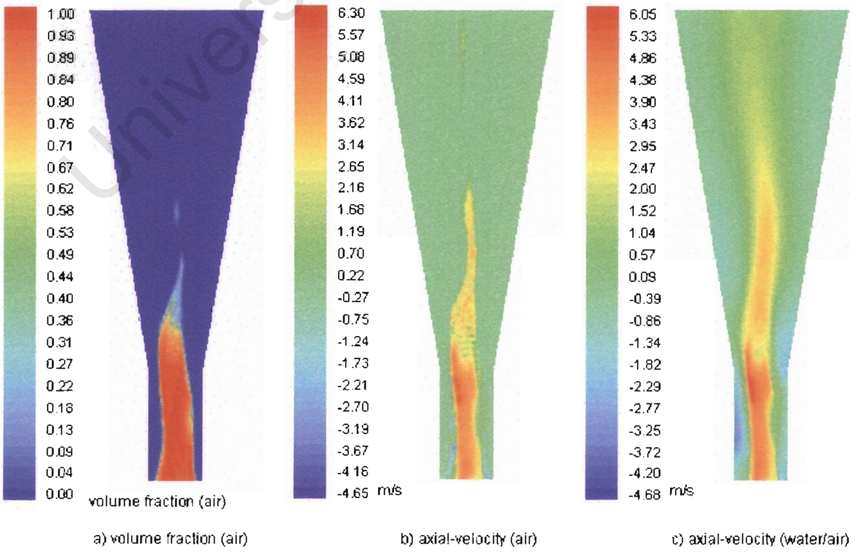

a) volume fraction (air) b) axial-velocity (air) c) axial-velocity (water/air)

Figure 4.15: Probable convective transport air core development mechanism

It was pointed out in section 4.2.1, with reference to figure 4.12 (b), that the thin centrally-located air stream is supposedly transported by the slow-moving central liquid-water stream depicted in figure 4.12 (a). Although, perhaps not pressure-driven, the central location of the secondary phase is, on account of the density differences exhibited between the operating media, supported by the sub-atmospheric core pressure, which prohibits the diffusion thereof, into the bulk flow. The indication from figure 4.14 (b), which depicts the axial multiphase flow velocity field, is that a positive axial velocity field which is unopposed to axial air core development is established. Although partially negative in the vicinity of the spigot internal wall boundary and the conical chamber apex, such downward-directed flow only serves to compound the underflow discharge stream. However, it is evident from a comparison of figures 4.15 (b) and (c), that such axial air core development is, in part, transported-aided. In addition, although partially depreciated, the sub-atmospheric core pressure, which supports air core inception, the axial location and the development thereof, is mantained as depicted in figure 4.14 (c).

4.2.4 Summary

A discussion of the numerical results arising from the CFD hydrocyclone models has been presented in line with the objectives of this dissertation. As such, the predicted velocity and pressure field profiles have been discussed, with focus centering primarily on single phase (water-only) flow fields. The appropriateness in application of standard wall functions, with regard to modelling of the near-wall region of the hydrocyclone flow field, has also been assessed. Flow fields arising from only two variable cyclone inlet geometries were considered. As such, further investigation is required in order to identify, by quantifying with certainty, the influence that a specific inlet geometry has on the internal hydrocyclone flow structure. The results derived from the multiphase (water/air) flow investigations, which were primarily aimed at establishing the procedural methodology for development and optimisation of the air core, have provided insight into the hydrodynamic behaviour of a hydrocyclone flow field, which challenges common conceptions. Convective transport and the internal hydrocyclone pressure field have been identified as being instrumental in the inception and development of the air core. The indication is that a sub-atmospheric core pressure supports air core inception and the central location thereof, while the subsequent development of the air column is a dual function of pressure-driven gaseous diffusion and convective transport. A summary of the extent to which the objectives of this research project have been met is given in the subsequent chapter. In addition, conclusions, which are based on the associated findings, are drawn.

Chapter 5

Summary and Conclusions

In view of the fact that the secondary objective of this research project was to provide an understanding of how to set up a two-product multiphase (water/air) CFD hydrocyclone model, moderate success has been achieved. Unfortunately, on account of the unavailability of published experimental data for water-only operated hydrocyclones, the predicted single phase (water-only) flow outcomes have not been validated. Furthermore, the experimental data set [6] that had been selected for the purpose of validating the CFD hydrocyclone models could not be used due to the failure to achieve formation of an air core. The significant influence that the air core has on the hydrocyclone flow field and the associated classification mechanism is acknowledged. Consequently, the need to develop a CFD hydrocyclone model with a fully developed air core such as to enable hydrodynamically meaningful hydrocyclone flow field predictions to be derived, is appreciated. However, despite literature reports of successful accounts of CFD hydrocyclone flow modelling, insufficient detail on the procedural methodology adopted in setting up the CFD hydrocyclone models is given yet the difficulty involved is emphasised. Consequently, this work aimed to establish a single phase (water-only) CFD hydrocyclone model and to explore and develop a robust methodology for setting up a multiphase (water/air) model. In the long term, it is envisioned to develop a CFD hydrocyclone model incorporating solids, hence the need to acquire the relevant knowledge and expertise incrementally by establishing rigorous methodologies.

Notably, however, solution methodologies and results, which are concerned with the fundamental aspects of this subject and that which will provide a relevant knowledge base for future related work, have been derived. A generic methodology for meshing the main body of the cyclone as well as means to avert non-conformal meshing of complex inlet duct-main chamber geometric configurations, have been identified. Also noted, are the turbulence and auxiliary models suited to the CFD modelling of single phase and multiphase hydrocyclone flow fields, via specific discretisation schemes. Numerical predictions have also been obtained, which reflect physically realistic hydrocyclone velocity and pressure field profiles. A procedural methodology for development of the air core, although implemented with partial success, has been established and numerical predictions from which insight into the probable mechanism for inception and development of the air core may be drawn, have been obtained.

Based on the findings of this research project, the following conclusions were drawn:

1. **The predicted spatial distribution of the liquid velocity components is consistent with experimentally-determined trends**
   The CFD predictions of the liquid velocity components were consistent with the experimentally-determined trends that are reported in the literature. Evidence of the existence of the locus or envelope of zero axial velocity, within which fluid motion is directed upwards, and downwards beyond its periphery, was given by the establishment of positive and negative axial flow fields. This also served as confirmation of the dual formation of the vertically opposed overflow and underflow discharge streams. In general, an increase in the absolute axial velocity component was predicted with increase in radial distance from the envelope of zero axial velocity, with the increase being greater in the upward than the downward direction of flow. The horizontal axis intercept of the locus of zero axial velocity migrated radially inwards, traversing down the length of the cyclone. The asymmetry exhibited in the axial velocity profiles was relatively pronounced within the main chamber on account of the asymmetric inlet flow.

   Of the three velocity components, the radial component represented the least in magnitude, and the axial and tangential global component values were twice and four times as large, respectively. Contrary to the common understanding which mantains that the radial velocity component is always directed radially inwards, the CFD predictions revealed the existence of alternating positive and negative liquid radial velocity fields. The implications of this observation are highlighted in a subsequent discussion which challenges the classical account of radial particle classification. Within the vortex finder-main chamber annulus, the tangential velocity component indicated an increase, traversing from the vicinity of the cyclone wall to the exterior of the vortex finder, at which in close proximity, a maximum was reached before a sudden decrease was exhibited. A similar trend was observed in the sub-vortex finder and conical chamber regions, where relatively steeper velocity gradients occured, traversing radially inwards.

2. **The Reynolds Stress Model (RSM) predicted a physically realistic Rankine vortex flow structure**
   The RSM, which reportedly represents the minimum order of accuracy for modelling hydrocyclone flow turbulence, predicted a physically realistic Rankine vortex flow structure. The establishment of solidy body rotation at the core of the flow field served to confirm forced vortex motion. The steep tangential velocity gradients exhibited beyond the radial positions of the tangential velocity maxima were indicative of the formation of free vortex motion. Such a compound vortex structure, comprising free and forced vortices, is characteristic of hydrocyclone flow.

3. **Physically realistic predictions of the characteristic hydrocyclone primary and secondary flow patterns were obtained**
   The establishment of positive and negative axial flow fields gave evidence of the formation of the vertically opposed overflow and underflow discharge streams, which constitute the primary spiral flow patterns of a hydrocyclone that determine the flow split to the discharge orifices. The dual exhibition of radial and vertical flow fields within the main chamber, particularly within the vortex finder-main chamber annulus, was indicative of the establishment of the secondary short-circuit and Eddy flow patterns.

4. **Pressure profile predictions that are consistent with intuitively inferred trends resulted**
   In accordance with experimentally inferred phenomena, atmospheric exposure of the discharge orifices led to the formation of a negative core pressure. High pressure gradients were predicted within the vicinity of the central axis and a positive pressure gradient was established radially outwards, for the equilibrium flow condition. The radial extent of the negative core pressure region was, in the same respect as the overflow discharge spiral, restricted to the diameters of the spigot and the vortex finder. The significance of this observation is that the negative core pressure is induced by the forced vortex motion exhibited within the core of the hydrocyclone flow field. The induction of the negative core pressure resulted in the inception of an air core at the spigot discharge orifice. This, in turn, effected an increase in the absolute values of the internal pressure field, on account of the atmospheric pressure field causing radial displacement of the liquid phase, towards the internal hydrocyclone wall structure. A fluctuation in the internal pressure field was effected on account of the inherent physical

fluctuating behaviour and instability of the partially developed air core.

5. **The Algebraic Slip Mixture Model (ASMM) is suited to modelling multiphase hydrocyclone flows**
   Despite reports that the ASMM is unsuitable for modelling hydrocyclone flows in which the secondary phases are in excess of 10% by volume, which is representative of typical slurry operating conditions, physically realistic multiphase flow fields were predicted at a fraction of air of 50% by volume, that was introduced as part of the feed. A precessing, partially developed and inherently unstable air core was also induced at the spigot discharge orifice. The numerical results reflected relative motion between the primary and secondary phases, indicating that the implementation of the ASMM which employs the slip velocity formulation is better suited to modelling multiphase hydrocyclone flows, in contrast to the homogeneous variant which was adopted in this work in order to achieve economy with simulation run times.

6. **Adequate resolution of the hydrocyclone flow field is only attainable via the transient solver**
   The hydrocyclone flow field exhibits transient behaviour and is inadequately resolved via the steady state solver. Upon application of the transient solver, an improvement in the definition of the velocity and pressure field profiles was demonstrated, for a flow field initially resolved via the steady state solver. Notably, however, upon adoption of the transient solver, it proved necessary to effect double precision numerical representation in order to achieve solution convergence at every simulation time step.

7. **Second order accurate discretisation schemes should provide adequate discretisation of the governing transport equations while ensuring solution stability**
   Instabilities leading to diverged solutions were encountered in the numerical resolution of the hydrocyclone flow field via the third order accurate QUICK discretisation scheme, even with continued relaxation of the convergence criteria. Solution stability and convergence was achieved through the implementation of the first order accurate upwind differencing scheme. This observation seemingly suggests, in accordance with reports presented in the literature, that second order accurate discretisation schemes should provide adequate discretisation of the governing transport equations while ensuring solution stability. Bearing in mind that grid-related instabilities and grid independence of the solution flow fields were not investigated, such a conclusion is not reached with absolute certainty.

8. **Standard wall functions provide an adequate means for resolution of the near-wall hydrocyclone flow field**
   Bulk flow velocity and pressure field profile predictions that are consistent with experimentally-determined and inferred trends were obtained via the RSM. Resolution of the near-wall hydrocyclone flow field via standard wall functions revealed the tangential velocity component to represent the most critical flow field variable, on account of its exhibition of the steepest local velocity gradients. Numerically predicted tangential velocity field profiles that were derived from a specific grid configuration, under-predicted an experimental data set in the near-wall region, revealing the associated grid-related inadequancy, with respect to the implementation of standard wall functions. It was also demonstrated, however, that by giving careful consideration when generating the grid, it may be so-defined as to satisfy the y^* criteria such as to ensure the appropriate implementation of standard wall functions.

9. **The classical understanding of the hydrocyclone radial particle classification mechanism is partially flawed**
   The account of the hydrocyclone radial particle classification mechanism given by the particle equilibrium orbit theory, which assumes a particle centrifugal-drag force balance in the radial direction, with centrifugal drift of large particles towards the cyclone wall and radial drag of small particles towards the core, is simplistic and only partially valid. The CFD predictions revealed that within significant portions of some regions of the hydrocyclone, the centrifugal and drag forces are, in fact, additive i.e. directed radially outwards such as to enhance centrifugal drift of particles. In addition, the liquid radial velocity component values were the least in magnitude. As such, the predicted numeric values thereof, seem to suggest that radial particle displacement and classification are predominantly due to centrifugal forcing action and that inward radial particle migration is a mass diffusion effect.

10. **Air core inception is pressure-driven while the subsequent development thereof is partially transport-aided**
    The establishment of a negative core pressure, particularly within the spigot, is paramount to the suction of air being effected across the spigot discharge orifice. The central location of an air stream with the potential for development into an air column, is supported by a negative core pressure. The inward radial migration of any dispersed air bubbles is facilitated by the positive bulk flow pressure field, which drives the less dense secondary gaseous phase towards the core on account of the negative pressure gradient established in this direction as well as

the density differences exhibited between the primary and secondary phases. The subsequent development of a centrally-positioned air column is partially effected via convective transport. The negative axial pressure gradient that is established in the direction of the roof of the cyclone supplements the air core development mechanism by facilitating pressure-driven gaseous diffusion of the centrally located air stream towards the higher positioned lower pressure region. Inasmuch as the upward-directed axial flow reversal is effected prior to the establishment of a negative core pressure, the latter may be deemed to constitute the primary air core development mechanism because the inception and fluctuation-induced instability of the air core are largely influenced by the relatively unstable rapidly fluctuating internal pressure field.

11. **Shock effects enhance turbulence mixing in the feed entry section of a hydrocyclone**

    Excessive turbulence was predicted within the feed entry section of the hydrocyclone. The establishment of a turbulent flow field in this region may be attributed to the collision of the main chamber swirl flow field and the inlet feed stream. The predicted consequent shock effects should, in accordance with literature reports, enhance turbulence mixing in this region. It was further established that the cross-sectional geometry of the inlet has a significant effect on the extent of the shock and turbulence mixing effected in this region.

Chapter 6

Recommendations for Future Work

With regard to the extent to which the objectives of this research project have been fulfilled, the following recommendations, with respect to future research on this subject, are made:

1. **Expand on the outcomes of the current research by using the established two-product CFD hydrocyclone models to:**
    (a) Develop an air core and to investigate its dynamics and influence on the hydrocyclone flow field.
    (b) Facilitate observation of the effects of variable viscosity on the flow, for a fixed set of boundary conditions.
    (c) Employ the Lagrangian particle model to obtain three-dimensional particle tracking predictions within the hydrocyclone flow field, through the introduction of a limited number of various-sized solid particles, as a post-processing phase.
    (d) Investigate high wear regions and to undertake parametric geometry optimisation, in order to identify means by which turbulence and component wear may be minimised.
    (e) Investigate the potential of employing CFD to provide classification data as well as insight into the classification mechanism within the hydrocyclone.
    (f) Obtain validation thereof, via suitable experimental data and to extend the application of the acquired knowledge to modelling the flow field within a three-product cyclone, operated at practical slurry concentrations.

2. **Employ an Eulerian-Eulerian multiphase algorithm in conjunction with the Reynolds Stress Model (RSM)**
   A complete Eulerian-Eulerian multiphase algorithm, which solves distinct momentum equations for each secondary phase, represents the most definitive methodology currently available for modelling hydrocyclone flows with phasic volume fractions representative of typical operating conditions [7] [52]. However, the version of Fluent [8] used in this research only implements an Euler-Euler algorithm if the ASMM is used in conjunction with the standard k-ϵ model, which was reported in chapter 2, section B.1.1 (c), to inadequately resolve highly swirling flow fields such as that presented by the hydrocyclone. Unfortunately, if used with the RSM, which has, through successful implementation with both single and multiphase flows [7] [37], been shown to represent the minimum order of accuracy for modelling hydrocyclone flow turbulence, the ASMM employs an Euler-Lagrange algorithm.

3. **Employ the higher order Large Eddy Simulation (LES) model for turbulence modelling**
   The LES model represents the highest order of accuracy of turbulence modelling within the version of Fluent [8] used in this research. However, despite providing an alternative to the RSM, it is computationally more expensive [51] because of the requirement of excessively fine grids, in order to model the effects of sub-grid scale eddies. The preferential adoption of the RSM over the LES was motivated by the restriction imposed by the computational capacity of the computational resources (3.06 GHz Pentium 4 processor, 2 GB RAM) utilised.

4. **Track the air-water interface via the Volume of Fluid (VOF) model**
   The homogeneous implementation of the ASMM should be used to the point of air core formation in order to achieve economy with simulation run times of multiphase flows. The VOF model should then be used subsequently, to track the air-water interface within the hydrocyclone flow field. The variant of the ASMM which employs the slip velocity formulation provides an alternative to the VOF model.

5. **Conduct grid independence studies and investigate the effects of grid density on solution stability**
   Computational expense and time constraints prevented the conduction of grid independence studies. The lack of experimental data of water-only operated cyclones meant that the integrity of any results derived from such CFD studies could also not be verified. Grid-related instabilities have been reported by Bren-

nan [50], who observed high numeric instabilities that led to diverged solutions of hydrocyclone flow fields resolved via excessively fine geometry grids. It has, in fact been suggested by Brennan [50] and Cullivan [56], to employ grids as coarse as 70 000 volume mesh elements, to initiate and develop the hydrocyclone flow field to the point of establishment of an air core, in order for numerically stable solutions to be obtained. Following this, the implementation of grid adaptation, such as to ensure sufficient volume mesh resolution in regions exhibiting large variations in flow variables, is also suggested. Such a solution strategy, although successfully implemented by Brennan [50], is coupled with the shortfalls of numeric diffusion highlighted in chapter 2, sections 2.2.2 (a) and (b), which further compound the diffusive effects of the strongly convective hydrocyclone flow.

It has been established that, inasmuch as CFD presents a useful research and design tool because of its inherent capibility to facilitate parametric studies, it inevitably requires continued reference to experimental investigation in order to achieve adequate profession. The various limitations imposed on CFD hydrocyclone modelling, in spite of which, useful numerical predictions of hydrocyclone flow fields were obtained, were higlighted. As such, it is hoped that an improved understanding of the hydrodynamic behaviour of hydrocyclone flow fields and the CFD modelling thereof, has been gained, that will facilitate the definition of more refined research objectives for future related work. With advances in the computational capability of computer hardware as well as in the numeric algorithms that are incorporated in commercial CFD codes, the prospects of future CFD hydrocyclone modelling look bright.

Bibliography

[1] D. T. Tarr Jr., "Hydrocyclones," in *SME Mineral Processing Handbook*, N. L. Weiss, Ed. New York: Society of Mining Engineers of the American Institute of Mining, Metallurgical, and Petroleum Engineers, Inc., 1985, pp. 3D1–3D59.

[2] M. D. Slack and A. E. Wraith, "Modelling the velocity distribution in a hydrocyclone," *4th International Colloquium on Process Simulation*, pp. 65–83, 1997.

[3] E. G. Kelly and D. J. Spottiswood, *Introduction to Mineral Processing*. New York: John Wiley and Sons, Inc., 1982.

[4] S. K. Kawatra, A. K. Bakshi, and M. T. Rusesky, "Effect of viscosity on the cut size of hydrocyclone classifiers," *Minerals Engineering*, vol. 9, no. 8, pp. 881–891, 1996.

[5] M. D. Slack, "AC-cyclone separator," Fluent Europe Ltd., 2002.

[6] K. T. Hsieh, "Phenomenological model of the hydrocyclone," Ph.D. dissertation, University of Utah, Utah, USA, December 1988.

[7] M. Slack, S. Del Porte, and M. S. Engelman, "Designing automated computational fluid dynamics modeling tools for hydrocyclone design," in *Proceedings Hydrocylones '03*, Cape Town, South Africa, 24 - 26 September 2003.

[8] "Fluent v6.1.22 user's manual," Fluent Inc., February 2003.

[9] J. H. J. Burrows *et al.*, *Environmental Engineering in South African Mines*. Cape Town, South Africa: The Mine Ventilation Society of South Africa, 1982.

[10] R. A. Williams, "The impact of fundamental research on minerals processing operations of the future," in *Proceedings of the XXII International Mineral Processing Congress*, L. Lorenzen *et al.*, Eds. Cape Town, South Africa: The South African Institute of Mining and Metallurgy, 28 September - 3 October 2003, pp. 1–12.

[11] R. B. Batterham, "The mine of the future; will it be visible," in *Proceedings of the XXII International Mineral Processing Congress*, L. Lorenzen *et al.*, Eds. Cape Town, South Africa: The South African Institute of Mining and Metallurgy, 29 September - 3 October 2003, pp. 40–48.

[12] J. S. J. Van Deventer and G. C. Lukey, "Sustainability in the minerals industry; threat or opportunity," in *Proceedings of the XXII International Mineral Processing Congress*, L. Lorenzen *et al.*, Eds. Cape Town, South Africa: The South African Institute of Mining and Metallurgy, 29 September - 3 October 2003, pp. 22–40.

[13] M. Stewart, G. Brent, and G. Petrie, "The application of life cylce assessment to mining and minerals," in *Proceedings of the XXII International Mineral Processing Congress*, L. Lorenzen *et al.*, Eds. Cape Town, South Africa: The South African Institute of Mining and Metallurgy, 29 September - 3 October 2003, p. 481.

[14] H. Von Blottnitz and J. Broadhurst, "Life cycle assessment in multi-product metals refining; a project planning support tool," in *Proceedings of the XXII International Mineral Processing Congress*, L. Lorenzen *et al.*, Eds. Cape Town, South Africa: The South African Institute of Mining and Metallurgy, 29 September - 3 October 2003, p. 353.

[15] T. J. Olson *et al.*, "Improving milling circuits through aggressive approach to cyclone and overall circuit operation," in *Proceedings of the XXII International Mineral Processing Congress*, L. Lorenzen *et al.*, Eds. Cape Town, South Africa: The South African Institute of Mining and Metallurgy, 29 September - 3 October 2003, p. 319.

[16] D. F. Kelsall, "A study of the motion of solid particles in a hydraulic cyclone," *Transactions Institute Chemical Engineers*, vol. 30, pp. 87–101, 1952.

[17] T. Dyakowski and R. A. Williams, "Modelling turbulent flow within a small-diameter hydrocylone," *Chemical Engineering Science*, vol. 48, no. 6, pp. 1143–1152, 1993.

[18] H. K. Versteeg and W. Malalasekera, *An Introduction to Computational Fluid Dynamics: The Finite Volume Method*. England: Longman Scientific and Technical, 1995.

[19] T. J. Olson and R. Van Ommen, "Optimising hydrocyclone design using advanced CFD model," in *Proceedings Hydrocyclone '03*, Cape Town, South Africa, 24 -26 September 2003.

[20] A. Mainza, M. S. Powell, and B. Knopjes, "Differential classification of dense material in a three product cyclone," in *Proceedings Hydrocyclones '03*, Cape Town, South Africa, 24 - 26 September 2003.

[21] S. V. Patankar, *Numerical Heat Transfer and Fluid Flow*. New York: Hemisphere Publishing Corporation, Taylor and Francis Group, 1980.

[22] N. Chakraborti and J. D. Miller, "Fluid flow in hydrocyclones; a critical review," *Mineral Processing and Extractive Metallurgy Review*, vol. 11, pp. 211 244, 1992.

[23] B. Chine and F. Concha, "Flow patterns in conical and cylindrical hydrocyclones," *Chemical Engineering Journal*, vol. 80, pp. 267 273, 2000.

[24] J. Turner, "The application of microcyclones in the minerals, chemicals, food, oil and gas industries," in *Proceedings Hydrocylones '03*, Cape Town, South Africa, 24 - 26 September 2003.

[25] C. A. Petty and S. M. Sparks, "A new class of hydrocyclones for downhole oil-water separation," in *Proceedings Hydrocylones '03*, Cape Town, South Africa, 24 - 26 September 2003.

[26] K. A. Hashmi, H. A. Hamza, and J. C. Wilson, "CANMET hydrocyclone; an emerging alternative for the treatment of oily waste streams," in *Proceedings Hydrocylones '03*, Cape Town, South Africa, 24 - 26 September 2003.

[27] L. Svarovsky, *Hydrocyclones*. New York: Technomic Publishing Co., Inc., 1984.

[28] O. Levenspiel, *Chemical Reaction Engineering*, 2nd ed. New York: John Wiley and Sons, 1972.

[29] C. Fredriksson, "Exploratory experimental and theoretical studies of cyclone gasification of wood powder," Ph.D. dissertation, Luleå University of Technology, Luleå, Sweden, August 1999.

[30] S. K. Kawatra, A. K. Bakshi, and M. T. Rusesky, "The effect of slurry viscosity on hydrocyclone classification," *Minerals Engineering*, no. 18, pp. 39 50, 1996.

[31] J. C. Cullivan, R. A. Williams, and C. R. Cross, "Understanding the hydrocylone separator through computational fluid dynamics," *Institution of Chemical Engineers. Transactions IChemE*, vol. 81, Part A, pp. 455 466, 2003.

[32] B. A. Wills, *Mineral Processing Technology: An Introduction to the Practical Aspects of Ore Treatment and Mineral Recovery*, 6th ed. Oxford: Butterworth-Heinemann, 1997.

[33] L. R. Plitt, "A mathematical model of the hydrocyclone classifier," *CIM Bulletin*, vol. 69, pp. 114 – 123, 1976.

[34] R. A. Williams *et al.*, "Using electrical impedance tomography for controlling hydrocylone underflow discharge," *Control Engineering Practice*, vol. 5, no. 2, pp. 253 – 256, 1997.

[35] R. A. Williams, O. M. Ilyas, and T. Dyakowski, "Air core imaging in cyclonic separators using electrical resistance tomography," *Coal Preparation*, vol. 15, pp. 149 – 163, 1995.

[36] J. F. Douglas, J. M. Gasiorek, and J. A. Swaffield, *Fluid Mechanics*, 3rd ed. Singapore: Longman Scientific and Technical, 1995.

[37] M. S. Brennan, "Multiphase CFD simulations of dense medium and classifying hydroyclones," in *Proceedings of the Third International Conference on CFD in the Minerals and Process Industries*, CSIRO, Melbourne, Australia, 10 - 12 December 2003.

[38] A. F. Nowakowski *et al.*, "Application of CFD to modelling of the flow in hydrocyclones; is this a realisable option or still a research challenge," in *Proceedings Hydrocyclones '03*, Cape Town, South Africa, 24 - 26 September 2003.

[39] T. Dyakowski and R. A. Williams, "Prediction of high solids concentration regions within a hydrocylone," *Powder Technology*, vol. 87, pp. 43 – 47, 1996.

[40] D. Leith, "Cyclones," in *Handbook of Powder Science and Technology*, 1st ed., M. E. Fayed and L. Otten, Eds. New York: Chapman and Hall, 1997, pp. 730 – 753.

[41] R. M. West, X. Jia, and R. A. Williams, "Parametric modelling in industrial process tomography," *Chemical Engineering Journal*, vol. 77, pp. 31 – 36, 2000.

[42] L. E. Drain, *The Laser Doppler Technique*. Chichester: John Wiley and Sons Ltd., 1980.

[43] F. M. White, *Viscous Fluid Flow*, 2nd ed. Singapore: McGraw-Hill, Inc., 1991.

[44] S. Schuetz *et al.*, "Investigations on the flow and separation behaviour of hydrocyclones using computational fluid dynamics," 29 April, 2003, accepted for publication by International Journal of Mineral Processing.

[45] S. Grady *et al.*, "Flow field prediction for 10 mm hydrocyclone using computational fluid dynamics," in *Proceedings Hydrocylones '03*, Cape Town, South Africa, 24 - 26 September 2003.

[46] T. C. Monredon, K. T. Hsieh, and R. K. Rajamani, "Fluid flow model of the hydrocyclone; an investigation of device dimensions," *International Journal of Mineral Processing*, vol. 35, pp. 65–83, 1992.

[47] M. D. Slack, "Personal communication," September 2003.

[48] "AC3-03-cyclone separator," Fluent Europe Ltd., 2002.

[49] J. C. Cullivan *et al.*, "New understanding of a hydrocylone flow field and separation mechanism from computational fluid dynamics," *Minerals Engineering*, vol. 17, pp. 651–660, 2004.

[50] M. S. Brennan, "Personal communication," February - July 2004.

[51] E. M. Marshall and A. Bakker, *Computational Fluid Mixing*. USA: John Wiley and Sons, Inc., 2003.

[52] D. Cokljat, M. D. Slack, and S. Vasquez, "Reynolds stress model for eulerian multiphase," 2003, submitted for publication to Turbulence, Heat and Mass Transfer 4.

[53] M. D. Slack *et al.*, "Advances in cyclone modelling using unstructured grids," *Transactions Institute Chemical Engineers*, vol. 78, pp. 1098–1104, 2000.

[54] "Autodesk inventor, v6.0," Autodesk, January 2004.

[55] D. F. Kelsall, "A further study of the hydraulic cyclone," *Chemical Engineering Science*, vol. 2, pp. 254–272, 1953.

[56] J. C. Cullivan, "Personal communication," July 2004.

[57] C. Chen and S. Jaw, *Fundamentals of Turbulence Modeling*. USA: Taylor and Francis, 1998.

[58] D. C. Wilcox, *Turbulence Modeling for CFD*, 2nd ed. California, USA: DCW Industries, Inc., 2000.

[59] A. V. Smol'yakov and V. M. Tkachenko, *The Measurement of Turbulent Fluctuations: An Introduction to Hot-Wire Anemometry and Related Transducers.* Berlin: Springer-Verlag, 1983.

Appendix A

The Experimental Hydrocyclone

Figure A.1 depicts the cylone used in the Laser Doppler Anemometry (LDA) studies conducted by Hsieh [6], in which liquid water velocity components were measured at various horizontal levels along the length of the cyclone. The physical dimensions of the cyclone are indicated in figure A.1 and listed in table A.1.

Part	**Diameter (mm)**	**Height (mm)**
main chamber	75	75
inlet duct	25	-
vortex finder	25	50
spigot	12.5	25
conical chamber (20^0 cone angle)	75	186

Table A.1: Experimental cyclone dimensions

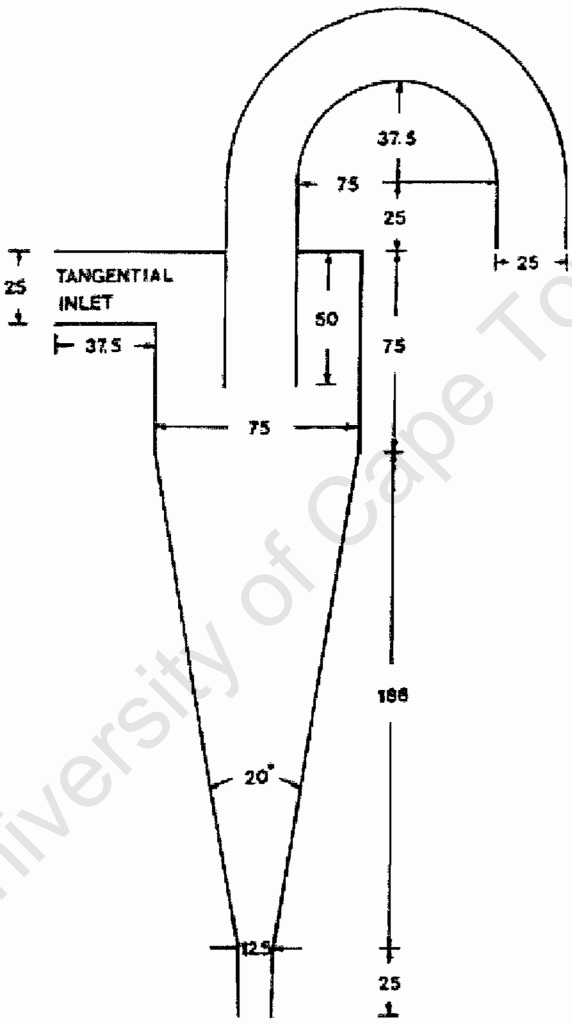

Figure A.1: Experimental hydrocyclone [6]

Appendix B

Computational Fluid Dynamics Fundamentals

This section outlines the mathematical basis of CFD with respect to the equations governing *compressible viscous fluid flow* and the *numerical methods* employed in their solution. Turbulence modelling and the difficulties associated with the selection of an appropriate *turbulence model*, for a specific fluid flow problem, are reviewed. A general overview of the relative performance-related merits of the *k-ε* model, the *Reynolds Stress Model* (RSM) and the *large eddy simulation* (LES) model, which are derived on the basis of computational expense, robustness and universality in application is also presented. Near-wall treatment of turbulent flows, which imposes certain grid requirements, is discussed in the context of the adoption of the *wall function* or *boundary layer meshing* approaches. The discussion on the auxiliary models that are used concurrently with the turbulence models, to model multiphase flows, is limited to the *Algebraic Slip Mixture Model* (ASMM). The solution techniques employed in commercial CFD codes are also discussed, with particular reference to the *finite volume* technique employed in Fluent version 6.1.22.

B.1 The mathematical basis of computational fluid dynamics

This section presents a brief discussion of the mathematical basis of a general purpose *single-component fluid* system, derived from the basic principles of conservation of mass and momentum. The mathematical relations, which are also applicable to *non-reacting mixtures*, describe fluid behaviour in terms of *macroscopic properties* such as velocity, pressure, density and their space and time derivatives. To avoid unduly cumbersome notation, the dependance of the fluid properties on space coordinates and time will not be explicitly stated and all *vector quantities* will be represented in bold typeface. In addition, the compact indicial vector notation will be adopted for some mathematical expressions. The equations governing fluid flow are here merely quoted and given a qualitative treatment. As such, reference to fluid dynamics texts, such as Versteeg [18] and White [43] is encouraged, for more comprehensive equation derivations and discussions.

a) The fundamental equations of compressible viscous fluid flow

The basic equations governing fluid flow, consist the three *laws of conservation* for physical systems viz. [18] [43]:

1. Conservation of mass.
2. Conservation of momentum.
3. Conservation of energy.

These three equations require simultaneous solution for the three unknown fluid variables $\mathbf{V}$, p and T, which represent velocity, thermodynamic pressure and absolute temperature, respectively. The *continuity* and *Navier-Stokes* equations, which are derived from the laws of conservation of mass and momentum are discussed in this section and the law of conservation of energy is mentioned for completeness.

i) The equation of continuity The equation of *continuity* is a statement of the *conservation of mass* of a physical system. With reference to a three-dimensional fluid element, this mass balance may be represented thus:

$$\begin{array}{c} \text{Rate of increase of mass} \\ \text{in fluid element} \end{array} = \begin{array}{c} \text{Net rate of flow of mass} \\ \text{into fluid element} \end{array}$$

By considering the above-stated relation, the *unsteady*, three-dimensional mass conservation or *continuity equation*, at any point in a *compressible fluid*, may be stated thus [18] [43]:

$$\frac{\partial\rho}{\partial t} + div(\rho\mathbf{V}) = 0 \tag{B.1}$$

The non-zero terms in equation B.1 represent the time rate of change of density i.e. mass per unit volume and convection, due to the net flow of mass out of and across the element boundaries, respectively [18]. Equation B.1 can be adapted to describe *steady state* flow of an *incompressible fluid* i.e. a constant density fluid, yielding the expression in equation B.2 [18]:

$$div\mathbf{V} = 0 \tag{B.2}$$

ii) The Navier-Stokes equations The *Navier-Stokes* equations, formulated from *Newton's second law*, are an expression of the *conservation of momentum* of a physical system. With reference to a fluid system, Newton's second law, which relates the change of momentum of and the sum of forces acting on a fluid particle, may be stated thus:

$$\begin{array}{ccc}\text{Rate of increase of momentum} & = & \text{Sum of forces acting}\\ \text{of fluid particle} & & \text{on fluid particle}\end{array}$$

Equation B.3a is the mathematical representation of Newton's second law and it expresses the proportionality between an applied force and the resulting acceleration of a particle of mass m. Fluid particle forces are classified into *surface* and *body forces* and are due to the stresses and forces acting on the surface of and on the entire mass of the fluid element, respectively.

$$\mathbf{F} = m\mathbf{a} \tag{B.3a}$$

Equation B.3a may be re-written on unit volume basis, for a fluid particle, as a summation of a gravitational body force and surface forces, due to stresses resulting from the *stress tensor* τ_{ij}, yielding equation B.3b [43].

$$\rho\frac{D\mathbf{V}}{Dt} = \rho\mathbf{g} + \nabla\cdot\tau_{ij} \tag{B.3b}$$

Assuming a *newtonian fluid*, the stress tensor τ_{ij} is related to the *strain rate tensor* ϵ_{ij} through an assumed viscous deformation-rate law, defined through Stokes' postulates, which stipulate that [43] [57]:

1. The fluid is *continuous* and its stress tensor τ_{ij} is at most a *linear* function of the strain rates ϵ_{ij}.
2. The fluid is *isotropic* i.e. it has direction independent properties, rendering the *deformation law* independent of the coordinate axes in which it is expressed.
3. The deformation law must reduce to the *hydrostatic pressure condition* given by equation B.4, when the strain rates are *zero*.

$$\tau_{ij} = -p\delta_{ij} \tag{B.4}$$

where

$$\delta_{ij} = \left\{ \begin{array}{ccccc} 1 & ; & \text{if} \quad i & = & j \\ 0 & ; & \text{if} \quad i & \neq & j \end{array} \right\}$$

When all three postulates are satisfied, the resulting deformation law for the newtonian viscous fluid is given by [43]:

$$\tau_{ij} = -p\delta_{ij} + \mu\epsilon_{ij} + \delta_{ij}\lambda div\mathbf{V} \tag{B.5}$$

where

$$\epsilon_{ij} = \left(\frac{\partial u_i}{\partial x_j} + \frac{\partial u_j}{\partial x_i}\right)$$

The final desired momentum equation for a general newtonian viscous fluid is formulated by substituting equation B.5 into Newton's second law, as given by equation B.3a. The result is the *Navier-Stokes* equation of motion given by equation B.6 [43].

$$\rho\frac{D\mathbf{V}}{Dt} = \rho\mathbf{g} - \nabla p + \frac{\partial}{\partial x}\left(\mu\epsilon_{ij} + \delta_{ij}\lambda div\mathbf{V}\right) \tag{B.6}$$

Although fluid flow characterisation can be achieved through the relations in equations B.1 and B.6, the following incorporated assumptions should be borne in mind [43]:

- the fluid forms a mathematical continuum
- the fluid particles are essentially in thermodynamic equilibrium

- the body force component only consists gravitational forces

Regrettably, CFD is founded on the *partial differential* Navier-Stokes equations, which although fundamental and rigorous, are *non-linear*, *non-unique*, complex and solved with great difficulty [43]. As such, very few publications of particular analytical solutions exist and the normal resolve is to employ numerical solution techniques via CFD [18].

B.1.1 Turbulence and CFD modelling thereof

Turbulence may be described as an *irregular multi-scaled* condition of flow in which the various flow quantities exhibit a *random* variation with *time* and *space coordinates*, so that *statistically distinct average values* can be discerned [58]. The random nature of the *fluctuations* in turbulent flow quantities leads to its study by statistical and probabilistic methods [59]. The *instantaneous* properties of turbulent flows are extremely sensitive to initial conditions [58] and consequently, the experimental measurement thereof is complicated. Fortunately, only average statistical turbulence parameters, which are insensitive to initial flow conditions [58], are normally of practical interest, in contrast to instantaneous values [59]. As such, experimentally determined turbulent properties may be used as the basis for formulating models explaining these properties [59]. The diversity of the subject matter prohibits a full rigor of the analytical proof of present-day turbulence models as well as a comprehensive discussion of related theory. What ensues therefore is a concise presentation of the basic ideas of turbulence and the CFD modelling thereof, without the introduction, whenever possible, of excessive mathematical complication.

a) Turbulent flow characterisation

i) Reynolds number effects It is common practice to define a critical value of the *Reynolds number*, Re_c, given by equation B.7 [18], to mark the *transition* from laminar to turbulent flow conditions. The intermediate transition process does not however occur at a unique value of the Reynolds number such as Re_c, but rather over a range of values, prior to the onset of turbulence. In a physical sense, Re for a given flow gives a measure of the relative importance of *inertia forces*, associated with *convective effects*, and *viscous forces* [36].

$$Re_c = \frac{\overline{u}L}{\nu} \tag{B.7}$$

ii) Turbulent quantity characterisation The random nature of turbulent flow effects phenomenal intricacy in the formulation of a complete mathematical description of the motion of all particles contained within a turbulent fluid flow field [59]. As such, turbulent flow is normally characterised by the *mean values* of flow properties and the *statistical properties* of their *fluctuations*. A turbulent velocity quantity $u(t)$, for example, may be decomposed as indicated in equation B.8, where $\overline{u}$ and $u'(t)$ represent the *mean* and *fluctuating* velocity components respectively. The turbulent fluctuations always have a *three-dimensional* spatial character even for flows where the mean velocities and pressures vary in one or two space dimensions.

$$u(t) = \overline{u} + u'(t) \tag{B.8}$$

ii) Turbulent eddy effects Turbulent flow is also characterised by *turbulent eddies*, which constitute a rotational flow structure of intense *vorticity* and a wide range of *length scales*. The eddy motion causes *effective mixing* within a fluid, which in turn gives rise to high mass, momentum and heat diffusion coefficients. The characteristic velocity and length scales of the mean flow and the large eddies are of the same order of magnitude and the latter are similarly dominated by inertial versus viscous effects. The largest turbulent eddies interact with and extract energy from the mean flow through a process termed *vortex stretching*, which is the mechanism through which turbulence is sustained. This phenomenon is complimented by an *energy cascade* i.e. a mechanism by which kinetic energy is handed down from larger eddies to progressively smaller and smaller eddies. The energy associated with eddy motion is additionally dissipated and converted into *thermal internal energy* of the fluid system, as a result of the *work* done to counteract molecular viscosity.

A structural difference prevails between the largest and smallest eddies due to their varying levels of interaction with the mean flow. As such, the largest eddies, which interact strongly with the mean flow, are highly *anisotropic* in contrast to the *isotropic* character exhibited by the smallest eddies. The isotropic nature of the smallest eddies is due to the diffusive action of the fluid viscosity, which is relatively significant and tends to smear out directionality at small scales. Fluid viscosity also dictates the smallest scale of motion occuring in turbulent flow. As such, the Reynolds number of the smallest eddies, formulated on the basis of their characteristic velocities and length scales, is limited to a numeric value of 1. This result tends to suggest *creeping* or *Stokes' flow* [43] of small eddy motion. The preceding discussion on turbulent flow characterisation is largely due to Versteeg [18] and Wilcox [58].

b) The Reynolds averaged equations of turbulent motion

Inasmuch as flow visualisation techniques supplement our knowledge of the physical structure of turbulent flows [43], they are incapable of providing quantitative information [59], which would perhaps be more beneficial. These techniques can however be supplemented by modern instrumentation such as hot wire anemometers, laser doppler velocimeters and pressure transducers, capable of quantitative measurement of the desirable statistical turbulence quantities [59]. Nonetheless, if improved understanding of turbulent flow phenomena is to be achieved, the need for a mathematical description of turbulence is not removed. It is in this regard that the *time-averaged Navier-Stokes* or the so-called *Reynolds averaged equations*, which are necessary for the numerical solution of turbulent flow [18] [43] [58], were formulated. Fortunately, despite the associated computational expense [58], the computational procedures normally adopted for practical flows supply adequate information about the significant time-averaged properties of turbulent flows [18].

i) The turbulence closure problem Although the *instantaneous* continuity and Navier-Stokes equations i.e. equations B.1 and B.6 respectively, provide mathematical descriptions for both the laminar and turbulent flow regimes, they only provide system closure for the former [18]. This equation *closure* permits the determination of the velocity, pressure and stresses generated at any point within the fluid flow field [59]. With regard to turbulent flows, the instantaneous values of the random fluctuations are of no interest and as such, equations B.1 and B.6 require modification to enable the description of the significant statistically averaged values of the turbulent flow quantities [59]. The Reynolds averaged equations constitute this modification and thus contribute towards bringing closure to the system of equations governing turbulent fluid flow.

ii) Turbulent quantity determination The standard analysis of turbulence by means of the time-mean and fluctuating property values, as in the decomposition of the turbulent velocity quantity $u(t)$ in equation B.8, has already been discussed. In the discussion that ensues, the time averaging of turbulent quantities is illustrated through use of the turbulent velocity quantity and the notation adopted does not explicitly indicate time dependence of the former. As such, the *time average* of the mean velocity $\overline{u}$ is defined by equation B.9 [57], where the *period* or *integration interval* T is chosen to be larger than any significant period of fluctuations in u [18] [43].

$$\overline{u} = \frac{1}{T}\int_0^T u \, dt \tag{B.9}$$

With a knowledge of $\overline{u}$, the fluctuating velocity component u' is subsequently determined through suitable manipulation of equation B.8. By definition, the time-average of the fluctuations, as given by equation B.10, is zero [18] [43]. Consequently, the magnitude of this component, verifiable experimentally, is determined via the *root-mean-square* (rms) formulation given by equation B.11 [18]. With reference to a Cartesian coordinate system, if fluctuating turbulent velocity components are determined in all three coordinate directions, the turbulent kinetic energy per unit mass of the flow is readily determined via equation B.12 [18] [58].

$$u' = \frac{1}{T}\int_0^T u'\,dt \equiv 0 \tag{B.10}$$

$$u'_{rms} = \sqrt{\overline{(u')^2}} = \left[\frac{1}{T}\int_0^T (u')^2 \;dt\right]^{\frac{1}{2}} \tag{B.11}$$

$$k = \frac{1}{2}\left(\overline{(u')^2} + \overline{(v')^2} + \overline{(w')^2}\right) = \frac{1}{2}\overline{u_i'u_i'} \tag{B.12}$$

iii) The Reynolds Averaged Navier-Stokes equation The fundamental fluid flow governing instantaneous continuity and Navier-Stokes equations i.e. equations B.1 and B.6 respectively, when modified through time and turbulent quantity averaging as to mathematically describe turbulent fluid flow motion, yield the Reynolds averaged equations [18]. As such, provided density fluctuations are neglected, the mean and fluctuating velocity components of a turbulent flow can be shown to separately exhibit zero divergence [58], in the same manner as the effective velocity, in the instantaneous form of the continuity expression given by equation B.1.

The generic form of the momentum equation for turbulent flow is termed the *Reynolds Averaged Navier-Stokes* (RANS) equation and is given by the relation [51]:

$$\begin{aligned}\frac{\partial\left(\rho\overline{u}_i\right)}{\partial t} + \frac{\partial}{\partial x_j}\left(\rho\overline{u}_i\overline{u}_j\right) \;=\;& \frac{\partial p}{\partial x_i} + \frac{\partial}{\partial x_j}\left[\mu\left(\frac{\partial\overline{u}_i}{\partial x_j} + \frac{\partial\overline{u}_j}{\partial x_i} - \frac{2}{3}\frac{\partial\overline{u}_k}{\partial x_k}\partial_{ij}\right)\right] \\ &+\frac{\partial}{\partial x_j}\left(-\rho\overline{u_i'u_j'}\right) + \rho g_i + F_i\end{aligned} \tag{B.13}$$

where F_i represents body forces and $\overline{u}_i$, directional mean velocities. Save for the replacement of instantaneous by average values, the only significant difference between momentum equations B.6 and B.13 is the introduction of the *turbulent inertia tensor* $\overline{u_i'u_j'}$ [43]. If all mean properties of a turbulent flow are to be determined, it becomes necessary to introduce an additional stress conservation equation [58]. It is common practice to express the turbulent inertia tensor terms as stresses given by $\rho\overline{u_i'u_j'}$, as in equation B.11. In a mathematical sense, these so-called *Reynolds stresses*, contribute an apparent stress to the overall system stress by compounding the newtonian viscous stress.

$$\tau_{ij} = \mu\left(\frac{\partial u_i}{\partial x_j} + \frac{\partial u_j}{\partial x_i}\right) - \rho\left(\overline{u_i^{\prime} u_j^{\prime}}\right) \tag{B.14}$$

Assuming an isotropic fluid, as per Stokes' postulates, the nine unknowns in the Reynolds stress tensor, introduced through Reynolds averaging, are reduced to six independent components and require solution thereof. For general three-dimensional flow, the six unknown Reynolds stress tensor components compound the four unknown mean flow properties, consisting pressure and the three velocity components, bringing the total number of unknowns to a grand total of ten [58]. The mathematical nature of Reynolds averaging, which precludes the introduction of any additional physical principles, effects turbulence non-closure. System closure is thus achieved through the introduction of the Reynolds stress equation, discussed in the subsequent section.

iv) The Reynolds stress equation If it is attempted to express the turbulent kinetic energy relation, given by equation B.12, by a single velocity scale, so as to derive the associated conservation relation, the result is equation B.15 [43]. Similarly, if a conservation equation is derived for a solitary Reynolds stress, the result is equation B.16 [43].

$$\begin{aligned}\frac{Dk}{Dt} = & -\frac{\partial}{\partial x_i}\left[\overline{u_i^{\prime}\left(\frac{1}{2}u_j^{\prime}u_j^{\prime} + \frac{p^{\prime}}{\rho}\right)}\right] - \overline{u_i^{\prime}u_j^{\prime}}\frac{\partial \overline{u}_j}{\partial x_i} + \frac{\partial}{\partial x_i}\left[\overline{\nu u_j^{\prime}\left(\frac{\partial u_i^{\prime}}{\partial x_j} + \frac{\partial u_j^{\prime}}{\partial x_i}\right)}\right] \\ & -\nu\overline{\frac{\partial \overline{u}_j^{\prime}}{\partial x_i}\left(\frac{\partial u_i^{\prime}}{\partial x_j} + \frac{\partial u_j^{\prime}}{\partial x_i}\right)}\end{aligned} \tag{B.15}$$

$$\begin{aligned}\underset{\text{(I)}}{\frac{D\overline{u_i^{\prime}u_j^{\prime}}}{Dt}} = & -\underset{\text{(II)}}{\left[\overline{u_j^{\prime}u_k^{\prime}}\frac{\partial \overline{u}_i}{\partial x_k} + \overline{u_i^{\prime}u_k^{\prime}}\frac{\partial \overline{u}_j}{\partial x_k}\right]} - \underset{\text{(III)}}{2\nu\overline{\frac{\partial u_i^{\prime}}{\partial x_k}\frac{\partial u_j^{\prime}}{\partial x_k}}} + \underset{\text{(IV)}}{\overline{\frac{p^{\prime}}{\rho}\left(\frac{\partial u_i^{\prime}}{\partial x_j} + \frac{\partial u_j^{\prime}}{\partial x_i}\right)}} \\ & \underset{\text{(V)}}{-\frac{\partial}{\partial x_k}\left[\overline{u_i^{\prime}u_j^{\prime}u_k^{\prime}} - \nu\frac{\partial\overline{u_i^{\prime}u_j^{\prime}}}{\partial x_k} + \overline{\frac{p^{\prime}}{\rho}\left(\delta_{jk}u_i^{\prime} + \delta_{ik}u_j^{\prime}\right)}\right]}\end{aligned} \tag{B.16}$$

Consider adopting a notation where the terms in equation B.16 are numbered from left to right and uniquely distinguished by grouping and/or bracketing the relevant expressions. As such, the terms in equation B.16, as represented by the Roman numerals, therefore denote:

I – rate of change of Reynolds stress
II – stress generation
III – energy dissipation
IV – pressure strain effects
V – diffusion Reynolds stress

Accounting for all symmetries, the Reynolds stress equation alone, introduces twenty-two additional unknowns, over and above the ten stemming from Reynolds averaging, but nonetheless brings system closure [58].

Regrettably, many present-day turbulence models cannot distinguish the individual normal Reynolds stresses and as such, only incorporate the turbulent kinetic energy k [58]. The normal resolve is to assume isotropic conditions for the velocity fluctuations and to specify a relative turbulence intensity T^r, defined in percentage form by equation B.17 [58].

$$T^r = 100\sqrt{\frac{2}{3}\frac{k}{\overline{u}_\infty^2}} \tag{B.17}$$

Furthermore, inasmuch as the Reynolds averaged and Reynolds stress equations facilitate closure of the mathematical turbulence model, their numerical solution is computationally expensive. It is therefore hoped that an appreciation of the complexity in form of equation B.16, i.e. the Reynolds stress equation, gives an indication of the level of sophistication required of the turbulence models necessary for its efficient numerical solution. The turbulence models used for the numerical modelling of turbulent flow phenomena are discussed in the subsequent section. The preceding section, which presented a discussion on the Reynolds equations, is largely due to White [43].

c) CFD turbulence models

Perhaps the most notable pioneering work done on turbulence modelling is due to Boussinesq, who proposed the *eddy viscosity* approximation in 1877. Further developments that led to time averaging of the Navier-Stokes equations in 1895, were due to Reynolds. In 1925, Prandtl introduced the *mixing length hypothesis* which provided a prescription for computing the eddy viscosity. The contributions made by these researchers formed the basis of subsequent turbulence modelling research [58], which has seen the evolution of numerous turbulence models. Table B.1 [18] presents two categories of turbulence models, distinguishable on the basis of their formulation and/or

Classical models	Based on Reynolds averaged equations 1. zero equation model - mixing length model 2. two equation model - k-ϵ model 3. Reynolds stress equation model 4. algebraic stress model
Large eddy simulation model	Based on space-filtered equations

Table B.1: Turbulence model classification

solution procedure, which either involves Reynolds averaging or space-filtering of the flow governing equations. Further classification of the turbulence models is derived on the basis of the number of differential equations requiring solution, in addition to those that govern the conservation of physical systems [58].

The function of turbulence modelling is to devise approximations for the unknown turbulence defining correlations in terms of known flow properties, so as to provide system closure [58]. Such is the purpose of turbulence models. Inevitably, no single turbulence model is adjudged universal, hence the choice thereof, suited for a particular application, requires careful consideration. By virtue of precluding a length scale, a turbulence model is defined as *incomplete*, the significance of which dictates that additional flow-related information, excluding initial and boundary conditions, should be known a priori, in order for a solution to be obtained [58]. Although this seemingly discredits *zero equation models*, they are nonetheless not without merit as a result of being of value to numerous engineering applications [58]. The inclusion of some of the models listed in table B.1 is merely for completeness. In contrast, the subsequent discussion is limited to turbulence models relevant to this dissertation, as indicated in chapter 1, section 1.5.

i) The Boussinesq hypothesis The Boussinesq hypothesis, the statement of which is given by equation B.18, assumes that the Reynolds stresses can be expressed in terms of the mean velocity gradients [51]. The newly introduced constant μ_t, which is dimensionally equivalent to viscosity, is termed the *turbulent* or *eddy viscosity*, and is modelled using the expression given by equation B.19. The terms C_μ and ϵ in equation B.19, represent an empirical constant and the dissipation of turbulent kinetic energy, respectively. In addition, the effective viscosity μ_e, given by equation B.20, is obtained through algrebraic manipulation of equations B.13 and B.18 [51]. In addition to equations B.18 and B.20, the hypothesis also incorporates the turbulent kinetic energy per unit mass k [51], given by equation B.12, and here reproduced for completeness.

$$\overline{\rho u_i' u_j'} = \frac{2}{3}\rho k \delta_{ij} + \mu_t \left(\frac{\partial \overline{u}_i}{\partial x_j} + \frac{\partial \overline{u}_j}{\partial x_i}\right) \tag{B.18}$$

$$\mu_t = \rho C_\mu \frac{k^2}{\epsilon} \tag{B.19}$$

$$\mu_e = \mu + \mu_t \tag{B.20}$$

$$k = \frac{1}{2}\left(\overline{(u')^2} + \overline{(v')^2} + \overline{(w')^2}\right) = \frac{1}{2}\overline{u_i' u_i'} \tag{B.21}$$

The computational procedure of a turbulence model is such as to compute the Reynolds stresses to provide system closure. One such procedure involves computing the quantities k and μ_t for successive back substitution into equations B.18 and B.13 [51]. Inevitably, variable computational procedures are adopted by different turbulence models in approximating the Reynolds stresses. As such, the suitability of a turbulence model, for prescribed flow conditions, is detemined by the extent of applicability of the incorporated assumptions.

ii) The k-ϵ model The *k-ϵ model* solves for the Reynolds stresses by solving two equations, in addition to the primary conservation equations. Equations B.22 and B.23 constitute the two additional transport equations that require solution by this model and represent the *turbulent kinetic energy* k and the *rate of dissipation of turbulence* ϵ, respectively [51] [58]. The quantity G_k, given by equation B.24, represents a turbulence generation term [51].

$$\frac{\partial(\rho k)}{\partial t} + \frac{\partial}{\partial x_i}(\rho \overline{u}_i k) = \frac{\partial}{\partial x_i}\left(\mu + \frac{\mu_t}{\sigma_k}\right)\frac{\partial k}{\partial x_i} + G_k - \rho\epsilon \tag{B.22}$$

$$\frac{\partial(\rho\epsilon)}{\partial t} + \frac{\partial}{\partial x_i}(\rho \overline{u}_i \epsilon) = \frac{\partial}{\partial x_i}\left(\mu + \frac{\mu_t}{\sigma_\epsilon}\right)\frac{\partial \epsilon}{\partial x_i} + C_1\frac{\epsilon}{k}G_k + C_2\rho\frac{\epsilon^2}{k} \tag{B.23}$$

where

$$G_k = \mu_t\left(\frac{\partial \overline{u}_i}{\partial x_j} + \frac{\partial \overline{u}_j}{\partial x_i}\right)\frac{\partial \overline{u}_j}{\partial x_i} \tag{B.24}$$

The k-ϵ model is semi-empirical and as such, incorporates five empirical constants represented by the quantities C_μ, C_1, C_2, σ_k and σ_ϵ [51] [43]. Unfortunately, the empirical constants are non-universal and therefore require modification for different flow conditions [43]. Another drawback of the k-ϵ model is the lack of source terms in equations B.22 and B.23 for purposes of modelling physical effects such as swirl, bouyancy and compressibility [51].

The computational procedure of the k-ϵ turbulence model is effected by initially solving for k and ϵ from equations B.22 and B.23. The eddy viscosity μ_t is subsequently determined from equation B.19. Using the computed values of k and μ_t, the Reynolds stresses are then determined using the Boussinesq hypothesis relation given by equation B.18. The Reynolds stresses are then computed and substituted into equation B.13 and following the solution of the RANS equation, which yields the velocity components of the fluid, G_k is updated and the solution process iteratively pursued [51], to the point of *convergence*. The form of the k-ϵ model which incorporates equations B.22 and B.23 is commonly referred to as the *Standard k-ϵ model* and has two variants termed the *renormalisation group* (RNG) and *realizable k-ϵ models* [51] [58].

iii) The Reynolds stress model The *Reynolds stress model* (RSM) precludes the Boussinesq hypothesis incorporated in the k-ϵ model and instead computes the Reynolds stresses directly [51], either through an *algebraic stress model* or a differential equation for the rate of change of stress [43]. In contrast to the k-ϵ model, the RSM accounts for the anisotropic character of the Reynolds stress field through the exact Reynolds stress transport equation i.e. equation B.16 [18]. The RSM also introduces six additional transport equations, one for each independent Reynolds stress, which may be solved along with the simplified model equation for ϵ given by equation B.23 [18]. As such, the RSM is relatively more computationally expensive.

iv) The algebraic stress model The *algebraic stress model* (ASM) is an economical means of computing the Reynolds stresses using the characteristically similar algebraic relation given by equation B.25 as opposed to the exact differential Reynolds stress transport expression given by equation B.16 [18] [43]. The computational advantage gained by the ASM over the RSM is immediately realised by comparing equations B.16 and B.25.

$$\overline{u_i' u_j'} = \frac{2}{3} k \partial_{ij} + \frac{(1 - C_\gamma)(k/\epsilon)\left(P_{ij} - \frac{1}{3} P_{ii} \delta_{ij}\right)}{C_1 + (1/2\epsilon) P_{ii} - 1} \tag{B.25}$$

where

$$P_{ij} = -\overline{u_j' u_k'} \frac{\partial \overline{u}_i}{\partial x_k} - \overline{u_i' u_k'} \frac{\partial \overline{u}_j}{\partial x_k}$$

v) The large eddy simulation model The *large eddy simulation* (LES) model is a *transient* solution procedure that solves the RANS equations for the mean flow and the largest eddies and models the effects of the smaller eddies [18]. A filtering process, which isolates the medium and large scale eddies from those smaller than a typical cell size is effected. As such, the effects of the smaller eddies are included in the filtered continuity and momentum equations, prior to their transient solution via

Turbulence model	Overview, pros and cons
Standard k-ϵ	- simple, well established and most widely validated - robust, economical and performs excellently with numerous high Reynolds number flows - not recommended for highly swirling flows
RSM	- the most accurate classical turbulence model in determining mean flow properties and Reynolds stresses - computationally more expensive than k-ϵ model - less widely validated and identically poor in performance as the k-ϵ model for some flows, due to ϵ-equation modelling
LES	- generally provides excellent results for all flow systems - requires extremely fine grid to capture turbulence in sub-grid scale eddies - requires most computational resources due to transient formulation

Table B.2: Relative performance assessment of turbulence models

a sub-grid-scale model [51]. The random fluctuations that develop on the medium and large scales are also captured during the transient solution process [51].

vi) Turbulence model comparisons A general overview and the relative performance related merits of the k-ϵ, RSM and LES turbulence models, derived on the basis of computational expense, robustness and universality in application are presented in table B.2 [18] [51].

d) Near-wall treatment of turbulent flows

Experiments indicate that the near-wall region can be subdivided into three regions that comprise an innermost, an intermediate and an outermost layer. These fluid layers are termed the *viscous sub-layer*, the *buffer layer* and the *fully turbulent layer*, respectively. The viscous sub-layer is dominated by molecular viscosity, which reduces tangential velocity fluctuations via viscous damping. The mean velocity field is also affected by the *no-slip* condition which has to be satisfied at the wall. These phenomena greatly reduce fluid momentum, which in turn effects laminar flow behaviour within this layer. In addition, a velocity gradient is established between the viscous sub-layer and the fully turbulent layer, resulting in increased turbulence intensity in the latter. In the interim region, viscous and turbulence effects are equally important.

In view of the fact that the large gradients exhibited by solution variables in the near-wall region are augmented by the vigorous transport of momentum and other scalar quantities, careful consideration needs to be given in the numerical resolution of wall-bounded flows. Unfortunately, the k-ϵ, the RSM and the LES models are primarily valid beyond the near-wall region. The *wall function* and *boundary layer meshing* approaches, which provide means for modelling the near-wall region, are discussed in the subsequent section. The discussion on the treatment of wall-bounded turbulent flows stems mainly from the Fluent [8] user's manual.

i) Wall functions and boundary layer meshing The empirically determined *law of the wall*, which forms the basis for wall functions, indicates a logarithmic variation in the streamwise velocity of near-wall flows, with distance from the wall [58]. Wall functions are semi-empirical formulae which obviate the need to modify the turbulence models to account for the presence of walls. They serve to bridge the viscous sub-layer and the buffer layer by linking corresponding solution variables at the wall to those at the near-wall cells so that the turbulence model only resolves the fully turbulent layer. An alternative approach involves boundary layer meshing through which the turbulence models are modified to enable complete resolution of the viscosity-affected regions via the construction of a very fine mesh near the wall.

The wall function approach is preferentially adopted due to its economy, robustness and reasonable accuracy in the solution of flow variables in the near-wall region. However, despite its practicality, this approach remains inadequate in the resolution of highly viscous and low velocity flows. In addition, it is also found to inappropriately resolve highly constricted and boundary layer separating flows that exhibit severe pressure gradients. The wall functions in Fluent [8] have a *standard* and *non-equilibrium* implementation and the latter is better suited to modelling severe pressure gradients, accounting for non-equilibrium effects and predicting wall shear. The grid considerations necessary for the successful implementation of wall functions are discussed in the subsequent section.

ii) Grid considerations for wall-bounded turbulent flow simulations The implementation of a mesh appropriately constructed for the numeric resolution of a wall-bounded turbulent flow is an iterative process that involves the evaluation of a dimensionless wall unit y^+, given by equation B.26 [18]. A near-wall flow is considered laminar if $y^+ \leq 11.63$ and turbulent for $y^+ > 11.63$ [18]. The wall function approach is only applicable with the latter condition [18]. Consequently, the iterative near-wall grid refinement process is undertaken until an appropriate nodal-wall distance y_P, of a near-wall node P, is determined.

$$y^+ = \frac{y_P}{\nu}\sqrt{\frac{\tau_w}{\rho}} \tag{B.26}$$

where

y^+ – dimensionless wall unit
y_P – distance of near-wall node P from the wall
ν – fluid kinematic viscosity
τ_w – wall shear stress
ρ – fluid density

However, the Fluent [8] implementation of the law of the wall is based on the wall unit y^*, defined by equation B.27c, for standard wall functions. The dimensionless groups U^* and y^*, which represent the mean fluid velocity and the wall unit, respectively, are related via the logarithmic law given by equation B.27a.

$$U^* = \frac{1}{\kappa}\ln\left(Ey^*\right) \tag{B.27a}$$

where

$$U^* = \frac{U_P C_\mu^{1/4} k_P^{1/2}}{\tau_w/\rho} \tag{B.27b}$$

$$y^* = \frac{\rho C_\mu^{1/4} k_P^{1/2} y_P}{\mu} \tag{B.27c}$$

U^* – dimensionless mean fluid velocity
y^* – dimensionless wall unit
κ – von Kármán constant (0.42)
E – empirical constant (9.793)
U_P – mean fluid velocity at point P
k_P – turbulence kinetic energy at point P
y_P – distance of near-wall node P from the wall
μ – dynamic viscosity of fluid

The logarithmic mean velocity law, which is valid for y^* values in the range 30 to 60, is employed in Fluent [8] when $y^* > 11.225$. For a mesh constructed such that $y^* < 11.225$, at cells adjacent to the wall, the laminar stress-strain relationship given by equation B.28 is employed [8].

$$U^* = y^* \tag{B.28}$$

B.1.2 Auxiliary models

In order to computationally resolve multiphase flows, the turbulence models are supplemented by auxiliary models that employ either the Euler-LaGrange or Euler-Euler solution approaches. The discussion on auxiliary models, presented as documented in the Fluent [8] user's manual, is limited to the Algebraic Slip Mixture Model (ASMM).

a) Multiphase modelling approaches

The numerical solution of a multiphase system is inherently difficult and in addition to the computational expense, stability or convergence problems may be encountered [8]. For time-dependent problems, it is recommended [8] that a time step at least an order of magnitude smaller than the characteristic time of the flow be used. However, the diversity in behaviour, of multiphase flows, means that no universal approach can be adopted for their numeric modelling. The subsequent discussion focuses on the two approaches that have been successfully implemented in this regard.

i) The Euler-LaGrange approach In the Euler-LaGrange approach, the fluid phase is treated as a continuum by solving the time-averaged Navier-Stokes equation. A solution for the dispersed phase is obtained by tracking a large number of particles, bubbles or droplets through the calculated flow field. Trajectories of distinct particles of the dispersed phase are computed individually, at specified intervals, in unison with the fluid phase calculation. Momentum, mass and energy exchanges are permissible between the dispersed and primary fluid phases. The fundamental and restrictive assumption underlying the Fluent [8] implementation of the Euler-LaGrange approach imposes use of a volume fraction nor greater than 10% for the dispersed phase. This limitation is detrimental to the numerical solution of hydrocyclone flow fields, by virtue of the fact that hydrocyclones commonly operate at much higher slurry feed concentrations [7].

ii) The Euler-Euler approach In the Euler-Euler approach, the constituent phases are treated as interpenetrating continua. The different phases are also assumed to constitute volume fractions that are continuous functions of space and time, summing up to unity, within any distinct control volume. Similarly structured conservation equations are derived for each phase and equation closure is achieved through the application of constitutive empirical relations or the kinetic theory.

b) The Algebraic Slip Mixture Model

The ASMM employs the Euler-Euler approach and solves continuity and momentum equations for the mixture and a volume fraction-derived continuity equation for each secondary phase. This model permits differential velocity flow of constituent phases, in which case, algebraic expressions for the relative velocities of any secondary phases are also solved. If all phases are assumed to move at the same velocity, the ASMM is reduced to a homogeneous multiphase model.

i) The mixture continuity equation The continuity equation for the mixture is given by equation B.29a, where $\mathbf{u}_m$, the velocity of the mixture is defined by equation B.29b and the density of the mixture ρ_m by equation B.29c. The $\dot{m}$ term on the right hand side of equation B.29a represents mass transfer due to *cavitation* or user-defined mass sources.

$$\frac{\partial}{\partial t}(\rho_m) + \nabla \cdot (\rho_m \mathbf{u}_m) = \dot{m} \tag{B.29a}$$

where

$$\mathbf{u}_m = \frac{\sum_{k=1}^{n} \alpha_k \rho_k \mathbf{u}_k}{\rho_m} \tag{B.29b}$$

$$\rho_m = \sum_{k=1}^{n} \alpha_k \rho_k \tag{B.29c}$$

$\mathbf{u}_m$ – velocity of mixture
$\mathbf{u}_k$ – velocity of phase k
ρ_m – density of mixture
ρ_k – density of phase k
$\dot{m}$ – mass transfer due to *cavitation* or user-defined mass sources
α_k – volume fraction of phase k
n – total number of constituent phases

ii) The mixture momentum equation The momentum equation of the mixture is derived via a summation of the momentum equations of all constituent phases and is given by equation B.30a. The viscosity of the mixture μ_m and the drift velocity $\mathbf{u}_{dr,k}$ of a secondary phase k are given by equations B.30b and B.30c, respectively.

$$\frac{\partial}{\partial t}\left(\rho_m \mathbf{u}_m\right) + \nabla \cdot \left(\rho_m \mathbf{u}_m \mathbf{u}_m\right) = -\nabla p + \left[\mu_m \left(\nabla \mathbf{u}_m + \nabla \mathbf{u}_m^T\right)\right] + \rho_m \mathbf{g} + \mathbf{F} + \nabla \cdot \left(\sum_{k=1}^{n} \alpha_k \rho_k \mathbf{u}_{dr,k} \mathbf{u}_{dr,k}\right) \tag{B.30a}$$

where

$$\mu_m = \sum_{k=1}^{n} \alpha_k \mu_k \tag{B.30b}$$

$$\mathbf{u}_{dr,k} = \mathbf{u}_k - \mathbf{u}_m \tag{B.30c}$$

μ_m – viscosity of mixture
$\mathbf{g}$ – gravitational acceleration vector
$\mathbf{F}$ – body force
$\mathbf{u}_{dr,k}$ – drift velocity of secondary phase k
T – transpose operator

iii) Slip and drift velocity Slip velocity is defined as the velocity of a secondary phase p relative to the velocity of a primary phase q and is given by equation B.31a. The drift velocity of an arbitrary secondary phase k is defined as the relative velocity between the secondary phase and the mixture and is given by equation B.30c.

$$\mathbf{u}_{pq} = \mathbf{u}_p - \mathbf{u}_q \tag{B.31a}$$

The relationship between the drift velocity $\mathbf{u}_{dr,p}$ of a secondary phase p and its slip velocity $\mathbf{u}_{pq}$, is given by equation B.31b.

$$\mathbf{u}_{dr,p} = \mathbf{u}_{pq} - \sum_{k=1}^{n} \frac{\alpha_k \rho_k}{\rho_m} \mathbf{u}_{qk} \tag{B.31b}$$

The ASMM computes the particle slip velocity $\mathbf{u}_{pq}$ via the the Manninen et. al. algebraic slip formulation given by equation B.31c. This relation incorporates the assumption that local equilibrium is attained between the constituent phases over short spatial length scales. The drag force f_d on a secondary phase particle of diameter d_p is governed by equation B.31d and the corresponding particle acceleration is determined via equation B.31e. Other forms of the drag law and particle acceleration formulations, which include the option of specifying user-defined functions, are also available.

$$\mathbf{u}_{pq} = \frac{(\rho_p - \rho_m)\, d_p^2}{18 \mu_q f_d}\mathbf{a} \tag{B.31c}$$

where

$$f_d = \left\{ \begin{array}{lll} 1 + 0.15 Re^{0.687} & ; \quad Re & \leq \quad 1000 \\ & & \\ 0.0183 Re & ; \quad Re & > \quad 1000 \end{array} \right\} \tag{B.31d}$$

$$\mathbf{a} = \mathbf{g} - (\mathbf{u}_m \cdot \nabla)\, \mathbf{u}_m - \frac{\partial \mathbf{u}_m}{\partial t} \tag{B.31e}$$

d_p – particle diameter of secondary phase p
$\mathbf{a}$ – particle acceleration of secondary phase p
ρ_p – density of secondary phase p
ρ_m – density of primary phase q
μ_q – viscosity of primary phase q
f_d – drag function

iv) Transport equation for secondary phases The ASMM accounts for the transport of the volume fraction of each dispersed phase p via equation B.32. This volume fraction equation is derived from the continuity equation of each distinct secondary phase.

$$\frac{\partial}{\partial t}(\alpha_p \rho_p) + \nabla \cdot (\alpha_p \rho_p \mathbf{u}_m) + \nabla \cdot (\alpha_p \rho_p \mathbf{u}_{km}) = 0 \tag{B.32}$$

B.2 The methodology of solution of CFD codes

Current commercial CFD codes facilitate interaction with the user through graphical user interfaces equipped to tackle the problem definition and numerical solution of a broad range of fluid dynamics problems [18]. The main phases of the computational simulation process required to obtain a numerical solution to a fluid flow problem involve *pre-processing* and *post-processing*.

a) Pre-processing

Pre-processing is here defined with respect to Gambit version 2.1.6. This phase, concerned with the definition of the fluid flow problem, involves the input of user-defined data that includes:

- specification of the solver to be used in the post-processing phase

- computational domain specification through geometry definition
- surface mesh generation and volume meshing
- edge/surface specific boundary type specification
- surface/volume specific continuum type specification
- surface/volume mesh exportation

c) Post-processing

The *post-processing* phase, discussed with reference to Fluent [8] version 6.1.22, may be subdivided into two stages. These include the iterative solution process via the solver specified in the pre-procesing phase and data extraction and manipulation through the post-processing facilities. Prior to either subsidiary stage, the surface/volume mesh for the two/three-dimensional problem is imported from Gambit into Fluent, which has the option of single or double precision numerical representation.

i) The solver Present-day numerical solution techniques fall into three distinct streams namely; *finite difference*, *finite element* and *spectral methods*. These streams are distinguished from each other via the methodology implemented in approximating the flow variables as well as through the associated *discretisation* processes. In general terms, the steps performed by the numerical techniques on which the solver is based include [18]:

1. Employing simple functions in the approximation of unknown flow variables.
2. Discretisation of governing flow equations through the substitution of the derived approximations.
3. Casting of resulting equations, through mathematical manipulation, into a form suited to numerical solution.
4. Solution of the resulting set of algrebraic equations.

The finite volume method, which evolved as a special finite difference formulation, forms the basis of the code to some of the Fluent solvers. The numerical algorithm of this well established and thoroughly validated CFD technique, involves the following steps [18]:

1. *Integration* of the equations governing fluid flow over all the finite control volumes contained within the computational domain.

2. *Discretisation*, which involves the conversion of the integral equations into a system of algebraic equations. This is effected through the generation of finite difference approximations of the integral equation terms representing flow processes such as convection, diffusion and sources.
3. *Iterative solution* of the algebraic equations.

To effect numerical solution of a fluid flow problem, with reference to a user-specified Fluent solver, the following more specific generic steps are necessary:

- specification of fluid properties and the relevant fluid models
- boundary condition specification
- setting the initial condition(s)
- specification of the solver and formulation options i.e. segregated/coupled and implicit/explicit respectively
- specification of the time dependance of the solution i.e. steady/unsteady
- specification of solver controls e.g. convergence criteria, solution time step and duration etc.
- initialising the solution

The numerical solution process is iterative and as such, certain criteria defining solution *convergence* need to be specified. Convergence of a solution in a numerical sense refers to the condition under which the numerical solution may be deemed an acceptable approximation to the exact solution [18]. It is common practice to specify flow-variable-specific *residuals*, as convergence criteria.

ii) The post-processor Although Fluent is in its entirety a post-processor, the post-processor here defined refers collectively to the data extraction and analysis tools available for processing post solution data. The two/three dimensional data visualisation and manipulating tools incorporated in the post-processor facilitate:

- geometry mesh visualisation
- flow variable contour, vector and histogram plotting
- visualisation of particle path lines
- determination and visualisation of particle tracks

- numeric and graphic data exports
- view perspective manipulation and scene animation
- extraction of a summary of information related to the specified; models, boundary conditions, solver controls and fluid/solid material properties
- quantitative determination of fluxes across boundaries and forces acting against wall boundaries

Appendix C

Comparative CFD Hydrocyclone Velocity Profile Predictions

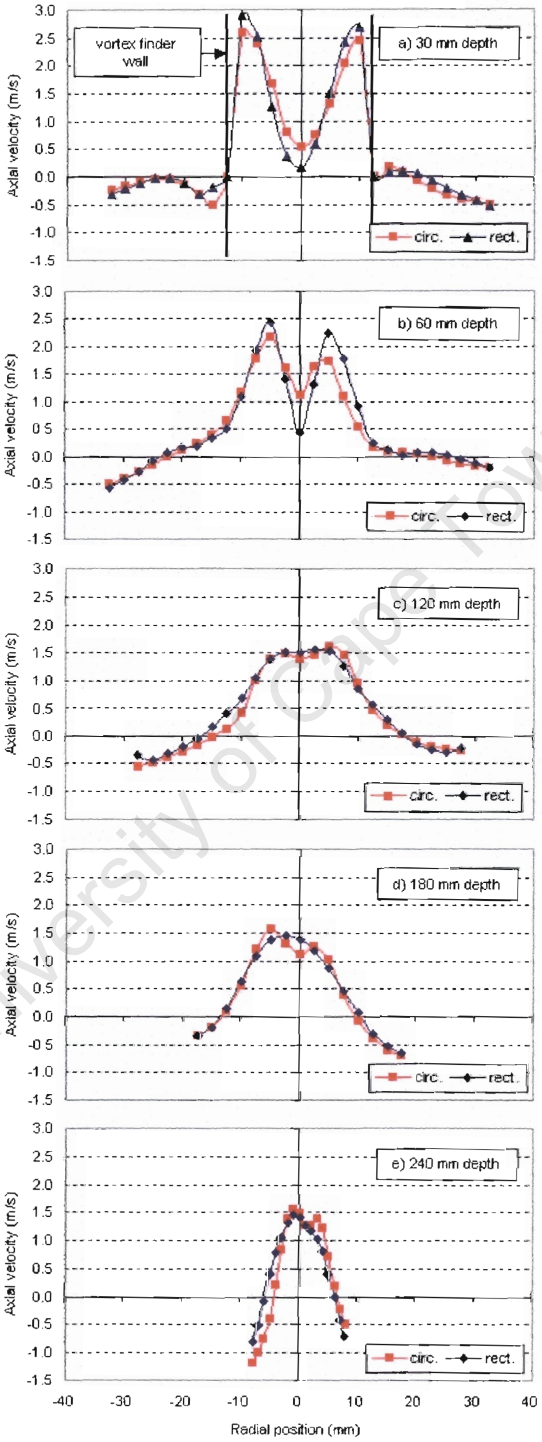

Figure C.1: Circular and rectangular inlet hydrocyclone axial velocity profile comparison

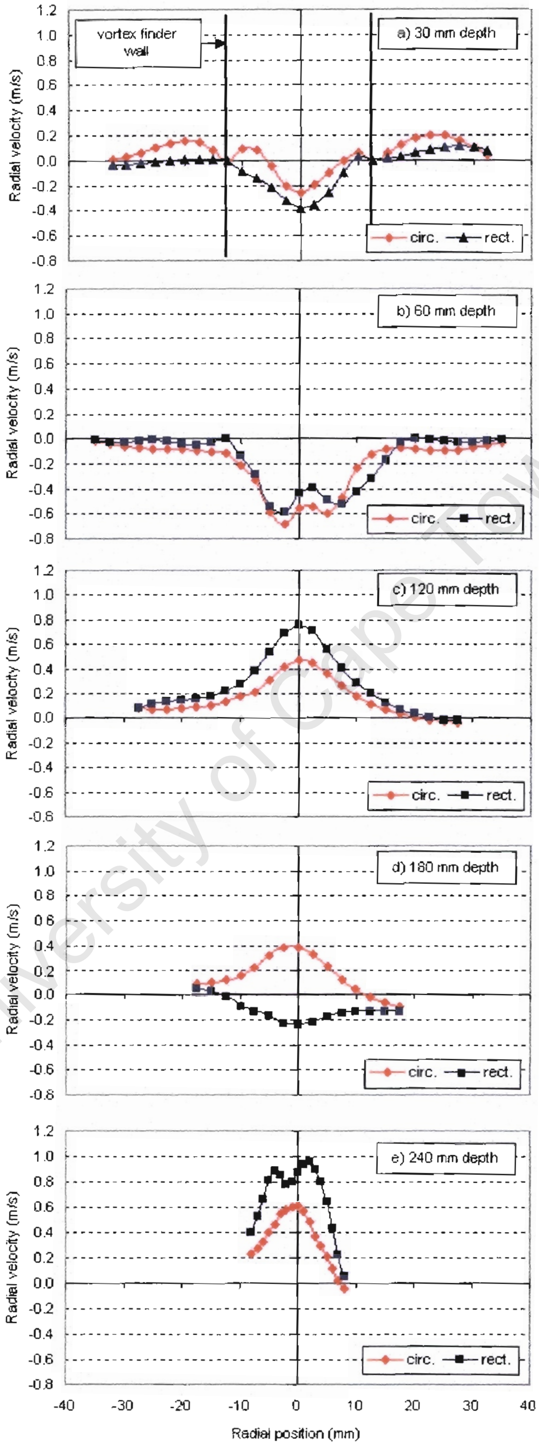

Figure C.2: Circular and rectangular inlet hydrocyclone radial velocity profile comparison

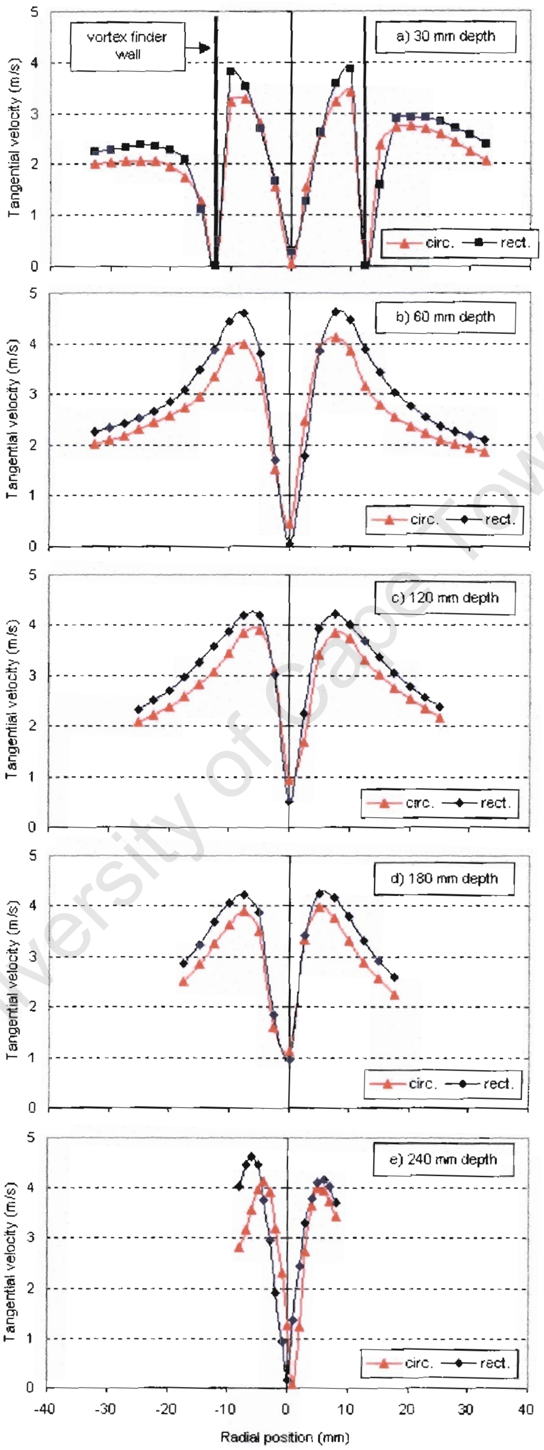

Figure C.3: Circular and rectangular inlet hydrocyclone tangential velocity profile comparison